Modelling and simulation of engineered cardiac tissue for drug safety testing



Maxandre Jacqueline
Pembroke College
University of Oxford

A thesis submitted for the degree of
Master of Science by Research

Michaelmas 2019

Acknowledgements

I thank my supervisors for their guidance throughout this work. In particular, Sarah Waters, for her support in important times, Ruth Baker, for her sharp eye on my work, Liudmila Polonchuk, for her professionalism, and Ken Wang, for her helpful suggestions. In addition, many thanks to Sarah and Ruth for teaching me mathematical and scientific writing.

I am grateful for the funding provided by the Engineering and Physical Sciences Research Council (EPSRC), the Medical Research Council (MRC), and Roche. I give special thanks to Bryn Roberts for his crucial help in setting up this project. I thank Garrett Morris and Gesine Reinert for accepting me into the Systems Approaches to Biomedical Science (SABS) programme at the Doctoral Training Centre (DTC). I enjoyed attending the SABS taught courses during my first year. I thank my college advisor Raphael Hauser for his responsiveness and professional insight, and Philip Maini for being a responsible chair for the mathematical biology group. I give my warm thanks to Sandy Patel and Alison Franklin for their caring support.

I thank Louise Bowler for her assistance and for providing C++ simulation code that was utilised in this work. I am grateful to Michelangelo Paci for discussing this work with me. I thank Leo Doerr for his help with the CardioExcyte Control software. I thank Sonja Stölzle-Feix and Ulrich Thomas for replying to my questions about the CardioExcyte96 recording device. Many thanks to Bartosz, Fergus and Joe Pitt-Francis for their help with Chaste.

Huge thanks to my fellow mathematical biologists Barbara, Andrew, Maxi and Citlali for their friendliness. I am grateful to Guillermo and Kristina for friendly discussions. My girlfriend Sarah knows how much the past years have been an adventure for me. Thank you for being by my side. Finally, I am grateful to my parents Lisa and Serge. *Maman*, your medical tales sparked my interest in medicine. *Papa*, your innumerable gifts ignited and enabled my interest in computers. Our travels around the world raised my awareness of the importance of mastering the English language. The actions of both of you contributed to my joining Oxford.

Abstract

Within the drug development process, the detection of the drugs that are *not* proarrhythmic is particularly important. The recent Comprehensive *in vitro* Proarrhythmia Assay (CiPA) initiative makes use of two new technological developments to improve this detection process. The first technological development is the invention of human engineered cardiac tissue (hECT) that can be used as an *in vitro* platform for testing the effects of drugs on the heart. The second technological development is the advent of sophisticated mathematical models and computational simulations of cardiac tissue. In this thesis, we highlight the potential for improvement of the theoretical model currently chosen by the CiPA initiative to predict the arrhythmogenicity of drugs. The principal aim of this thesis is to investigate the use of a multiscale model that directly predicts the effect of drugs on hECT.

We begin by presenting the cardiological notions necessary for our investigation into the effect of drugs on hECT. Next, we introduce our multiscale mathematical model of the electrophysiological response of hECT to drugs. Our methodology for simulating this model is then laid out. We present the parametrisation, verification and analysis of the simulations. Lastly, we present our results on the electrophysiological response of engineered cardiac tissue to drugs. In particular, we compare predictions of the multiscale model to *in vitro* data of the effects of drugs on hECT. We conclude by identifying specific directions for future research to improve the *in silico* prediction of drug effects on hECT.

Contents

Acronyms **1**

1 Introduction **2**
1.1 Background 4
1.2 Aims 6
1.3 Approach 7
1.4 Outline 8

2 Cardiological background **9**
2.1 Cardiac electrophysiology 9
2.1.1 Action potential 12
2.1.2 Field potential 15
2.1.3 Electrocardiogram 15
2.2 Drug cardiac safety testing 17
2.3 Human engineered cardiac tissue 18
2.4 Conclusion 20

3 Mathematical models of cardiac electrophysiology **21**
3.1 Models of cellular electrophysiology 22
3.1.1 The Hodgkin-Huxley model 22
3.1.2 The Noble (1962) model 24
3.1.3 The Paci (2013) model 25
3.2 Drug conductance block model 27
3.3 The bidomain model 27
3.4 Weighted cellular phenotypes model 29
3.5 Phenotype distribution model 30
3.6 Conclusion 31

4 Simulation and signal processing of the electrophysiological response of engineered cardiac tissue to drugs 32
4.1 Experimental set-up . . . 32
4.2 Model adaptations . . . 35
4.3 Simulation . . . 37
4.3.1 Implementation . . . 38
4.3.2 Verification . . . 38
4.4 Signal processing . . . 41
4.4.1 Field potential signal processing . . . 41
4.4.2 Action potential signal processing . . . 49
4.4.3 Implementation . . . 54
4.5 Uncertainty quantification of simulations . . . 55
4.5.1 Spatial resolution . . . 56
4.5.2 Adaptive timestep and tolerance . . . 57
4.5.3 Approximation of the steady state of the summary statistics . 58
4.6 Discussion . . . 62

5 *In silico-in vitro* investigation of the electrophysiological response of engineered cardiac tissue to drugs 63
5.1 Insight into the dynamics of the measured field potential signal . . . 64
5.2 Drug-dependent field potential duration biomarker validity . . . 72
5.2.1 Example I_{CaL} blocker: nifedipine . . . 78
5.2.2 Example I_{Kr} blocker: droperidol . . . 81
5.2.3 Example I_{CaL} and I_{Kr} balanced blocker: pimozide . . . 85
5.2.4 Example I_{Na}, I_{CaL} and I_{Kr} multiblocker: quinidine . . . 87
5.2.5 Conclusion . . . 89
5.3 Influence of ρ_{v} on action potential duration . . . 90
5.4 *In silico* and *in vitro* effects of drugs on time-to-repolarisation biomarkers 92
5.4.1 I_{CaL} blockers . . . 97
5.4.2 I_{Kr} blockers . . . 102
5.4.3 I_{CaL} and I_{Kr} balanced blockers . . . 106
5.4.4 I_{Na} and I_{Kr} multiblockers . . . 109
5.4.5 I_{Na}, I_{CaL} and I_{Kr} multiblockers . . . 112
5.5 Discussion . . . 116

6 Conclusion and future work **119**
6.1 Summary and conclusions 119
6.2 Future work 121

A Supplementary information for Chapter 4 **125**
A.1 Detailed description of the experiments 125
A.1.1 Sensor plate preparation and cell seeding 125
A.1.2 Chemical reagents and solutions 126
A.1.3 Data acquisition and analysis 126
A.2 Methods for the calculation of APD_{90} 127
A.2.1 Calculation of the depolarisation time in the hiPSC-CM method 127
A.2.2 Calculation of the repolarisation time in the hiPSC-CM method 128
A.2.3 Calculation of the action potential duration at 90% repolarisation in Chaste 128
A.3 Uncertainty quantification: resolution 130
A.4 Uncertainty quantification: steady state of the summary statistics . . 131
A.4.1 Outlier removal in time series 131
A.4.2 Relaxation to steady-state of drug simulations 131

B Supplementary information for Chapter 5 **134**
B.1 Effect of drugs on time to repolarisation biomarkers 134
B.1.1 I_{CaL} blockers 136
B.1.2 I_{Kr} blockers 137
B.1.3 I_{CaL} and I_{Kr} balanced blockers 138
B.1.4 I_{Na} and I_{Kr} multiblockers 139
B.1.5 I_{Na}, I_{CaL} and I_{Kr} multiblockers 140

References **145**

Acronyms

AL atrial-like

CiPA Comprehensive *in vitro* Proarrhythmia Assay

CM cardiomyocyte

EAD early after depolarisation

ECG electrocardiogram

FPD field potential duration

FPS field potential signal

hECT human engineered cardiac tissue

hERG human *ether-à-go-go* related gene

hiPSC human induced pluripotent stem cell

hiPSC-CM human induced pluripotent stem cell derived cardiomyocyte

ICH International Council on Harmonization of Technical Requirements for Registration of Pharmaceuticals for Human Use

MEA micro electrode array

RMSE root mean squared error

TdP torsade de pointes

VL ventricular-like

Chapter 1

Introduction

In the 1990s and 2000s, cardiotoxicity caused one third of all drug safety concerns [1]. These concerns appeared in the form of drug withdrawals from the market, safety warnings for marketed drugs, and the termination of (pre)clinical drug development projects [1]. In particular, nine drugs were removed from the market or had their availability severely restricted because they induced torsade de pointes (TdP), a potentially fatal ventricular arrhythmia [2]. Subsequently, a strategy based on two surrogate biomarkers for arrhythmia was established to prevent future pro-arrythmic drugs from reaching the market. These two biomarkers are: (i) the blockage of the potassium channel encoded by the human *ether-à-go-go* related gene (hERG), later referred to as *hERG block*; and (ii) the prolongation of *in vivo* cardiac repolarisation [3]. This strategy was successful in that no new marketed drugs have been associated with an unacceptable risk of TdP [3]. However, as many as 60% of drug compounds have also been excluded from further development as a result of this strategy [4]. As a proportion of those drugs are in fact not pro-arrythmic, a more specific detection of pro-arrhythmic compounds is urgently required.

The CiPA initiative [5] aims at improving specificity of the preclinical detection of pro-arrhythmic compounds. This initiative consists of four components [3]. First,

drug effects on human ion channels are assessed *in vitro* (step 1). The human ion channels studied in the CiPA initiative are expressed in heterologous cells by genetic recombination [6, 7]. These heterologous cells include human embryonic kidney cells, chinese hamster ovary cells and chinese hamster lung cells. The second component of CiPA is the integration of the ion channel effects at the level of a cell. In this component, the prediction of the arrhythmogenicity of a drug is obtained via an *in silico* simulation of the effect of the drug on an adult human ventricular cardiomyocyte (step 2). The third component of CiPA is the *in vitro* assessment of drug arrhythmogenicity in human induced pluripotent stem cell (hiPSC) derived cardiomyocytes (CMs) (hiPSC-CMs) (step 3). The *in silico* prediction of drug arrhythmogenicity from step 2 is compared with the *in vitro* assessment from step 3. The last component of CiPA is the clinical assessment of drug arrhythmogenicity from human electrocardiogram (ECG) data collected in a phase I clinical trial (step 4). The success of CiPA would enable safe compounds blocking the hERG channel and/or prolonging cardiac repolarisation to have better chances of reaching patients with unmet medical needs [3].

To ensure the success of the CiPA objectives, current limitations in the present CiPA plan must be addressed. We address two such limitations in this thesis. The first limitation of the current CiPA initiative lies in the discrepancy in the cell types used for the *in silico* and *in vitro* investigation of arrhythmogenicity (step 2 and 3). While the *in silico* investigation (step 2) utilises a mathematical model of an *adult* ventricular cell, the *in vitro* investigation (step 3) uses hiPSC-CMs with both adult ventricular-like (VL) and atrial-like (AL) characteristics, making the intended *in silico-in vitro* comparison more difficult. The second limitation is the difference in the spatial scales of the *in silico* and *in vitro* investigations. While the *in vitro* investigation studies hiPSC-CM monolayers comprising AL and VL cells, the *in silico* assessment involves a single ventricular CM only. To our knowledge this is the first

mention of these two precise limitations in the literature, although the choice of the *in silico* approach used in the CiPA initiative was first put into question by Lee *et al.* (2017) [8].

In this thesis, we conduct an *in silico* electrophysiological study of the drug responses of a hiPSC-CM monolayer. Complementary to step 2 of the CiPA initiative, which considers a mathematical model of the electrophysiology of a single adult ventricular CM, the mathematical model of the electrophysiology of an hiPSC-CM monolayer that we develop will allow direct comparison between *in silico* predictions and results obtained with the *in vitro* experiments on a hiPSC-CM monolayer in step 3. We study the arrythmogenicity of drugs via the electrophysiological response of hECT to drugs. We study the effect of 12 drugs selected for development and validation of the CiPA assays [3] and compare our *in silico* results with electrophysiological experimental data collected by the pharmaceutical company Roche (F. Hoffmann-La Roche AG, Switzerland).

1.1 Background

We develop a suite of *in silico* models for hECT. We consider hECT derived from hiPSCs [9]. This *in vitro* platform has given encouraging results in the preclinical cardiotoxicity assessment of drugs [10]. Compared to human embryonic stem cells, hiPSCs have the benefit of being more commercially available, causing less ethical controversy, and having the potential to more faithfully reproduce the tissue of any given individual patient. In biological research, hECT is an *in vitro* model of human *in vivo* cardiac tissue that is used to study the physiological and pathological states of cardiac tissue. In pharmacology, hECTs are utilised to study cardiac responses to the administration of drugs [11]. The inclusion of hECT in microphysiological *in vitro* systems (e.g. organ-on-a-chip) for drug testing [11] is currently attracting large

financial investment [12], with the ultimate aim of replacing *in vivo* animal testing and of building test systems for personalised medicine. In regenerative medicine, hECT can provide contractile support to a failing heart [13] in the form of a surgically sutured patch [14].

The methodology underlying this work consists of mathematical modelling and computational simulation of the electrophysiology of hiPSC-derived hECTs. An essential component of a mathematical model of hECT is a model of its constituent cardiac cells. The earliest simulation based on a mathematical model of a cardiac Purkinje cell dates back to Noble (1962) [15]. The development of mathematical models of hiPSC-CMs has only borne fruit in the last decade with the work of Paci [16–19]. In particular, Paci *et al.* (2013) [16] have developed mathematical models for both AL and VL hiPSC-CM phenotypes. In this thesis we only consider these two cell phenotypes and neglect nodal-like cells which were found to be the least common type of hiPSC-CM [20]. Bowler *et al.* [21] integrated hiPSC-CMs in a mathematical model of hECT through a homogenisation approach that captures the presence of the AL and VL hiPSC-CM phenotypes in a hECT. Alternatively, Abbate *et al.* (2018) have utilised distinct spatial domains for the different CM phenotypes [22]. This last approach is computationally tractable only when a small number of phenotypically homogeneous regions is considered. However, experiments indicate that AL and VL phenotypes are well-mixed within hECT [23, 24]. In the well-mixed case the approach of Abbate *et al.* becomes computationally intractable, as the domain needs to be subdivided into many phenotypically homogeneous subdomains. In this work we choose to follow the approach by Bowler *et al.* [21] which allows for smoothly varying proportions of cell phenotypes with a tractable computational cost. The work presented in the doctoral thesis of Bowler [25] is taken as a starting point for this thesis. We adapt the model to capture measurements performed on a different recording device (CardioExcyte96, Nanion Technologies, Germany), and use it to examine a larger set

of drugs.

Several challenges need to be overcome for computational simulations of hECTs to reproduce experimental results. First, the model should be parametrised with data obtained at the same experimental temperature as the experiments we model. Second, the extracellular concentrations of ions parametrising the simulations should match experimental conditions. Third, Lei *et al.* identified the benefits of calibrating the mathematical model to the cell line used in the experiments [26]. Finally, the simulation of the electrophysiological activity of the tissue is computationally demanding. In this study, we have tackled the first of those challenges by choosing a cardiomyocyte model [16] that was parametrised using experiments conducted at 37°C [20] which matches the temperature of our experiments. The extracellular concentrations parametrising the cellular model were modified to match our experimental conditions. Furthermore, the hiPSC-CMs used in our experiments come from the same manufacturer (Cellular Dynamics International, Madison, Wisconsin, USA) as the cells used to produce the data that parametrised the CM model that we use. Regarding the final, computational challenge, we have chosen to use the efficient parallel numerical solver implemented in Chaste [27]. The stiff ordinary differential equation (ODE) systems contained in cardiac cellular models are solved with the fast CVODE [28] library, as recommended by [29].

1.2 Aims

The overarching aim of this thesis is to predict *in silico* the electrophysiological behaviour of a hiPSC-CM monolayer subject to drugs. We introduce a mathematical model of the measurements performed on the CardioExcyte96 recording device. The experimental data available for this project includes control and drug-perturbed electrophysiological recordings of hECTs that we take as a reference for our models.

1.3 Approach

We follow an *in silico* methodology that includes the development of a mechanistic mathematical model and computational simulation of the drug responses of hECT. A mathematical model encodes observations of a system in a mathematical language and the computational simulation decodes the mathematical model into predictions for the system that can be compared with observations. The *in silico* methodology used here can complement experimental results by providing mechanistic understanding. In addition, predictions of the mathematical model can help reduce the total number of experiments that need to be conducted by selecting those that are predicted to be most informative. As experiments are much more expensive than computation, this can significantly reduce time and expense. In the case of drug testing, drugs predicted by the computational model to be arrhythmogenic can be given special attention in the *in vitro* safety study.

Two prerequisites need to be met before the mathematical model and computational simulation can be used to predict drug effects. The two prerequisites are the *verification* of the simulation framework and the *validation* of the model. Firstly, the computational simulation framework needs to be *verified* to ensure that it is correctly computing quantities specified by the model. We will verify the simulation framework by conducting a convergence analysis. Secondly, the mathematical model needs to be *validated* to ensure that it behaves sufficiently similarly to the system for predicting the drug response of hECT. We will validate the model of hECT by comparing the output of the simulation with experimental data of hECT collected in the presence and in the absence of drugs.

We will develop and simulate an electrophysiological model for hECT. We model the cardiac electrophysiological mechanisms with differential and algebraic equations to benefit from the detailed knowledge of cardiac beating mechanisms while keeping the computation tractable (as opposed to molecular simulations of ion channel dy-

namics, for example). Given the complexity of the system modelled, we aim for at least a *qualitative* validation of the model. By *qualitative* we mean that the output of the simulation of the model should reproduce experimental trends and fall within the range of the experimental measurements. If the simulation is able to achieve those goals for drug-free as well as drug-perturbed experimental data, we will deem that the model is qualitatively validated.

1.4 Outline

In Chapter 2, we introduce the cardiological knowledge necessary to conduct our study into the effects of drugs on hECT. In Chapter 3, we present the mathematical models relevant for this study. In Chapter 4, we introduce our methodology for studying the electrophysiological response of hECT to drugs. In Chapter 5, we present the results of our study. In Chapter 6, we summarise our findings and identify directions for future research.

Chapter 2

Cardiological background

In this study, we investigate the effects of drugs on the electrophysiology of hECT. This chapter provides the cardiological background knowledge necessary to conduct our investigation. In Section 2.1, we explain fundamental notions of cardiology, focusing on cardiac electrophysiology. In Section 2.2, we present the current regulatory guidelines for the cardiac safety testing of drugs. In Section 2.3, we provide background knowledge on hECT. Finally, Section 2.4 summarises the discussion contained in this chapter.

2.1 Cardiac electrophysiology

In this work, we study the side effects of drugs on the human heart. The human heart is a muscular pump that allows for the rapid transport of oxygen, nutrients, waste products and heat around the body [30]. The heart consists of four chambers: the left and right atria, and the left and right ventricles. Figure 2.1 shows the locations of the atria and ventricles in the heart and the circulation of blood through the heart. Deoxygenated blood fills the right atrium before being pumped into the

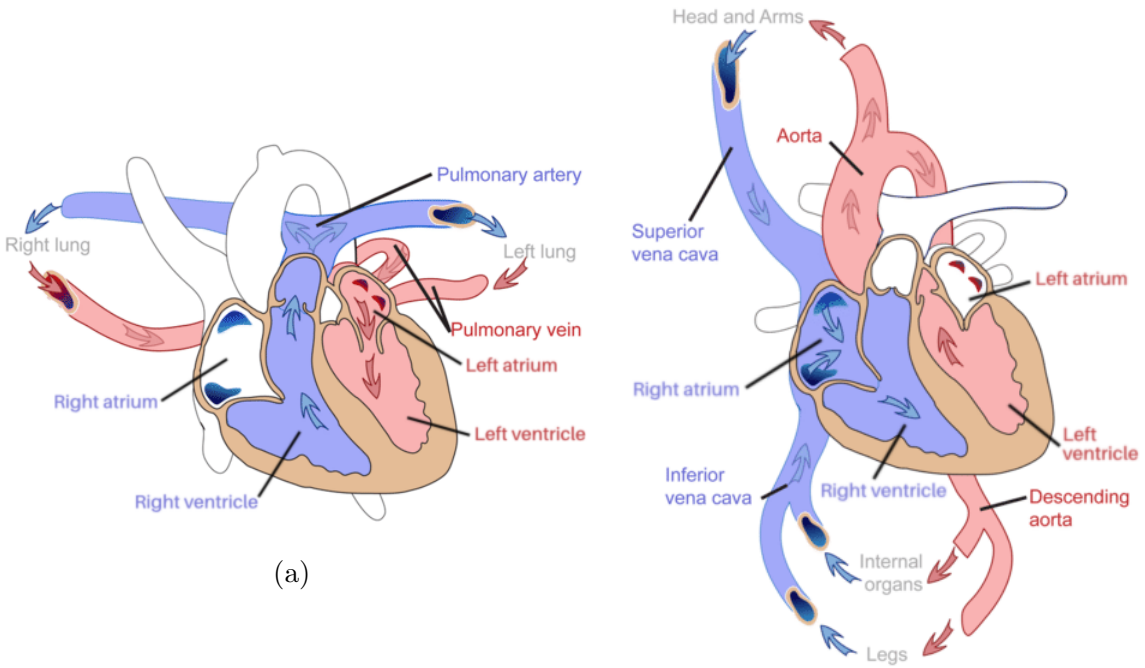


Figure 2.1: Diagrams illustrating the movement of blood through the heart. Figure (a) shows the movement of blood during pulmonary circulation and Figure (b) the movement of blood during systemic circulation. Deoxygenated blood is coloured in blue and oxygenated blood is coloured in red. Arrows indicate the direction of blood flow. The major anatomical parts of the heart are named and identified on the diagrams with lines. Figure adapted from originals created by Mariana Ruiz Villarreal (LadyofHats) for CK-12 Foundation.

right ventricle. The right ventricle then pumps the blood through the lungs to the left atrium (pulmonary circulation). This circulation oxygenates the blood. The oxygenated blood is ejected from the left atrium into the left ventricle. The left ventricle finally contracts to pump the oxygenated blood through the body back to the right atrium (systemic circulation).

Our work focuses on the effect of drugs on the electrophysiology of the heart. The contraction of the heart is activated by an electrical wave called the *activation wave*. The electrical conduction system of the heart is presented in Figure 2.2. The activation wave is initiated at the sinoatrial node and propagates to the ventricles through the atrioventricular node [32]. The activation wave is then conducted at

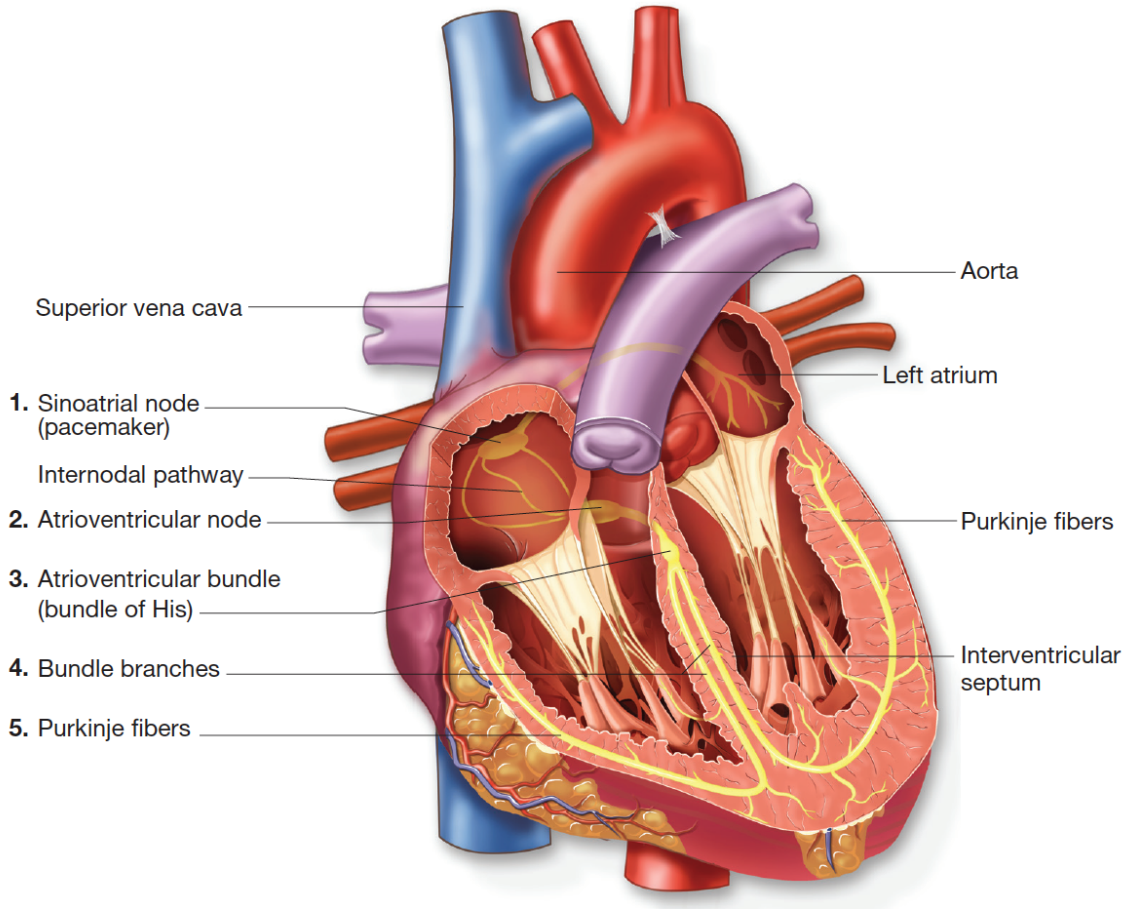


Figure 2.2: Diagram describing the electrical conduction system of the heart. The major anatomical parts of the heart are named and identified on the diagram with lines. The activation wave crosses the numbered anatomical parts in the order indicated by the numbers. Reproduced from [31] with permission of Pearson Education, Inc., New York, New York.

high speed throughout the ventricles via conducting pathways. These pathways are the atrioventricular bundle, the bundle branches, and eventually the Purkinje fibres [32]. They permit the near-synchronous contraction of the ventricles necessary to pump blood out efficiently [32].

Heart muscle cells, also known as cardiomyocytes (CMs), are the cells that perform the contraction. The activation wave propagates between adjacent CMs through low-resistance connections called gap junctions. This propagation can be observed through changes in the *membrane potential*, V_{m}. The membrane potential is defined as the difference in electric potential between the interior and the exterior of a biological

cell, such that

$$V_{\mathrm{m}} = V_{\mathrm{i}} - V_{\mathrm{e}}, \tag{2.1}$$

where V_{i} is the intracellular potential and V_{e} is the extracellular potential. Before activation, V_{m} is at a negative value called the *resting potential*. The activation wave causes V_{m} to increase (*depolarise*). When V_{m} depolarises above a threshold potential, a sudden large increase in membrane voltage occurs. Later, V_{m} progressively decreases (*repolarises*) back to the resting potential. The depolarisation and repolarisation of CMs described here is termed an *action potential*.

2.1.1 Action potential

The action potential is the result of various ionic currents across the CM membrane. The drugs that we study in this project act on the heart by blocking specific ionic currents. Ionic currents may traverse the membrane through either of two kinds of transmembrane proteins [33]. These proteins are *ion channels* and *ion pumps* [33]. Ions move through ion channels subject to diffusion and the surrounding electric field. For example, K^+ ions are more concentrated inside the cell than outside. This concentration difference drives K^+ out of the cell (chemical force). However, the cell contains large, impermeable, proteins which are negatively charged. This negative polarity attracts K^+ into the cell (electrical force). When the electrical force acting on K^+ balances the chemical force, the membrane potential is equal to the K^+ equilibrium potential, E_{K^+}.

The membrane potential of the cell is determined by the intracellular and extracellular concentrations of three ions, K^+, Na^+ and Ca^{2+}. Let us consider one of these ions, S. We assume that the membrane is only permeable to S. The equilibrium

potential for S, E_S, can be obtained from the Nernst equation [34]

$$E_S = \frac{RT}{zF} \ln \left(\frac{[S]_\mathrm{e}}{[S]_\mathrm{i}} \right), \tag{2.2}$$

where R is the gas constant, T is the temperature, z is the charge on S and F is Faraday's constant. Finally, $[S]_\mathrm{e}$ is the extracellular concentration of S, and $[S]_\mathrm{i}$ is the intracellular concentration of S.

The ionic current for S across ion channels is proportional to the difference between the membrane potential, V_m, and E_S. This ionic current, I_S, can be obtained from the equation

$$I_S = g_S \left(V_\mathrm{m} - E_S \right), \tag{2.3}$$

where g_S is the ionic conductance of ion channels for S. Ion pumps also contribute to ionic currents across the cell membrane. They transfer ions across the cell membrane by using energy. Their role is to maintain the ionic concentration differences across the cell membrame.

Ionic currents shape the morphology of the action potential. Figure 2.3 presents the typical shape of the action potential of a ventricular CM in physiological conditions. The action potential is divided into five phases. The inward sodium current across fast sodium channels, I_Na, causes the rapid depolarisation of V_m in phase 0. Phase 0 is known as the action potential *upstroke*. The following phase, phase 1, is marked by a rapid repolarisation of the membrane caused by the opening of transient outward K^+ channels letting the I_to current through. In phase 2, the inward current across long-lasting (L-type) calcium channels, I_CaL, delays the repolarisation. Phase 2 is known as the *plateau* phase of the action potential. The action potential ends with phase 3. The outward delayed-rectifier potassium current, I_Kr, increases while I_CaL decreases. This results in the repolarisation of V_m. In phase 4, V_m is at the resting potential. The different phases and principal ionic currents are illustrated in

Figure 2.3.

Changes in the action potential enable the detection of arrythmia. In particular, pro-arrhythmic drugs can be identified through changes in the action potential. The action potential duration at 90% repolarisation, APD_{90}, is a statistic[1] that can be extracted from the action potential trace. The APD_{90} statistic is defined as the duration between the depolarisation and the 90% repolarisation of V_m. Figure 2.3 illustrates this definition. The prolongation of APD_{90} is linked with arrhythmia [36].

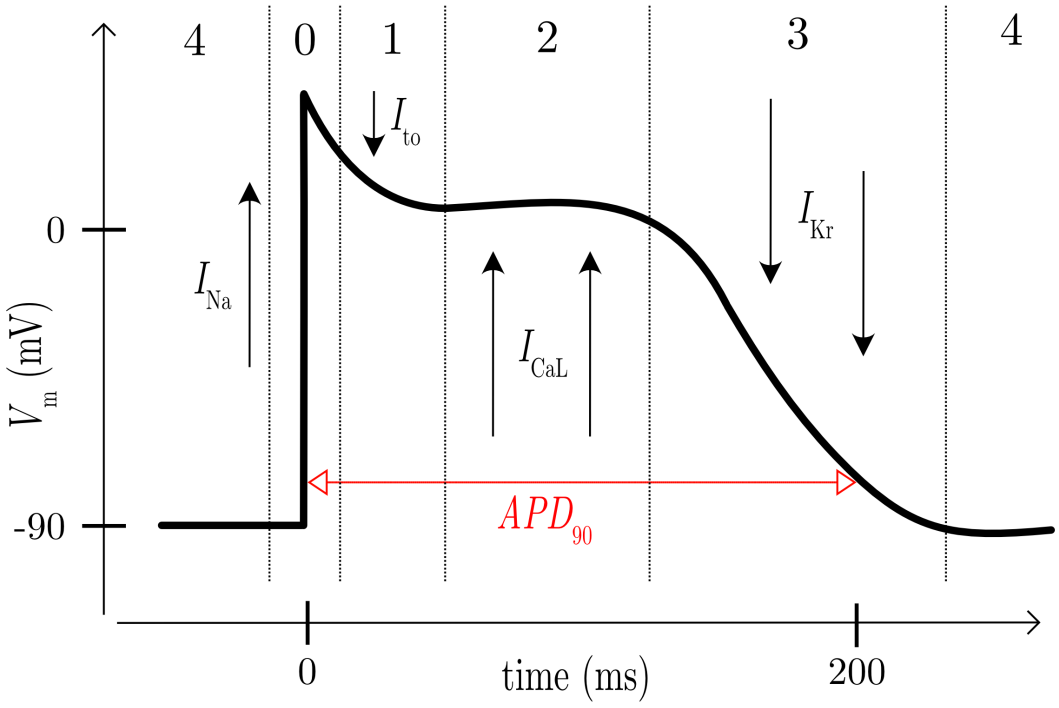


Figure 2.3: Sketch of a typical action potential of a ventricular CM in physiological conditions. The dotted lines delineate the five phases of the action potential. Each phase is numbered. The impact of ionic currents on the action potential is illustrated with arrows. The fast sodium current, I_{Na}, and the L-type calcium current, I_{CaL}, increase V_{m}; the transient outward current, I_{to}, and the delayed-rectifier potassium current, I_{Kr}, decrease V_{m}. The red arrow indicates the time span of APD_{90}. Figure adapted from [33, 37].

[1]In this thesis, we interchangeably use the terms summary statistics [35], statistics, features and biomarkers to refer to the scalar values (like APD_{90}) that summarise the signals considered.

2.1.2 Field potential

The variation in V_{m} during an action potential occurs concomitantly with a variation in the extracellular potential, V_{e}. This variation in V_{e} is called the *field potential*. The recording of an action potential requires the measurement of both V_{e} and V_{i} (see Equation (2.1)), whereas the recording of a field potential only requires the measurement of V_{e}. In addition, the measurement of V_{e} is less invasive than that of V_{i}. As a result, the field potential is easier to measure than the action potential. In this project, we focus on the influence of drugs on the field potential. The analysis of the field potential is not as well-established in the literature as the analysis of the action potential or the ECG. Our study will focus in part on deriving biomarkers from the field potential.

2.1.3 Electrocardiogram

The pro-arrhythmic effects of drugs on patients are detected on ECGs. The ECG is the surface recording of the electrical activity of the heart [33]. This recording is composed of five waves [32]. An illustration of the ECG waveform is given in Figure 2.4. By convention, the first wave is the P wave. It represents atrial depolarisation. The next three waves (Q, R, S) happen in rapid succession and are usually grouped to form the QRS complex. The QRS complex corresponds to ventricular depolarisation. Finally, the T wave represents ventricular repolarisation. The duration between the Q wave and the T wave is called the *QT interval*. It is correlated with APD_{90} [38], as shown in Figure 2.4. As with APD_{90}, prolongation of the QT interval is correlated with the development of arrhythmia [38]. In particular, QT prolongation heightens the risk of developing the potentially life-threatening TdP [38].

Variation in the shape of the ECG complicates its analysis. Depending on where the measurement is taken, the QRS complex presents different shapes. For example,

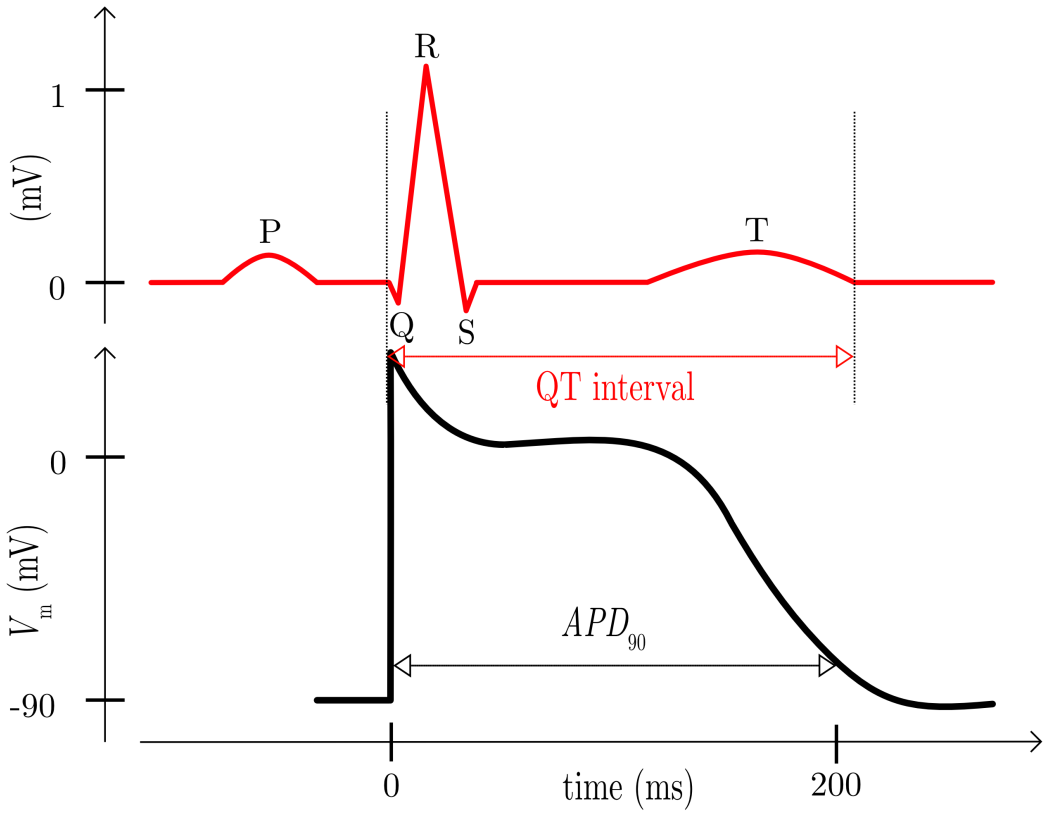


Figure 2.4: Sketch of a typical ECG waveform, compared with a typical ventricular action potential. The P, Q, R, S, T waves comprising the ECG are labeled. The correlation between the QT interval and APD_{90} is illustrated. Figure adapted from [30, 38].

the QRS complex may lack a Q wave [30]. Certain people also display an atypical waveform, for example, the polarity of the T wave may be inverted [33]. This phenomenon, called *T-wave inversion*, is common in children [39]. It can also happen as a result of a myocardial infarction. The variations in the shape of the Q and T wave complicate their identifications [40, 41]. The difficulty in their identifications translates to a potential imprecision in the measurement of the QT interval. This potential imprecision complicates any diagnosis of arrhythmia based on the QT interval measurement.

2.2 Drug cardiac safety testing

The current drug cardiac safety testing guidelines draw on our understanding of cardiac electrophysiology. The International Council on Harmonization of Technical Requirements for Registration of Pharmaceuticals for Human Use (ICH) guidelines S7B and E14 define procedures to detect potentially pro-arrythmic drug compounds. The ICH S7B guideline recommends an *in vitro* assay to detect whether a drug or its metabolites block the I_{Kr} current (hERG block) [3]. As the I_{Kr} current contributes to action potential repolarisation (see Section 2.1.1), hERG block prolongs cardiac repolarisation. This prolongation of cardiac repolarisation can be observed by increases in APD_{90} at the level of a cell, or increases in the QT interval at the level of the heart. As stated in Section 2.1, the prolongation of cardiac repolarisation is linked with arrhythmia. The ICH S7B makes use of this correlation to screen for potential pro-arrhythmic compounds. Drugs causing hERG block are discouraged from further development. However, the block of other ionic currents can compensate for the prolongation of cardiac repolarisation caused by hERG block. For example, the drug verapamil blocks the I_{CaL} current in addition to I_{Kr} [42] and is considered to be clinically safe [43].

In addition to the assessment of hERG block, the ICH S7B guidelines recommend the preclinical evaluation of the effect of a candidate drug on the QT interval [3]. This evaluation is conducted using *in vivo* animal models. Drugs that prolong the QT interval are considered to carry a pro-arrythmic risk. This risk often leads pharmaceutical companies to terminate the development of the drug [3]. The preclinical assessment of QT prolongation recommended by the ICH S7B guidelines is complemented by a clinical assessment recommended by the ICH E14 guidelines. The ICH E14 guidelines suggest the measurement of the heart-rate-corrected QT interval in treated patients during clinical development.[2] This evaluation is known as the thor-

[2]The heart-rate-corrected QT interval is the result of the division of the QT interval by a function

ough QT study. A statistically clear drug-induced increase of more than 10 ms in the heart-rate-corrected QT interval flags the evaluated drug for pro-arrythmic risk. Although QT prolongation is associated with the occurrence of TdP [46], it is known that the prolongation does not necessarily lead to TdP [47, 48].

The CiPA initiative [3], already presented in Chapter 1, aims to develop a mechanistic approach that determines the TdP risk of candidate drugs with more specificity than the methods recommended by the ICH S7B and E14 guidelines. To achieve this goal, the CiPA initiative relies on the use of hECT [3, 49].

2.3 Human engineered cardiac tissue

Human engineered cardiac tissue is an attractive *in vitro* experimental model for *in vivo* cardiac tissue (see Chapter 1). The wide availability of hiPSC-CMs [10] has allowed a reliable production of hECT composed of hiPSC-CMs. However, concerns about the immaturity of hiPSC-CM hECT limits its use. In addition, the existence of hiPSC-CM phenotypic subtypes is a subject of controversy. Here, we discuss the topics of hiPSC-CM hECT production, maturation and cellular phenotypes.

Takahashi and colleagues ushered in a new era of tissue engineering in 2007 [9] by describing how human fibroblasts can be reprogrammed to a pluripotent state. The cells obtained via this reprogramming are called hiPSCs. Zhang and co-workers extended the work of Takahashi *et al.* by demonstrating in 2009 [50] that hiPSCs can be further differentiated into hiPSC-CMs. Combined, the breakthroughs by Takahashi *et al.* and Zhang *et al.* opened the doors for the reliable generation of stem-cell derived CMs devoid of the ethical concerns surrounding embryonic-stem-cell-derived CMs. These discoveries in the manipulation of cellular identity were accompanied by engineering feats in the assembly of stem-cell-derived CMs into tissue. The first

of the heart rate. The correction preferred by the Food and Drugs Administration [44] is Fridericia's formula. Please refer to [45] for a review of the different correction formulae.

human cardiac tissue was engineered in 2007 by Caspi *et al.* [51] from human embryonic stem cells. In 2011, Tulloch and co-workers [52] demonstrated for the first time that it is possible to generate a hECT composed of hiPSC-CMs. Today, the immaturity of hECT is the main remaining drawback for its use as a substitute for adult native cardiac tissue [53]. The immature phenotype of hECT is characterised by both a contraction force and an electrical conduction velocity that are lower than typically measured in adult native cardiac tissue [53]. Strategies to mature hECT include mechanical loading, electrical pacing, hydrodynamic stimulation, long-term culture, material cues from scaffolds and a three-dimensional environment [53–55].

The hiPSC-CMs which compose hECT have been classified into three different phenotypes [20]. These phenotypes bear resemblance to the atrial, ventricular and nodal phenotypes found in the native human heart. As a consequence, the phenotypes were termed AL, VL and nodal-like. Representative action potential traces of AL, VL and nodal-like hiPSC-CMs can be seen in Figure 2.5. Ma *et al.* (2011) [20] classified hiPSC-CMs into the three phenotypes based on characteristics of the action potential waveform. The characteristic used to distinguish between AL and VL hiPSC-CMs is the length of the plateau phase. Action potentials with shorter plateau phases were classified as AL, and action potentials with longer plateau phases were classified as VL. Following this definition, AL action potentials appear more triangular than VL action potentials. Finally, action potential traces with a higher resting potential, a smaller upstroke amplitude, and a slower upstroke than those of AL and VL hiPSC-CMs were classified as nodal-like.

The categorisation of hiPSC-CM into AL, VL and nodal-like was disputed by Du *et al.* (2015) [56], who suggested that characteristics of the action potential of hiPSC-CMs instead follow a (unimodal) normal distribution. In spite of the results of Du *et al.*, later studies supported the hypothesis that discrete hiPSC-CMs phenotypes can be discerned. Chen *et al.* (2017) [57] found that AL, VL and nodal-like hiPSC-

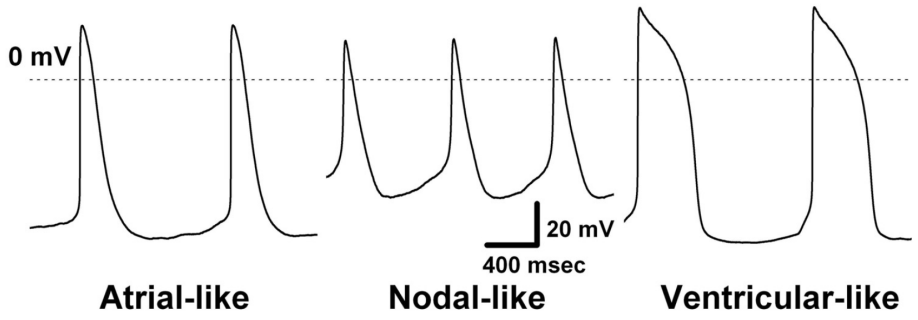


Figure 2.5: Representative action potential waveforms for different hiPSC-CM phenotypes. The AL, VL and nodal phenotypes are shown. Figure adapted from [20] with permission from The American Physiological Society.

CMs could be distinguished by a transcriptomic analysis. The shape of the action potential of each of the three phenotypes closely resembled the characterisation by Ma *et al.* [20]. In addition, Cyganek *et al.* (2018) [58] detected AL and VL hiPSC-CMs by immunocytochemical staining of cardiac subtype–specific proteins. As in [57], the AL and VL action potentials present the characteristic waveforms described by Ma and co-workers. In this study, we assume that hECT is composed of discrete hiPSC-CM phenotypes, following Ma *et al.* (2011) [20].

2.4 Conclusion

In this chapter, we presented different types of measurements of the electrical activity of cardiac tissue. We focused on their uses in the detection of arrhythmia. The current guidelines for the detection of proarrhythmic drugs during pharmaceutical development were also outlined. Finally, we presented the characteristics of a promising new *in vitro* model for drug testing, hECT. In the next chapter, we present a mathematical model of the electrophysiological behaviour of hECT.

Chapter 3

Mathematical models of cardiac electrophysiology

In this thesis, we study the effects of drugs on hECT with *in silico* and *in vitro* methods. Our *in silico* method makes use of various mathematical models. Here, we present these models. The models describe objects that exist at disparate spatial scales which range from subcellular to tissue-level. To model the effects of drugs on hECT we combine these models in a larger, multiscale model. A diagram presenting the organisation of the components of this model can be found in Figure 3.1. In Section 3.1, we present models of cellular electrophysiology that are relevant for our work, including the model of hiPSC-CMs that we use. In Section 3.2, we present how this model of hiPSC-CMs can be modified to account for drug effects. The models necessary to simulate hECT electrophysiology are introduced next. In Section 3.3, the bidomain model of cardiac tissue electrophysiology is introduced. In Section 3.4, we present how the different hiPSC-CM phenotypes can be integrated into the bidomain model. In Section 3.5, we introduce the model we use to capture the distribution of hiPSC-CM phenotypes within hECT. Finally, Section 3.6 summarises the content of this chapter.

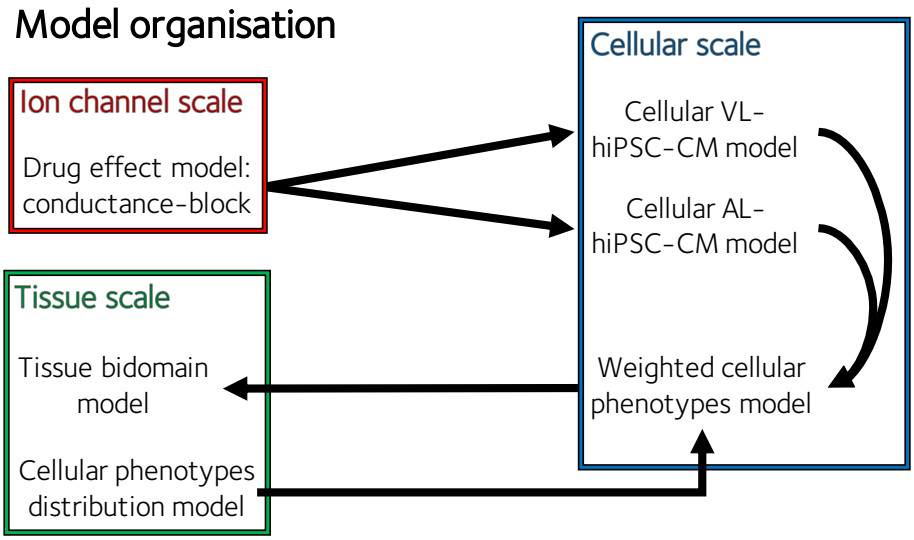


Figure 3.1: Organisation of the electrophysiological model into its different components. The different components are distributed on different lengthscales (ion channel, cell and tissue). The lengthscale of an ion channel is 10 nm. The lengthscale of a CM is 50 µm. The length of the hECT in the experiments we model is 6 mm.

3.1 Models of cellular electrophysiology

Here, we introduce mathematical models of cellular action potentials that are relevant for our work. In Section 3.1.1, we introduce the foundational Hodgkin-Huxley model, whose structure is similar to the hiPSC-CM model we use in this thesis. In Section 3.1.2, we present the first model of a cardiac cell, the Noble (1962) model. We conclude this section by presenting the model of hiPSC-CM action potentials we use in this thesis, the Paci (2013) model (Section 3.1.3).

3.1.1 The Hodgkin-Huxley model

The first biophysical mathematical model of an action potential was derived by Hodgkin and Huxley in 1952 [59]. Although the Hodgkin-Huxley model describes neural action potentials, the model structure is retained in the model of hiPSC-CM action potentials we use in this thesis. Here, we give a brief introduction to the Hodgkin-Huxley model. In this model the current across the cell membrane is as-

sumed to be either capacitive or ionic. This assumption leads to the equation [60]

$$C_{\mathrm{m,cell}}\frac{\mathrm{d}V_{\mathrm{m,cell}}}{\mathrm{d}t} = -I_{\mathrm{ion,cell}}(V_{\mathrm{m,cell}}), \tag{3.1}$$

where $V_{\mathrm{m,cell}}$ is the membrane potential of a single cell, $C_{\mathrm{m,cell}}$ is the capacitance of the cell, and $I_{\mathrm{ion,cell}}$ is the sum of the ionic currents across the membrane. Let us consider in more detail one of the ionic currents considered by Hodgkin and Huxley. A neural potassium current denoted by I_{K} was modelled by Hodgkin and Huxley using Equation (2.3). Equation (2.3) requires the specification of a potassium conductance, g_{K}. Hodgkin and Huxley modelled this conductance with the equation

$$g_{\mathrm{K}} = \bar{g}_{\mathrm{K}} n^4, \tag{3.2}$$

where $\bar{g}_{\mathrm{K}}$ is a constant denoting the maximum potassium conductance and n is a dimensionless variable that can vary between 0 and 1. Equation (3.2) indicates that n controls the porosity of the cell membrane to potassium ions. As this porosity can be conceived of as the open or closed state of potassium gates within the membrane, n is called a *gating variable*. The dynamics of this gating variable is governed by

$$\frac{\mathrm{d}n}{\mathrm{d}t} = \alpha_n\,(1-n) - \beta_n n, \tag{3.3}$$

where α_n and β_n are rate constants that vary with $V_{\mathrm{m,cell}}$. These rate constants are determined by fitting experimental data. The other currents considered by Hodgkin and Huxley are a sodium current and a *leakage* current carried by chloride and other ions. Like I_{K}, these currents were modelled using Equation (2.3). Two gating variables (m and h) are used in the description of the sodium current, while none is used in the description of the leakage current.

The Hodgkin-Huxley model [59] is remarkable for synthesizing multiple experi-

mental findings [61–64] into a mechanistic model whose simulation successfully reproduced experimental data. The model forms the basis of our modern quantitative understanding of neuronal action potentials [65].

3.1.2 The Noble (1962) model

The first mathematical model of the action potential of a cardiac cell was an extension of the Hodgkin-Huxley model. It was developed in 1962 by Noble [15]. In this model, the potassium current of the Hodgkin-Huxley model is split into an inward rectifier potassium current, I_{K1}, and a delayed-rectifier current, I_{K2} [66]. The I_{K2} current corresponds to an efflux of potassium ions from the cell with a delay after membrane repolarisation.

The Nobel (1962) model successfully reproduces the action potential waveform of Purkinje fiber cells [67], which are part of the conducting tissue of the heart ventricle (see Chapter 2). In addition, the time course of potassium current was successfully reconstructed. The main limitation of the Noble (1962) model is that it does not include any calcium current [37]. The model compensated for this lack of calcium current by altering the formulation of the m gating variable in the sodium current. This alteration made the sodium current longer lasting. In turn, this change in the sodium current dynamics resulted in a simulated plateau that matched experimental observations. However, the alteration was not supported by experimental evidence and was later found to be incorrect (e.g. with the discovery of the calcium current [68]).

In spite of this inaccuracy, the Noble (1962) model [15] pioneered the quantitative description of the electrophysiological behaviour of cardiac cells. The influence of this model can still be observed today from the large number of cardiac action potential models that inherited formulations from it (for a review see [67, 69]). Modern adaptations of the two potassium currents introduced by the Noble (1962) model are

present in the hiPSC-CM electrophysiocal model used in this thesis.

3.1.3 The Paci (2013) model

The first mathematical model of hiPSC-CMs was developed by Paci in 2013 [16]. We refer to this model as Paci2013 hereafter. The model is based on experimental data [20] of the iCell cell line of hiPSC-CMs (available from Cellular Dynamics International). It was shown to capture the characteristic spontaneous beating observed in hiPSC-CMs [16]. Two versions of the model are used in order to account for the differences between AL and VL CMs. Newer VL hiPSC-CM models were developed by Koivumäki *et al.* (2018) [70] and Paci *et al.* (2018) [19]. In particular, these newer models better capture calcium dynamics. However, no newer AL hiPSC-CM model is available. As a result, we choose to model both AL and VL hiPSC-CMs with the Paci2013 model in this thesis. This choice allows us to be sure that differences in the AL and VL hiPSC-CMs models reflect the underlying physiology and do not originate from different modelling methodologies.

The Paci2013 model consists of a coupled system of 92 algebraic and ordinary differential equations. The equations share a similar structure with the foundational Hodgkin-Huxley model [59], including the use of equilibrium potentials (see Chapter 2) and gating variables (see Section 3.1.1). The equations in the Paci2013 model describe the transmembrane currents created by the movement of ions across the membrane of hiPSC-CMs. The Paci2013 model outputs $I_{\text{ion,cell}}$ – $I_{\text{ion,a}}$ for the AL model and $I_{\text{ion,v}}$ for the VL model – such that

$$I_{\text{ion,cell}} = \sum_{\textbf{channels}} I_{chan} + \sum_{\textbf{others}} I_o, \tag{3.4}$$

where **channels** denotes the vector of ion channel current names used by the model and **others** the vector of pump and exchanger current names. In particular, the

current of the ion channel *chan*, denoted by I_{chan}, verifies the proportionality relation

$$I_{chan} \propto g_{chan}, \tag{3.5}$$

where g_{chan} represents the conductance of the ion channel. The output of the Paci2013 model can be used to simulate the cellular membrane potential $V_{\text{m,cell}}$ via Equation (3.1) and the initial condition

$$V_{\text{m,cell}} = -70\,\text{mV}. \tag{3.6}$$

The formulations of several membrane ionic currents in the Paci2013 model were calibrated against experimental ion current data collected by Ma *et al.* [20]. The formulations of the other currents were based on a previous model of human embryonic stem cell derived CMs [71]. The parameters of these other currents were optimised to obtain a simulated action potential shape that matched experimental action potential data. Like the experimental ion current data, the experimental action potential data were obtained from [20]. A weakness of the methodology followed by Paci *et al.* lies in the optimisation procedure used to calibrate the parameters of the latter currents. This procedure does not guarantee that the chosen parameters are physiological. As a result, the validity of the description of the latter currents by Paci *et al.* is questionable. In spite of this weakness, the Paci2013 model is notable for enabling *in silico* study of both the AL and VL phenotypes of hiPSC-CMs. In particular, the effects of drugs on AL and VL hiPSC-CMs can be investigated theoretically thanks to the Paci2013 model.

3.2 Drug conductance block model

In this work, we analyse the effect on hECT of drugs that block certain ion channels. The cellular models presented so far can be modified to capture the effects of drugs. In particular, the Paci2013 model utilises parameters g_{chan} that represent the conductance of the ion channel *chan*. The conductance is a function of the drug concentration, $[D]$, such that $g_{chan} = g_{chan}([D])$. In the presence of a pharmaceutical drug that blocks the ion channel by binding to it, g_{chan} is reduced. The factor by which g_{chan} is reduced can be calculated from the Hill equation [72] that describes the binding of a ligand to a macromolecule. In particular, this equation is appropriate to model the binding of a small molecule drug to an ion channel membrane protein [73]. In the presence of a drug, g_{chan} can be calculated using the conductance-block model

$$g_{chan}([D]) = g_{chan}(0)\left(1 + \left(\frac{[D]}{[IC_{50}]_{chan}}\right)^{n_{chan}}\right)^{-1}, \tag{3.7}$$

where $g_{chan}(0)$ denotes the conductance of *chan* in the absence of drug, $[IC_{50}]_{chan}$ the concentration of the drug at which the conductance of the ion channel is reduced by half, and n_{chan} is the hill coefficient.

3.3 The bidomain model

There are about 40,000 to 60,000 hiPSC-CMs per cm^2 of two-dimensional hECT. To capture their combined behaviour, the cellular Paci2013 model is coupled to a tissue model called the bidomain model. The bidomain model is used to simulate the electrophysiological activity at the scale of the tissue in our study. According to [74], the bidomain model was first suggested by Otto Schmitt in 1969 [75] and put into its current form by scientists between the late 1970s [76–78] and the late 1980s [79–83]. The bidomain model takes its name from the fact that it is spatially defined over two

domains which coexist at each spatial point. The two domains are the extracellular domain and the intracellular domain.

The bidomain model describes the evolution in time, t, of two properties that are defined at every position, $\boldsymbol{r} = (x, y)$, on the spatial domain, Ω. The two properties described by the bidomain model are V_m and V_e. The bidomain model consists of the two coupled partial differential equations [84]

$$\nabla \cdot \left(\left(\boldsymbol{\Sigma}_\mathrm{i} + \boldsymbol{\Sigma}_\mathrm{e} \right) \nabla V_\mathrm{e} + \boldsymbol{\Sigma}_\mathrm{i} \nabla V_\mathrm{m} \right) = 0, \tag{3.8}$$

$$\chi \left(C_\mathrm{m} \frac{\partial V_\mathrm{m}}{\partial t} + I_\mathrm{ion} \right) - \nabla \cdot \left(\boldsymbol{\Sigma}_\mathrm{i} \nabla \left(V_\mathrm{m} + V_\mathrm{e} \right) \right) = 0. \tag{3.9}$$

The net sum of the cell transmembrane ionic currents per unit length is denoted by I_ion and the capacitance of the cell membrane per unit length is denoted by C_m. The values for I_ion and C_m are provided at every position on the tissue by the weighted cellular phenotypes model that we describe next in this chapter. The tensors $\boldsymbol{\Sigma}_\mathrm{i}$ and $\boldsymbol{\Sigma}_\mathrm{e}$ are scalar multiples of identity matrices, reflecting the assumption that the conduction of electricity in the tissue is isotropic. Finally, the length of cell membrane per unit area of tissue is denoted by χ.

The bidomain equations (3.8) and (3.9) are subject to the no-flux boundary conditions

$$\boldsymbol{n} \cdot \left(\boldsymbol{\Sigma}_\mathrm{i} \nabla \left(V_\mathrm{m} + V_\mathrm{e} \right) \right) = 0, \tag{3.10}$$

$$\boldsymbol{n} \cdot \left(\boldsymbol{\Sigma}_\mathrm{e} \nabla V_\mathrm{e} \right) = 0, \tag{3.11}$$

where $\boldsymbol{n}$ is the outward unit vector normal to the cardiac tissue boundary, $\partial\Omega$. The initial condition is

$$V_\mathrm{m}(\boldsymbol{r}, t = 0) = -70\,\mathrm{mV}. \tag{3.12}$$

The system presented so far specifies V_e only up to a constant. Several methods exist to specify this constant. These methods include fixing the integral of V_e over the domain, or fixing the value of V_e over a subset of mesh nodes [84]. The choice of the method depends on the system modelled. We will specify the method used in this thesis once the experimental system has been introduced.

3.4 Weighted cellular phenotypes model

The tissue-scale bidomain model relies on input derived from a cell-scale model. Here, we model a tissue consisting exclusively of AL and VL hiPSC-CMs. We represent the two cellular phenotypes within the bidomain model by using the weighted cellular phenotypes model introduced in 2018 by Bowler et al. [21]. This model was derived through a homogenisation method that relies on the fact that the characteristic length scale of the local fluctuations in the properties of the tissue, l, is small compared to the characteristic length scale of the conduction of electricity in the tissue, L, i.e. that

$$l \ll L, \tag{3.13}$$

where l represents the length of a repeated unit that contains several cells and L the length scale over which V_m varies.

The weighted cellular phenotypes model defines the parameters C_m and I_{ion} of the bidomain tissue model to be averages weighted by the proportion of cell membrane length occupied by AL hiPSC-CMs, ρ_a, and VL hiPSC-CMs, ρ_v, such that

$$C_m = \rho_a C_{m,a} + \rho_v C_{m,v}, \tag{3.14}$$

$$I_{ion} = \rho_a I_{ion,a} + \rho_v I_{ion,v}, \tag{3.15}$$

$$\rho_a = 1 - \rho_v, \tag{3.16}$$

where the subscript a denotes AL hiPSC-CMs and v denotes VL hiPSC-CMs. The capacitance of the AL-hiPSC-CM cell membrane per unit length is $C_{\mathrm{m,a}}$ and the VL capacitance is $C_{\mathrm{m,v}}$. Similarly, $I_{\mathrm{ion,a}}$ is the net sum of the AL-hiPSC-CM transmembrane ionic currents per unit length and $I_{\mathrm{ion,v}}$ the VL currents. Equation (3.14) and Equation (3.15) can also be used to compute $C_{\mathrm{m,cell}}$ and $I_{\mathrm{ion,cell}}$ for the simulation of $V_{\mathrm{m,cell}}$ with Equation (3.1).

3.5 Phenotype distribution model

The weighted cellular phenotypes model requires specification of the proportion of cell membrane length occupied by VL hiPSC-CMs, ρ_{v}. To specify ρ_{v}, we notice that CMs derived from stem cells were shown to spatially cluster by phenotype (including the AL and VL phenotypes) [23]. We model this observation by considering that the proportion of VL hiPSC-CMs in the tissue, at a given position, $\rho_{\mathrm{v}}(\boldsymbol{r})$, and the proportion at a nearby position, $\rho_{\mathrm{v}}(\boldsymbol{r}+\Delta\boldsymbol{r})$, are random variables that are highly correlated. Further, we assume for convenience that $\rho_{\mathrm{v}}(\boldsymbol{r})$ and $\rho_{\mathrm{v}}(\boldsymbol{r}+\Delta\boldsymbol{r})$ are sampled from a bivariate normal distribution. We generalise and detail these modelling principles for the whole tissue by assuming that ρ_{v} is a realisation of a Gaussian random field with mean μ and a Gaussian covariance function such that

$$\mathrm{Cov}(\rho_{\mathrm{v}}(\boldsymbol{r}_1), \rho_{\mathrm{v}}(\boldsymbol{r}_2)) = \sigma^2 \exp\left(\frac{-||\boldsymbol{r}_1 - \boldsymbol{r}_2||^2}{l_{\mathrm{c}}^2}\right), \tag{3.17}$$

where $\boldsymbol{r}_1$ and $\boldsymbol{r}_2$ are two positions in the tissue, σ is the standard deviation of $\rho_{\mathrm{v}}(\boldsymbol{r})$, l_{c} is the spatial correlation length, and $||\cdot||$ is the Euclidean distance.

3.6 Conclusion

In this chapter, we detailed key models of cellular electrophysiology, including the Paci2013 model used in this thesis. We then presented how the Paci2013 model could be modified to describe the effect of ion-channel-blocking drugs. Finally, we showed how the cellular Paci2013 model could be integrated at the scale of hECT. In summary, we presented a multiscale mathematical model of the electrophysiological behaviour of hECT subject to drugs. In the next chapter, we focus on presenting the simulation of the multiscale model.

Chapter 4

Simulation and signal processing of the electrophysiological response of engineered cardiac tissue to drugs

In this chapter, we present our method to enable study of the electrophysiological response of engineered cardiac tissue to drugs. In Section 4.1 we present the experimental system modelled, along with the necessary adaptations to the standard mathematical models presented in Chapter 3. In Section 4.3 we present and verify the simulation framework. In Section 4.4 we present and test the novel signal processing methods required to analyse the experimental and simulated measurements. In Section 4.5 we introduce the methods we employed to reduce computational expense while keeping the error introduced within acceptable bounds. Finally, Section 4.6 discusses the choices made to enable the study of drug effects on hECT.

4.1 Experimental set-up

A detailed technical description of the experimental protocol is available in Section A.1. Here, we summarise the aspects directly relevant to the mathematical

model.

The experimental system consists of a cellular monolayer composed of CDI (iCell Cardiomyocytes2, Cellular Dynamics International) hiPSC-CMs. Experimental data were recorded using the CardioExcyte96 device (Nanion Technologies, Germany) [85]. A single cellular monolayer was seeded in each of the 96 culture chambers of a microplate that was inserted in the recording device. The monolayer rested on a fibronectin coating and was covered by culture medium. It was not electrically stimulated. The two-dimensional arrangement of cells within the monolayer has been experimentally observed not to display any anisotropies. Neither the proportion of the different hiPSC-CM phenotypes present in the monolayer nor their spatial distribution was controlled. Electrophysiological measurements were performed using two electrodes that are located at the bottom of the wells enclosing the culture chambers. The recording electrode is located at the centre, while the reference electrode is located near the boundary. A visualisation of the experimental set-up is provided in Figure 4.1 and the geometry of the bottom of each culture chamber is precisely specified in Figure 4.2.

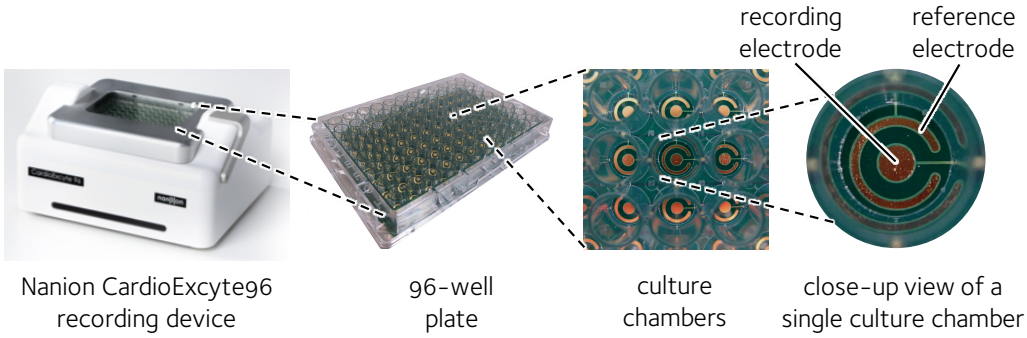


Figure 4.1: Visual presentation of the experimental set-up. Figure adapted with permission from [85] with the kind help of Nanion Technologies, Germany.

The CardioExcyte96 device measures the field potential signal (FPS) over time, t, such that

$$FPS(t) = \overline{V_{\mathrm{e}}(\boldsymbol{r}, t)}^{\mathrm{rec}}, \tag{4.1}$$

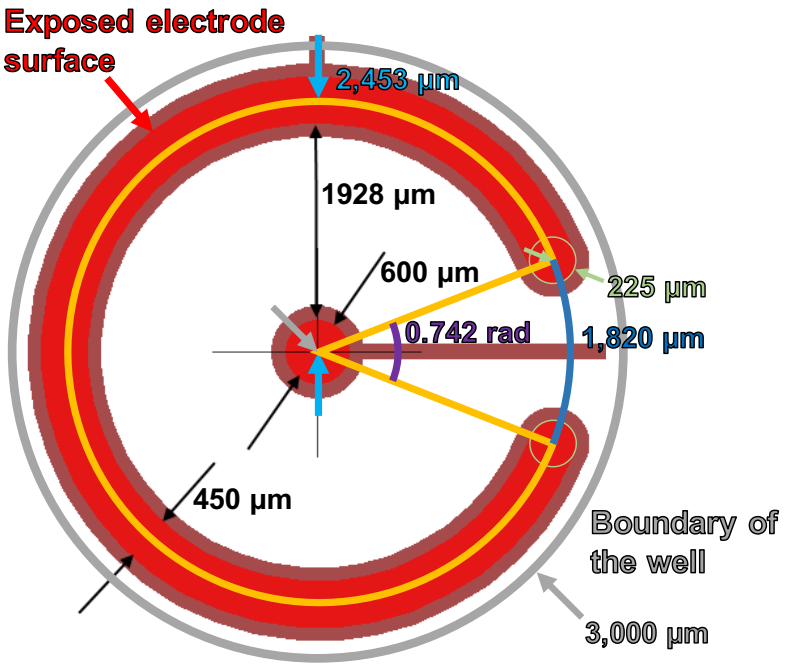


Figure 4.2: Geometry of the bottom of the culture chamber of each well, including the positions and measurements of the electrodes. The outer C-shaped electrode is the reference electode and the inner disc-shaped electrode is the recording electrode. The ends of the C-shaped electrodes can be described by half-circles of radiuses 225 µm as shown in the figure. The exposed electrode surfaces are indicated in bright red. The brown regions are made of copper that is electrically insulated from the rest of the tissue by varnish. The brown regions do not contribute to the measurement. Figure adapted with permission from an original diagram and measurements graciously provided by Nanion Technologies, Germany.

where $FPS(t)$ is the FPS at time t and $V_\mathrm{e}(\boldsymbol{r}, t)$ is the extracellular electrical potential, V_e, at position $\boldsymbol{r}$ and time t. (Some authors [86, 87] refer to the FPS as the extracellular field potential (EFP)). The superscript rec corresponds to the recording electrode, and the bar symbol represents a spatial average, such that the average of $V_\mathrm{e}(\boldsymbol{r}, t)$ over the recording electrode is denoted by $\overline{V_\mathrm{e}(\boldsymbol{r}, t)}^{\mathrm{rec}}$. The FPS in each well was recorded in the presence and in the absence of drugs. In total, the effects of 12 different drugs at four different concentrations were recorded. For each drug and each concentration, up to five replicates were performed: i.e., a drug at a given concentration was added to up to five different hiPSC-CM monolayers located in up to five different wells. The FPS was recorded every 15 min for 30 s in what is known as a *sweep*. The experiments

$[Ca^{2+}]_e$	$[Na^+]_e$	$[K^+]_e$	$[Mg^{2+}]_e$
1.5	115.0	4.0	1.0

Table 4.1: Extracellular ionic concentrations in the experiments modelled in this work. The concentrations are given in mM.

were performed at 37°C with the extracellular ionic concentrations given in Table 4.1.

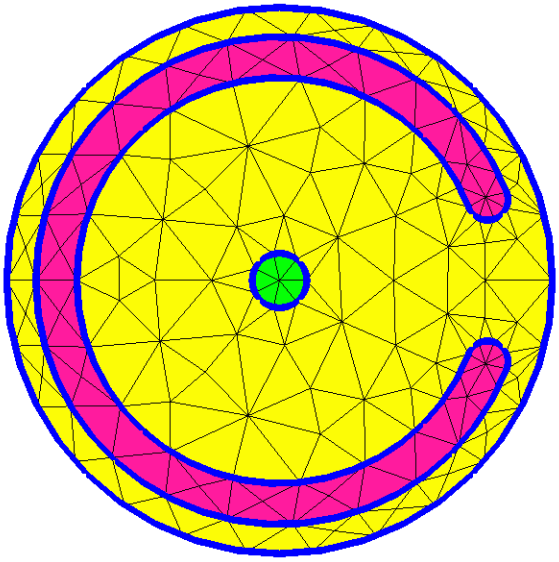


Figure 4.3: Finite element mesh modelling of the geometry of the bottom of each culture chamber. The mesh is partitioned into different subdomains that are indicated with different colours. The reference electrode is coloured in pink, the recording electrode in green, and the remaining domain is coloured in yellow. The blue lines indicate the separations between the different subdomains. The mesh shown contains 152 nodes, 276 triangular elements and has a maximum inter-node spacing of 750 µm. The dimensions of the domain and subdomains are specified in Figure 4.2.

4.2 Model adaptations

The spatial domain is a disc of radius 3000 µm which corresponds to the surface of the bottom of the well. We discretise the geometry of the bottom of the well with a finite element mesh made of triangular elements. The mesh utilised in this study is illustrated in Figure 4.3. The mesh was generated using the Gmsh software [88], which allows specification of a maximum inter-node spacing.

The mathematical models used to describe the electrical activity of the hECT have been described in Chapter 3. Here, monolayers only consist of hiPSC-CMs and we make the simplifying assumption that they can be of only two different cellular phenotypes that are AL or VL. We neglect the nodal-like phenotype as it is the rarest iCell hiPSC-CM phenotype [20]. In addition, no mathematical model exists to describe the electrophysiological behaviour of nodal-like cells.

Several characteristics of the experimental tissue monolayers facilitate simplifying assumptions. We assume that the electrophysiology of the tissue does not change across the depth of the monolayer so that the tissue can be modelled as a two-dimensional sheet. In addition, we assume that the conduction of electricity in the tissue is isotropic. Moreover, the cardiac tissue is confluent and covers the bottom of each culture chamber entirely. The tissue is surrounded by the walls of a well that we consider to be an electrical insulator. Finally, the model reflects the spontaneous beating of hiPSC-CMs and the fact that no stimulus currents are used to pace the monolayers in the experiments.

Contrary to the Axion Biosystems 96-well micro-electrode array studied by Bowler in [25], the CardioExcyte96 recording device studied here has a grounding electrode. This grounding electrode enables specification of the undefined constant in V_e which was mentionned in Section 3.3. The grounding electrode is modelled by fixing the value of V_e on the reference electrode, such that

$$V_\mathrm{e} = 0. \tag{4.2}$$

As a consequence, Equation (3.8) and Equation (3.9) become

$$\nabla^{\mathbf{2}} V_\mathrm{m} = 0, \tag{4.3}$$

$$C_\mathrm{m} \frac{\partial V_\mathrm{m}}{\partial t} + I_\mathrm{ion} = 0. \tag{4.4}$$

on the reference electrode.

The extracellular ionic concentrations in the cellular model needed to be adapted. We adjusted the Ca^{2+}, Na^{+} and K^{+} extracellular concentrations in accordance with Table 4.1 (Mg^{2+} is not included in the Paci2013 model [16]). Since both our experiments and those used to calibrate the Paci2013 model were conducted at 35–37°C [16] we did not need to adjust the model for differences in temperature. The phenotype distribution model was parametrised according to the recommendation of Bowler (2018) [25], such that $\sigma = 0.075$ and $l_c = 0.2\,\text{cm}$. The average proportion of VL cells in the tissue was obtained from the study of the phenotypes of iCell hiPSC-CM by Ma *et al.* [20]. Accordingly, we have $\mu = 0.54$.

In this thesis, we continue the study of drug effects on hECT initiated by Bowler [25]. Therefore, we keep the values of the bidomain parameters as set in [25]. The parameters of the bidomain equations χ, $\boldsymbol{\Sigma}_e$ and C_m are kept at their default values set in Chaste [27], which model a tissue composed of adult CMs. The intracellular conductivity is set to $\sigma_i = 0.3\,\text{mS}\,\text{cm}^{-1}$, so that

$$\boldsymbol{\Sigma}_i = \sigma_i \boldsymbol{I}, \tag{4.5}$$

where $\boldsymbol{I}$ is the identity matrix. This intracellular conductivity is lower than the default value of $1.75\,\text{mS}\,\text{cm}^{-1}$ to reflect the slow electrical conductivity of hiPSC-CMs as compared to adult CMs. The value of σ_i chosen here was obtained by Bowler [25] from experimental wave propagation maps obtained with iCell Cardiomyocytes.

4.3 Simulation

We conduct simulations by adapting an existing implementation described in Section 4.3.1. We present the verification of the correctness of this implementation in

Section 4.3.2.

4.3.1 Implementation

The Chaste library [27], written in the C++ programming language [89], already implements the simulation specified by the tissue and the single-cell Paci2013 model. The simulations we run in this chapter make use of an existing Chaste user project that was contributed by Louise Bowler [25]. The simulation outputs for the single-cell model are $V_{\mathrm{m,cell}}$ at timesteps n and the simulation outputs for the tissue model are V_{m}, and V_{e} at timesteps n and linear spatial indices l. The linear spatial index is a scalar discrete representation of the two-dimensional position vector $\boldsymbol{r}$.

4.3.2 Verification

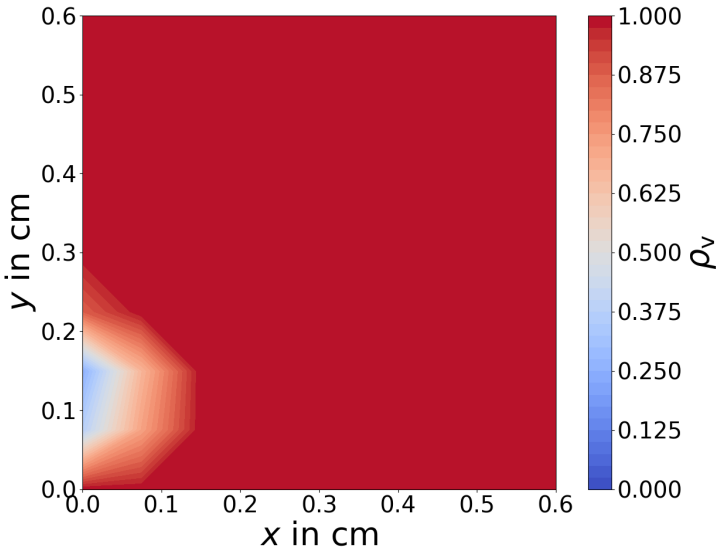


Figure 4.4: Phenotypic distribution on the square structured mesh. High values correspond to a mostly VL phenotype, while low values correspond to a mostly AL phenotype. The spatial resolution chosen for this figure is 750 µm.

We verify that the simulation is correctly implemented by comparing actual and theoretical convergence rates of appropriately chosen metrics, as the timestep or

spacestep is reduced. We carry out this analysis on a structured mesh on a square domain. With unstructured meshes such as those produced by Gmsh, the change of spacestep has complex effects on the position of the mesh nodes. Here, the structured mesh is chosen so that the positions of the computational nodes have a simple dependence on the spacestep. The square domain, Ω_{square}, has the length of the diameter of the original domain Ω presented in Figure 4.3. A simple mixed phenotypic distribution is chosen. The phenotypic distribution through the domain is shown in Figure 4.4. Finally, we adapted the condition on V_{e} set by Equation (4.2) to account for the fact that no grounding electrode is present in Ω_{square}. Instead, we take the average extracellular potential over Ω_{square} as a reference potential at each point in time [25, 84]. Formally,

$$\iint_{\Omega_{\text{square}}} V_{\text{e}} \mathrm{d}x\mathrm{d}y = 0\,\text{mV}. \tag{4.6}$$

The convergence rates of two metrics are studied. The metrics are the L^2 and L^∞ norms, defined as

$$||\Delta V_{\text{e}}||_{L^2} = \sqrt{\iiint\limits_{\substack{(x,y)\in\hat{\Omega}_{\text{square}} \\ t\in[T_{\text{start}},T_{\text{end}}]}} \Delta V_{\text{e}}^2 \mathrm{d}x\mathrm{d}y\mathrm{d}t}, \tag{4.7}$$

$$||\Delta V_{\text{e}}||_{L^\infty} = \max_{\substack{(x,y)\in\hat{\Omega}_{\text{square}} \\ t\in[T_{\text{start}},T_{\text{end}}]}} \left(|\Delta V_{\text{e}}|\right). \tag{4.8}$$

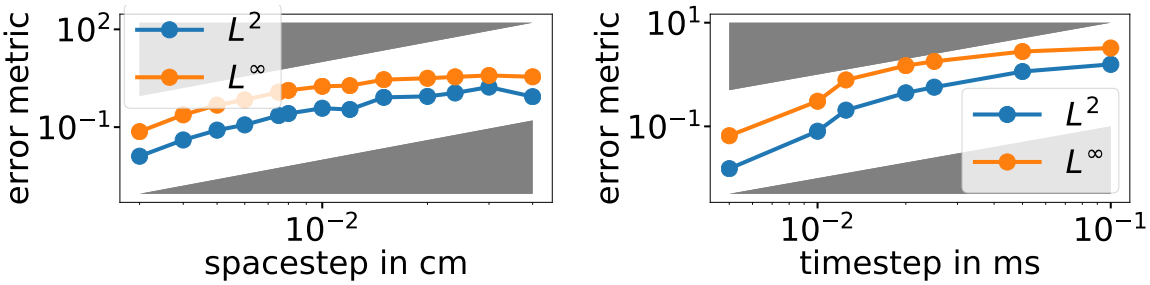
A spatial and temporal subset of the simulation output has to be chosen to compute the metrics. The parameter T_{start} corresponds to the selected start time, and T_{end} to the selected end time. Selected sample points of the square domain are denoted by $\hat{\Omega}_{\text{square}}$. The absolute value is symbolised by $|\cdot|$. The error metrics are used to evaluate the absolute difference in extracellular potential, ΔV_{e}, between a computed

solution $V_{\mathrm{e},computed}$ and a reference solution $V_{\mathrm{e,reference}}$, such that

$$\Delta V_{\mathrm{e}} = |V_{\mathrm{e},computed} - V_{\mathrm{e,reference}}|, \tag{4.9}$$

where $V_{\mathrm{e,reference}}$ is numerically computed at a very fine resolution. We had to obtain $V_{\mathrm{e,reference}}$ numerically as no analytic solution for the full model is available. The L^2 and the L^∞ metric are both predicted to converge at rate $\mathcal{O}(\Delta t)$ temporally and $\mathcal{O}(h^2)$ spatially [25], where Δt is the timestep of the simulation and h is the maximal inter-node spacing of the spatial mesh, that we call *spacestep* for short. However, this prediction only holds for sufficiently small values of the spacestep and timestep. These values are known as the *asymptotic tail*.

Figure 4.5 shows that the metrics converge at, or faster than, the theoretical convergence rates, within the asymptotic tail. This suggests that the simulation is correctly implemented. That said, we underline that this convergence analysis was conducted on Ω_{square}, which is different from Ω, and that no grounding electrode was present, contrary to the model described in Section 4.2. In Section 6.2, we recommend that a more thorough convergence analysis be conducted in future work.



(a) (b)

Figure 4.5: Convergence analysis of the simulation of the full model. The grey triangles correspond to the expected convergence rates which are respectively $\mathcal{O}(h^2)$ for the spatial convergence analysis and $\mathcal{O}(\Delta t)$ for the temporal convergence analysis, for both error metrics [25]. The spatial convergence analysis shown in Figure (a) compares the error metrics, measured at different spacesteps and a fixed timestep, to the expected convergence rates. The spacestep at which $V_{\text{e,reference}}$ is computed is 25 µm and the fixed timestep chosen is 0.01 ms. The temporal convergence analysis shown in Figure (b) compares the error metrics, measured at different timesteps and a fixed spacestep, to the expected convergence rates. The timestep at which $V_{\text{e,reference}}$ is computed is 0.004 ms and the fixed spacestep chosen is 25 µm. The results were obtained on a square mesh of length 6 mm for simplicity and sampled from 36 fixed points spaced by 1.2 mm in height and width. We chose $[T_{\text{start}}, T_{\text{end}}] = [1, 3]$ s to cover the second full beat in the simulation. The absolute tolerance chosen is 1×10^{-5}.

4.4 Signal processing

The lack of accessible software libraries allowing to detect FPS features, or hiPSC-CM-specific action potential signal features, led us to develop novel detection methods. In Section 4.4.1 we detail the signal processing methods we developed for the FPS, while in Section 4.4.2 we explain the signal processing methods developed for the hiPSC-CM action potential signal. A brief note on the implementation of these methods is given in Section 4.4.3.

4.4.1 Field potential signal processing

We transform the simulation output into a FPS to facilitate comparison with the experimental measurement specified by Equation (4.1). Specifically, we compute the FPS at any given timestep, n, denoted by $FPS|_n$, through the equation

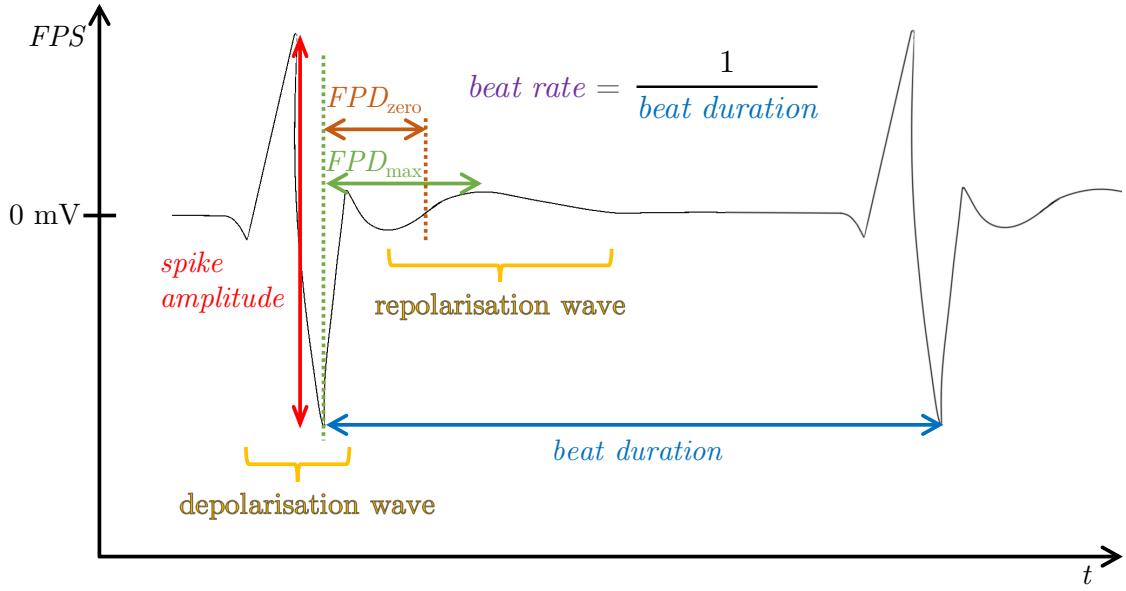


Figure 4.6: Sketch of the waveform of the field potential signal over time and visual definition of important portions and summary statistics. In actual data, the depolarisation wave happens very fast compared to the duration of a beat and looks like a straight line when visualising a full action potential. As a result, the depolarisation wave is sometimes also called a *spike*. The beat duration corresponds to the time that elapses between two consecutive spikes (see Section 4.4.1 for a more detailed definition), the beat rate is defined as the inverse of the beat duration, the spike amplitude is the peak-to-trough ratio of the depolarisation wave, FPD_{max} is the field potential duration that corresponds to the time that elapses between the depolarisation wave and the extremum of the following repolarisation wave, and FPD_{zero} is the field potential duration that corresponds to the time that elapses between the depolarisation wave and the zero crossing of the following repolarisation wave (see Section 4.4.1 for a more detailed definition).

$$FPS|_n = \frac{1}{|\mathbf{rec}|} \sum_{l \in \mathbf{rec}} V_e|_{n,l}, \tag{4.10}$$

where $V_e|_{n,l}$ is the extracellular potential evaluated at timestep n and linear spatial index l, **rec** is the vector of the linear indices of the nodes that are located in the recording electrode and $|\mathbf{rec}|$ is the number of nodes in the recording electrode.

We summarise the FPS using several summary statistics that are illustrated in Figure 4.6. A complexity in the definitions of the field potential duration (FPD) at maximum repolarisation, FPD_{max}, and the beat duration, comes from the fact that

the repolarisation wave can be inverted between two FPSs. The precise definition we use for $FPD_{\max}$ is the duration between the trough of the depolarising wave and the extremum of the following repolarising wave. The duration between the trough of the depolarising wave and the zero crossing of the following repolarisation wave is denoted by FPD_{zero}. Finally, the precise definition for the beat duration is the duration between the trough of the depolarising wave and the trough of the depolarising wave of the following beat.

We have developed signal processing algorithms to compute the summary statistics describing both the simulated FPS and the experimental FPS. These algorithms require the accurate detection of points of interest in the FPS: the peak and the trough of the depolarisation wave, and the extremum and the zero crossing of the repolarisation wave. An illustration of the detection of the points of interest on an experimental signal is provided in Figure 4.7a. The detection of the points of interest was performed by thresholding and excluding parts of the signal appropriately. A difficulty arose in the detection of the repolarisation extremum on the experimental FPS. The noise present in the experimental signal had to be removed prior to detection. This required the selection and parametrisation of a low-pass frequency filter. We chose a 3rd order Butterworth low-pass filter below 4.5 Hz. Figure 4.7b illustrates the difference between the raw experimental FPS and its filtered counterpart. Visual checks on the validity of the points of interests detected were carried out throughout the developement of our signal processing algorithm by looking at figures similar to Figure 4.7a and Figure 4.7b.

We verified that the algorithm we have developed computes the summary statistics presented in Figure 4.6 accurately by comparison with results from a commercial software (CardioExcyte Control 96, Nanion Technologies). We performed the detection on the FPS from drug-free and ranolazine-perturbed experiments. The beat rate values computed by our algorithm match very closely those computed by CardioEx-

cyte Control 96 (see Figure 4.8a). Good agreement is also achieved for $FPD_{\max}$ as can be seen in Figure 4.8c. In the rest of this chapter we are also interested in the relative change in biomarkers after a drug is added to the system. We define, a relative change, Δ_{rel}^{SS}, in a summary statistic, SS, between an experiment with a drug at concentration $[D]$ and a control experiment without the drug, as

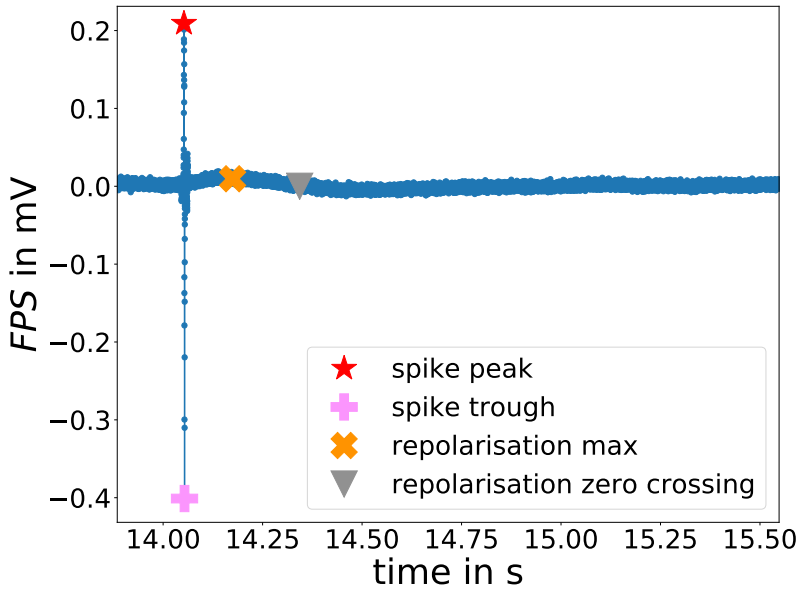
$$\Delta_{\text{rel}}^{SS} = \frac{SS^{[D]} - SS^{\text{control}}}{SS^{\text{control}}}. \tag{4.11}$$

Acceptable agreements in $\Delta_{\text{rel}}^{beat\ rate}$, $\Delta_{\text{rel}}^{FPD_{\max}}$ and $\Delta_{\text{rel}}^{FPD_{\text{zero}}}$ are presented in Figure 4.8b.

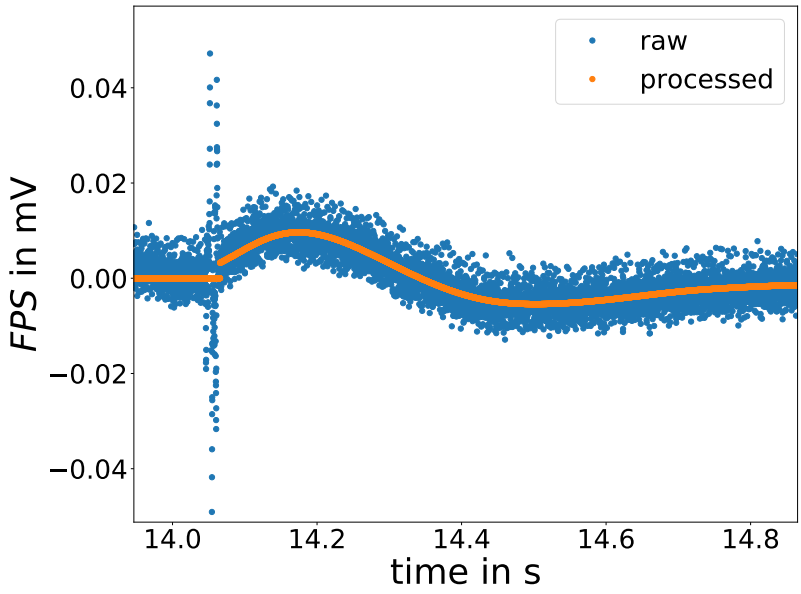
Minor discrepancies between our algorithm and CardioExcyte Control 96 occur at ranolazine concentration, $[D_{\text{r}}]$, 1000 nM and 10 000 nM for $\Delta_{\text{rel}}^{FPD_{\max}}$ and $\Delta_{\text{rel}}^{FPD_{\text{zero}}}$. After investigation, we discovered that this discrepancy comes from a difference in data aggregation between our algorithm and CardioExcyte Control 96. While our algorithm takes the median value of the summary statistics detected in a sweep, CardioExcyte Control 96 determines the morphology of the average beat in the *FPS* sweep, and detects the summary statistic on this averaged beat. In most cases the two methods give similar results. However, discrepancies can arise in two cases. The first case is when the zero crossing or the maximum is flat. In this case, the detection is very sensitive to the data aggregation method. The second case is when the summary statistics are bimodally distributed within one sweep. For example, we investigated the trace of well F10 with $[D_{\text{r}}] = 1000$ nM. In this trace, the first five beats have a distinct morphology from the rest, including earlier repolarisations (see Figure 4.9). The averaging process implemented in CardioExcyte Control 96 creates an average mean beat with an artificially flat repolarisation extremum where detection is ambiguous. On the contrary, the median taken by our algorithm effectively eliminates the $FPD_{\max}$ calculated on the first five beats and gives the value averaged over the rest of the beats. This procedure is more meaningful than the averaging

because it outputs an observed $FPD_{\max}$ that is representative of the distribution of $FPD_{\max}$ within the sweep. By contrast, the averaging creates an unobserved $FPD_{\max}$ that is not representative of the bimodal distribution of $FPD_{\max}$ within the sweep. This explains the difference in relative changes between our algorithm and Nanion's.

Lastly, a subtle difference in $FPD_{\max}$ and FPD_{zero} values exists between our algorithm and Nanion's. The reason for this difference is that the filter that we chose introduces a slight delay of about 10 ms in the signal. As we filter the repolarisation wave, this delay explains the slight differences in values between our algorithm and that of CardioExcyte Control 96 for $FPD_{\max}$ and FPD_{zero}. These differences can be observed in Figure 4.8c and Figure 4.8e. Given the small size of this delay and the focus of this thesis on relative changes rather than absolute values, we choose to accept the slight differences.



(a)



(b)

Figure 4.7: Illustration on an experimental signal of the detection of the peak and the trough of the spike, as well as the extremum of the repolarisation wave. Figure (a) shows the FPS during one beat with markers indicating the spike peak, trough, repolarisation extremum and repolarisation zero crossing. Figure (b) shows a close-up of the repolarisation wave with the processed signal overlayed on top of the raw signal. The raw signal is processed with a lowpass filter and a zero-out of the depolarisation wave. The signal shown in this figure comes from the control experiment conducted in well F9.

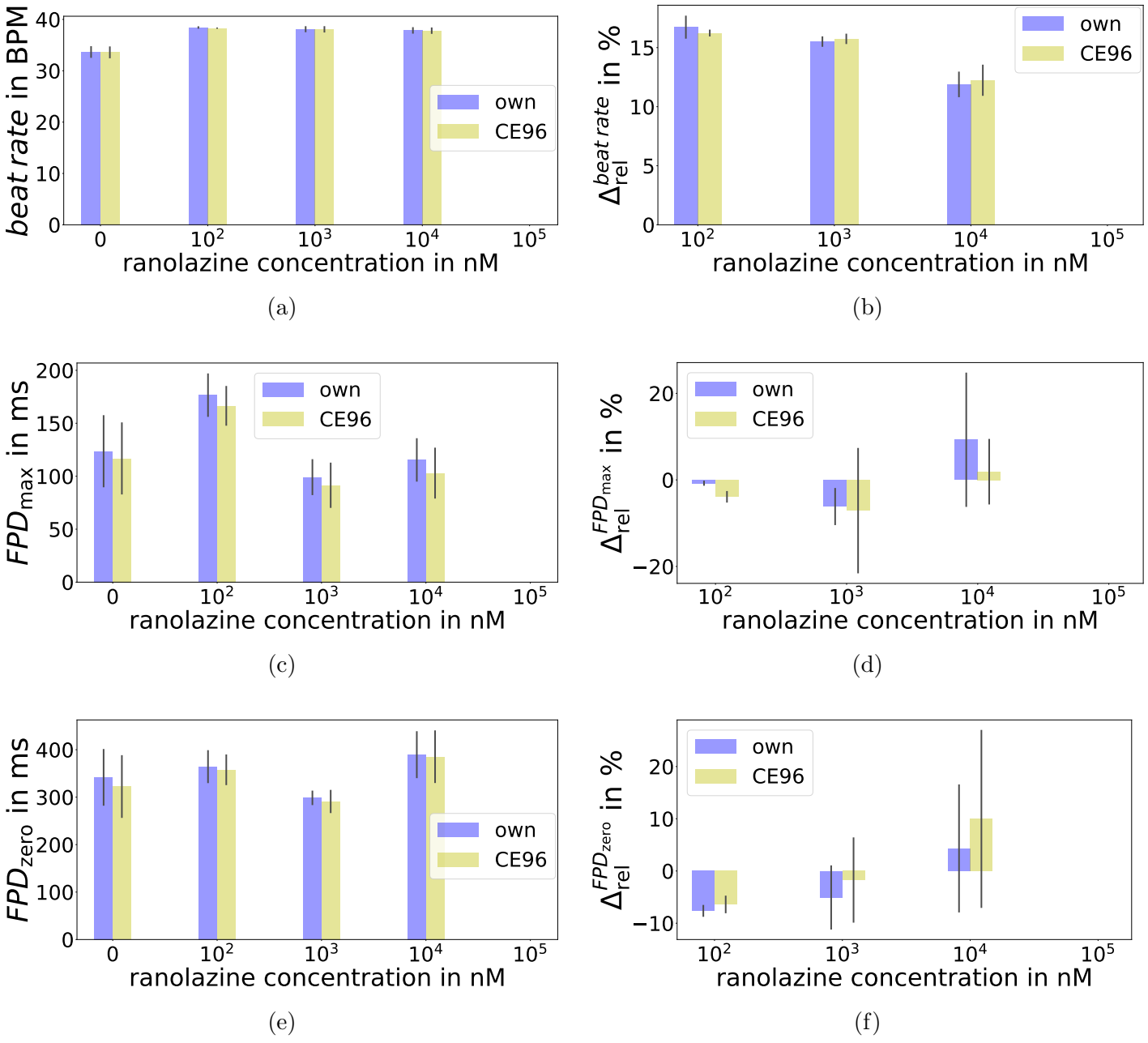
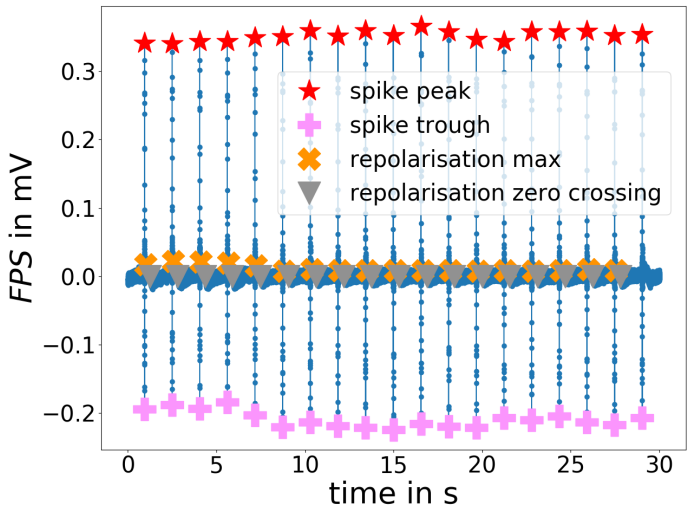
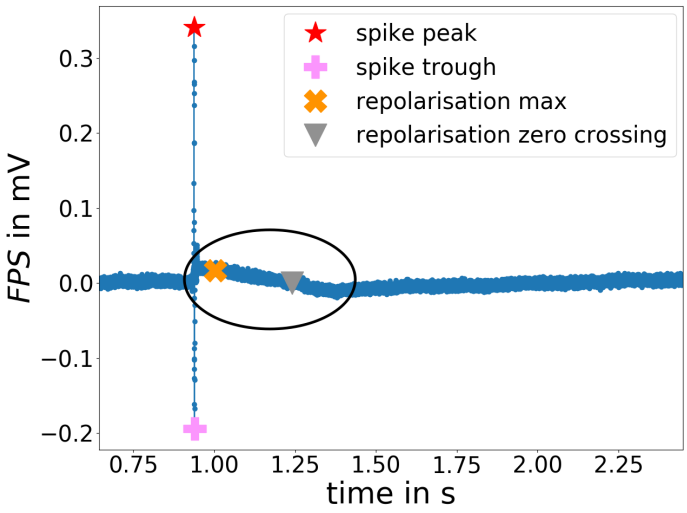


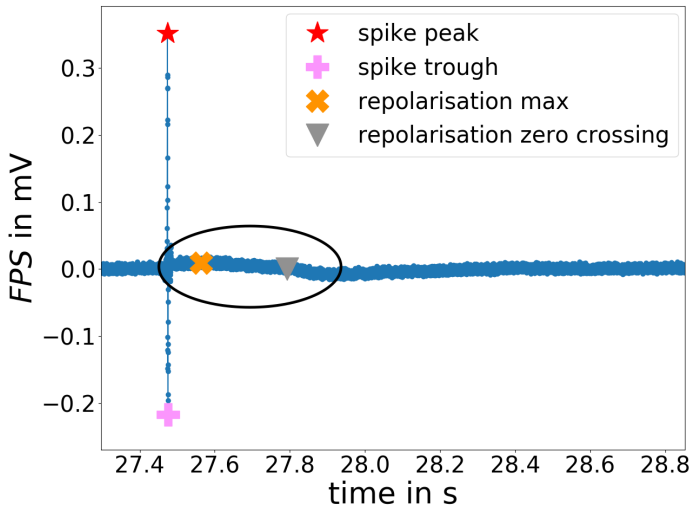
Figure 4.8: Verification of the algorithm developed in this thesis to compute FPS biomarkers by comparison with values obtained from a commercial software. The FPS biomarkers computed with our own algorithm are labeled "own" while the FPS biomarkers computed with the CardioExcyte Control 96 software are labeled "CE96". Figures (a), (c) and (e) show a comparison in values whereas Figures (b), (d) and (f) show a comparison in relative changes, as defined in the main text. Experimental wells E11, G10 and H7 were excluded from the detection because the experimental traces were unreliable (large inter-beat variation in the control or drug case). Experimental well E7 was excluded because of erroneous detection of depolarisation wave spikes by CardioExcyte Control 96. The error bars correspond to the addition and the subtraction of one standard deviation from the presented mean values.



(a)



(b)



(c)

Figure 4.9: Experimental traces from well F10 obtained after the addition of ranolazine at concentration 1000 nM. Figure (a) shows the full experimental trace. We can observe that the first five beats have a different morphology from the rest. The first beat is magnified in Figure (b) and the last beat is magnified in Figure (c). These magnifications allow for observing the differing shape of the repolarisation wave (circled). Figure (b) shows a steeper, decreasing repolarisation wave, while Figure (c) shows a flatter repolarisation wave.

4.4.2 Action potential signal processing

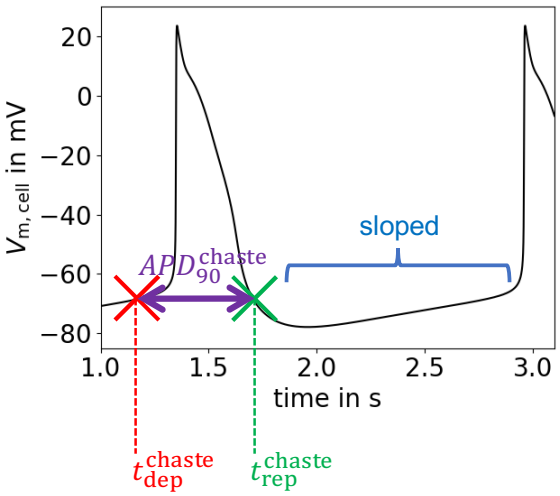
The action potential signal or cellular transmembrane potential, $V_{\text{m,cell}}$, is the dependent output of the single-cell model. A summary statistic of $V_{\text{m,cell}}$ is the duration of its action potentials. The definition of the duration of an action potential for hiPSC-CMs is challenging as $V_{\text{m,cell}}$ is devoid of a flat resting potential between two action potentials. The definition of an action potential duration given by Chaste [90] is ill-suited for such kinds of action potentials. We illustrate the inaccurate calculation of action potential duration by Chaste in Figure 4.10a. Instead of using Chaste for determining action potential duration, we decide to determine the action potential duration through a more appropriate method, which we call the *hiPSC-CM method*.

An action potential starts when the cellular transmembrane potential depolarises (the *upstroke*), and ends when it repolarises. Let i denote the index of the ith action potential. The time when it depolarises, $t_{\text{dep},i}$, approximately coincides with the time when $V_{\text{m,cell}}$ reaches its point of steepest ascent, or equivalently the maximum of its first derivative, so that for practical purposes in the hiPSC-CM method we can define $t_{\text{dep},i}$ as

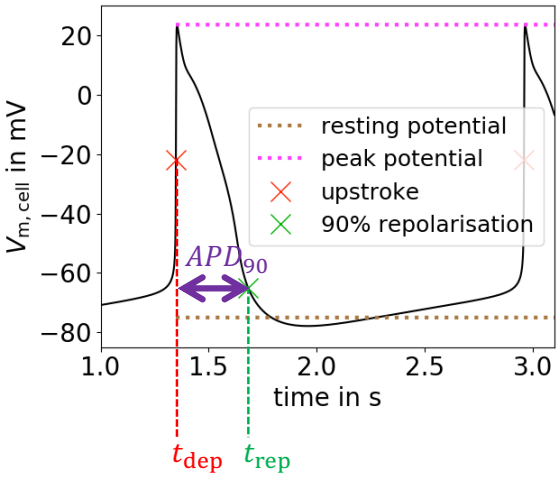
$$t_{\text{dep},i} = \underset{t\in[t_{\text{start},i},t_{\text{end},i}]}{\operatorname{argmax}} \left(\frac{\mathrm{d}V_{\text{m,cell}}}{\mathrm{d}t}\right), \tag{4.12}$$

where $[t_{\text{start},i}, t_{\text{end},i}]$ is the inverval of times between which we look for $t_{\text{dep},i}$. The method for determining this interval is given in Section A.2.1. The depolarisation time computed by the hiPSC-CM method, $t_{\text{dep},i}$, is visually defined in Figure 4.10b whereas the depolarisation time computed by Chaste, $t^{\text{chaste}}_{\text{dep},i}$ is visually defined in Figure 4.10a. The definition of t_{dep} coincides with the definition stated in [91] and [25], but differs from the definition of $t^{\text{chaste}}_{\text{dep},i}$ (see Section A.2.3 for the definition used by Chaste). Similarly, the ith repolarisation time used in the hiPSC-CM method, $t_{\text{rep},i}$, is provided a visual definition in Figure 4.10b, while the ith repolarisation time as calculated by Chaste, $t^{\text{chaste}}_{\text{rep},i}$, is provided a visual definition in Figure 4.10a. The

method for computing $t_{\text{rep},i}$ is given in Section A.2.2 and the method for computing $t_{\text{rep},i}^{\text{chaste}}$ is given in Section A.2.3.



(a)



(b)

Figure 4.10: Comparison of the definition of the action potential duration by Chaste and by the hiPSC-CM method we introduce. Figure (a) presents the automated detection of action potential features with the method used by Chaste. This method is better suited for action potential signals that have a flat resting potential. For those that do not, including those of hiPSC-CMs, Chaste overpredicts the action potential duration (see Section A.2.3 for a detailed argument). Figure (b) presents the automated detection of action potential features with the hiPSC-CM method utilised in the remainder of this work. The resting potential and peak potential variables are formally defined in Section A.2.2 while other variables are defined in the main text. In both figures, we have removed the subscript denoting the number of the action potential, i, for tidiness. The specific values of the cellular transmembrane potential shown in the figures come from the simulation of a VL hiPSC-CM cell with the Paci2013 model in the absence of drugs.

We have now provided a definition for computing the start, $t_{\text{dep},i}$, and the end, $t_{\text{rep},i}$, of the ith action potential in the hiPSC method, and have contrasted these definitions with the standard provided by Chaste. In the hiPSC-CM method, the ith action potential duration at 90% repolarisation, $APD_{90}|_i$, is defined as

$$APD_{90}|_i = t_{\text{rep},i} - t_{\text{dep},i}, \tag{4.13}$$

as illustrated in Figure 4.10b. This definition also holds for the ith action potential duration at 90% repolarisation calculated by Chaste, $APD_{90}^{\text{chaste}}\big|_i$, by replacing $t_{\text{rep},i}$ with $t_{\text{rep},i}^{\text{chaste}}$ and $t_{\text{dep},i}$ with $t_{\text{dep},i}^{\text{chaste}}$. The calculation of $APD_{90}^{\text{chaste}}\big|_i$ is illustrated in Figure 4.10a.

To test whether the algorithm we developed for computing APD_{90} is accurate, we compare the computed values to the action potential durations detected by the well-established Chaste method, APD_{90}^{chaste}. To assess whether our method is robust to the perturbations caused by the addition of drugs on hiPSC-CMs, we simulate the addition of a drug to the cellular models. The drug that we choose, called ranolazine, strongly perturbs the cellular models by blocking multiple ion channels and is one of the 12 drugs that were added to hECTs in the experiments described in Section 4.1. Additional experiments were conducted by Roche to determine the drug block parameters of ranolazine. The experiments followed the CiPA protocol [92] and determined the principal conductance-block parameters $[IC_{50}]_{chan}$ and n_{chan} of ranolazine so that its effect on ion channel conductance can be modelled using Equation (3.7). The conductance-block parameters are presented in Table 4.2.[1]

We compare the two methods by considering the difference between their outputs

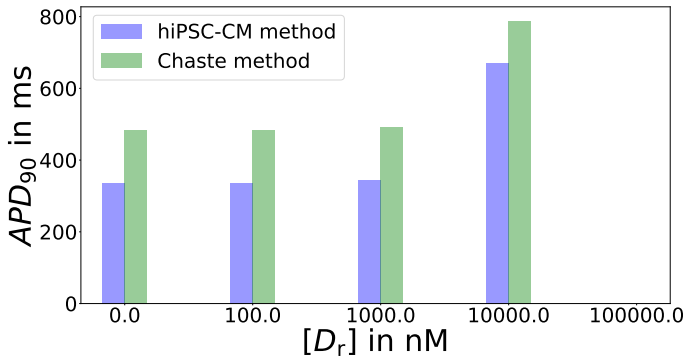
[1]The conductance-block parameters however do not fully represent the effects of ranolazine. Experimentally, ranolazine also has a blocking effect on the late-sodium ion channel which we have not included in the mathematical model of drug effects. This being said, only *in silico* data are used here for computing APD_{90} and APD_{90}^{chaste}. The differences between the experimental and theoretical effects of ranolazine are of minor importance for the present comparison between APD_{90} and APD_{90}^{chaste}.

	$[IC_{50}]_{\mathrm{Kr}}$	n_{Kr}	$[IC_{50}]_{\mathrm{Na}}$	n_{Na}	$[IC_{50}]_{\mathrm{CaL}}$	n_{CaL}
Ranolazine	9,000	1.20	34,000	1.49	179,000	1.00

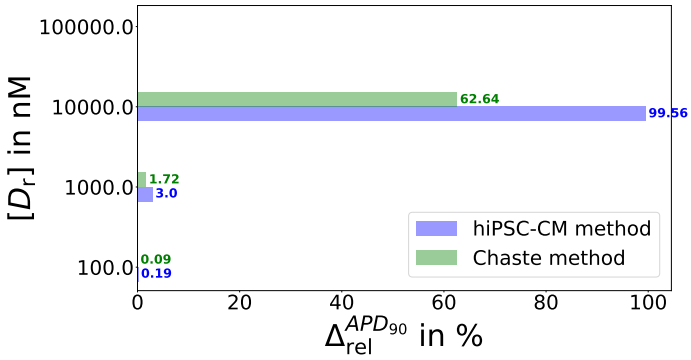
Table 4.2: Conductance-block parameters of ranolazine obtained with the CiPA protocol [92]. The subscript Kr corresponds to the rapid delayed rectifier ion channel (also referred to as *hERG*), Na to the fast sodium channel, CaL to the L-type calcium channel. The $[IC_{50}]$ values are given in nM.

with respect to two different metrics. The first metric is the simplest and consists in comparing the different values of APD_{90} produced by the two methods for all the different concentrations of ranolazine. The second metric consists in comparing the relative change in APD_{90}, $\Delta_{\mathrm{rel}}^{APD_{90}}$, between the control action potential duration produced by a hiPSC-CM under control conditions, $APD_{90}^{\mathrm{control}}$, and that produced by a hiPSC-CM exposed to ranolazine at concentration $[D_{\mathrm{r}}]$, $APD_{90}^{[D_{\mathrm{r}}]}$. The benefit of this second metric is that it only accounts for the variation in APD_{90} caused by ranolazine.

As expected from our calculations in Section A.2.3 and our discussion in Section A.2.3, the Chaste method predicts higher APD_{90} than the hiPSC-CM method for all drug concentrations, as shown in Figure 4.11a. This observation is a consequence of the Chaste method APD_{90} overprediction illustrated in Figure 4.10. The two methods produce similar results for the relative change in APD_{90}, $\Delta_{\mathrm{rel}}^{APD_{90}}$, except for $[D_{\mathrm{r}}] = 10\,000\,\mathrm{nM}$. This can be observed in Figure 4.11b. The discrepancy in $\Delta_{\mathrm{rel}}^{APD_{90}}$ for $[D_{\mathrm{r}}] = 10\,000\,\mathrm{nM}$ points to another deficiency of the Chaste method for hiPSC-CM action potential analysis. The APD_{90} value computed by Chaste is dependent on the resting potential slope. The discrepancy at $[D_{\mathrm{r}}] = 10\,000\,\mathrm{nM}$ between the hiPSC-CM method and the Chaste method is caused by the varying resting potential slope between the control and the 10 000 nM case. Precisely, a steeper resting potential slope before the depolarisation in the 10 000 nM case shortens the APD_{90} computed by Chaste, as compared to the control case. By contrast, the hiPSC-CM method is not affected by changes in the slope of the resting potential before depo-



(a)



(b)

Figure 4.11: Comparison between the calculations of APD_{90} with the hiPSC-CM method and the Chaste method: (a) shows a comparison in absolute values whereas (b) shows a comparison in relative changes, as defined in the main text. The single-cell model used in these simulations is the Paci2013 model simulating a VL hiPSC-CM. The conductance-block model is parametrised by the parameters given in Table 4.2. No beat was observed at the largest concentration tested.

larisation. This is good behaviour for computing APD_{90}, as the action potential only starts at depolarisation. In conclusion, the hiPSC-CM method is more accurate than the Chaste method for determining the APD_{90} and $\Delta_{\text{rel}}^{APD_{90}}$ of hiPSC-CM.

4.4.3 Implementation

The Julia [93] code we have written for the signal processing is scalable to the analysis of multiple drug-perturbed or control datasets. We wrote it following an object-oriented and functional paradigm for clarity, reusability and extendibility. A challenge

for the implementation was to write code that could execute sufficiently fast to process in a reasonable amount of time the data files output by the simulation, which can be as large as ~ 15 gigabytes. That challenge was met as the program processes the simulated output in about three minutes when the files are read from a solid-state drive (SSD).

4.5 Uncertainty quantification of simulations

The simulation of the bidomain model is very computationally intensive. However, the effect of drugs on summary statistics can be subtle. We followed multiple strategies to reduce computational time while maintaining the error introduced sufficiently small to capture subtle changes due to drugs. Three strategies proved to be instrumental. First, we reduced the resolution of the simulations (see Section 4.5.1). Second, we used an adaptive timestep and tolerance method (Section 4.5.2). Finally, we approximated the steady state of the summary statistics (Section 4.5.3).

In this thesis, we always initialise the tissue simulations with the attracting values of the cell model variables. We deem that these attracting values are reached when the difference between the last two action potential durations of $V_{\mathrm{m,cell}}$ is sufficiently small. Formally, we simulate the cell model until we have

$$\left| APD_{90}^{\mathrm{chaste}}\big|_{N} - APD_{90}^{\mathrm{chaste}}\big|_{N-1} \right| \leq 0.02\,\mathrm{ms}, \tag{4.14}$$

where $APD_{90}^{\mathrm{chaste}}$ is computed on $V_{\mathrm{m,cell}}$, and N is the number of action potential durations detected in $V_{\mathrm{m,cell}}$.[2] We chose the tolerance in Equation (4.14) (0.02 ms) so that it was less than 0.01% of a typical $APD_{90}^{\mathrm{chaste}}$ value (see Figure 4.11a).

[2]For practical purposes, we used $APD_{90}^{\mathrm{chaste}}$ instead of APD_{90} to define when the attracting values of the cell model variables are reached. We established in Figure 4.11 that $APD_{90}^{\mathrm{chaste}}$ captures the action potential duration of hiPSC-CM worse than APD_{90}. However, $APD_{90}^{\mathrm{chaste}}$ is still a well-established biomarker of $V_{\mathrm{m,cell}}$ [94]. In addition, it appears to be correlated to APD_{90} (see

4.5.1 Spatial resolution

We utilised the square domain introduced in Section 4.3.2 to estimate the effect of varying the spatial and temporal resolution on the summary statistics. We used the phenotype distribution presented in Figure 4.4. We present the error introduced by a coarse mesh (750 µm) and fine timestep (0.1 ms), relative to an intricate 25 µm mesh and 0.004 ms timestep, in Table 4.3. We discovered that the coarse mesh, surprisingly, introduces a less than 3 % error as compared to the very fine 25 µm mesh. We deem that errors smaller than 5 % are acceptable to capture the effect of drugs on hECT (for order-of-magnitude estimates of changes expected to be caused by drugs, see [95]). The computational time gain enabled by accepting such error is vast. For reference, we conducted 6 s simulations on the original domain to study the influence of spatial resolution on computational expense. We compared the computational expense incurred between a 750 µm mesh and a 50 µm mesh. The 15× coarser 750 µm mesh took 50× less time to compute, with 5× less computational cores. The full results of the comparison are presented in Section A.3. The 750 µm mesh is illustrated in Figure 4.3.

$h, \Delta t$	FPD_{zero}	FPD_{max}	APD_{90}	*beat rate*
750 µm, 0.1 ms	-2.97%	+0.11%	-0.29%	-0.80%

Table 4.3: Relative error induced by the choice of spatial resolution, h, and temporal resolution, Δt. The relative error was computed on the second beat, on the square mesh, at spatial point (0.24, 0.24) cm (close to the centre). The reference is the second beat of the 25 µm, 0.004 ms simulation. We chose to perform the comparison on the second beat so as to enable the very expensive computation of the reference solution.

Figure 4.11a). For these reasons, we assume that APD_{90}^{chaste} can be used as an indicator of the time when the attracting values of the cell model variables have been reached.

4.5.2 Adaptive timestep and tolerance

To reduce the computation time further we implemented a simple adaptive timestep and tolerance scheme. We simulate at a coarse timestep and tolerance for the first part of the simulation, until we reach the time when summary statistics should be extracted. At this time we decrease the timestep and tolerance to accurately capture the system dynamics.[3]

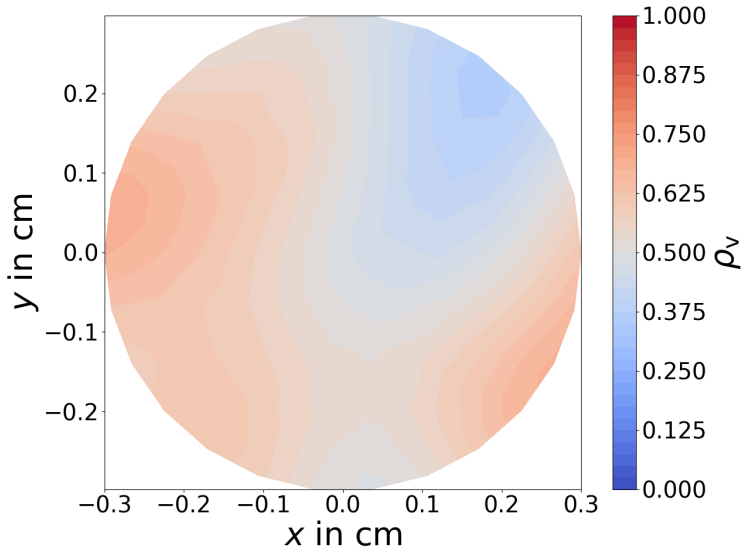


Figure 4.12: Visualisation of the distribution of VL hiPSC-CMs in the tissue obtained from a realisation of the Gaussian random field specified by equation (3.17). Overall, there are 54% VL hiPSC-CMs and 46% AL hiPSC-CMs in this figure. The Gaussian random field used to produce this visualisation was parametrised by the unitless variables $\mu = 0.54$ and $\sigma = 0.075$, and $l_c = 0.2\,\text{cm}$. The x and y variables indicate coordinates in space as defined by their respective axes in the figure.

We tested the error introduced by this adaptive scheme on the summary statistics. To perform the comparison, we chose the original round domain and the phenotype realisation presented in Figure 4.12. The error introduced by the adaptive scheme is presented in Table 4.4. These errors are reasonable with regards to the computation

[3]Precisely, we simulated at a coarse timestep and tolerance until 1976 s, and refined the timestep and tolerance for the rest of the simulation (1976 s to 2006 s). The dividing boundary at 1976 s was chosen because we had originally planned to study the dynamics between 1976 s and 2006 s. However, we eventually decided to only study the dynamics between 2000 s and 2006 s. We made this change to limit computational expense in signal processing.

$\Delta t_c, tol_c$	FPD_{zero}	$FPD_{\max}$	APD_{90}	*beat rate*
1 ms, 10^{-3}	-2.25%	-3.31%	-1.05%	-0.64%

Table 4.4: Relative error incurred on summary statistics with the adaptive timestep and tolerance method. The summary statistics obtained with the adaptive and non-adaptive method were computed on the median of the *FPS* and $\overline{V_m}^{\text{rec}}$ between 2000 s and 2006 s. The reference is the non-adaptive simulation, defined by $(\Delta t_c, tol_c) = (0.1, 10^{-5})$. These statistics have been computed on the phenotype realisation given in Figure 4.12.

$\Delta t_c, tol_c$	# cores	computation time
0.1 ms, 10^{-5}	8	45 049.3 s $\approx$ 12 h31 min
1 ms, 10^{-3}	8	37 775.5 s $\approx$ 10 h30 min

Table 4.5: Comparison of computation time taken to simulate 2006 s of the bidomain model with different coarse timesteps and absolute tolerances. The non-adaptive simulation is indicated by its coarse timestep and absolute tolerance, $(\Delta t_c, tol_c) = (0.1, 10^{-5})$ The abbreviation "# cores" stands for the number of processor cores involved in the simulation. The simulations presented here were conducted on the 750 µm mesh.

savings they allow us to achieve. We save 16% computation time by using this method, as presented in Table 4.5.

4.5.3 Approximation of the steady state of the summary statistics

Experimental measurements are assumed to have been conducted at the steady-state of the summary statistics. We want to reproduce the experimental measurements by extracting simulated summary statistics at steady state. In Figure 4.13 we present the time evolution of summary statistics over about 2 h45 min. This evolution is representative of the drug-free, control case. We present the time evolution of summary statistics for the case of nifedipine in Section A.4.2. To strike a compromise between minimising computation time and steady-state approximation error, we chose to study statistics between 2000 s and 2006 s (about 33 min). The relative error introduced by this choice is presented in Table 4.6. We observe that little error is introduced by

this approximation. This approximation is much more precise than the use of the first beats to approximate steady-state, as presented in Table 4.7. In particular, our approximation is much closer than the first-beat approximations for the simulations where nifedipine is added.

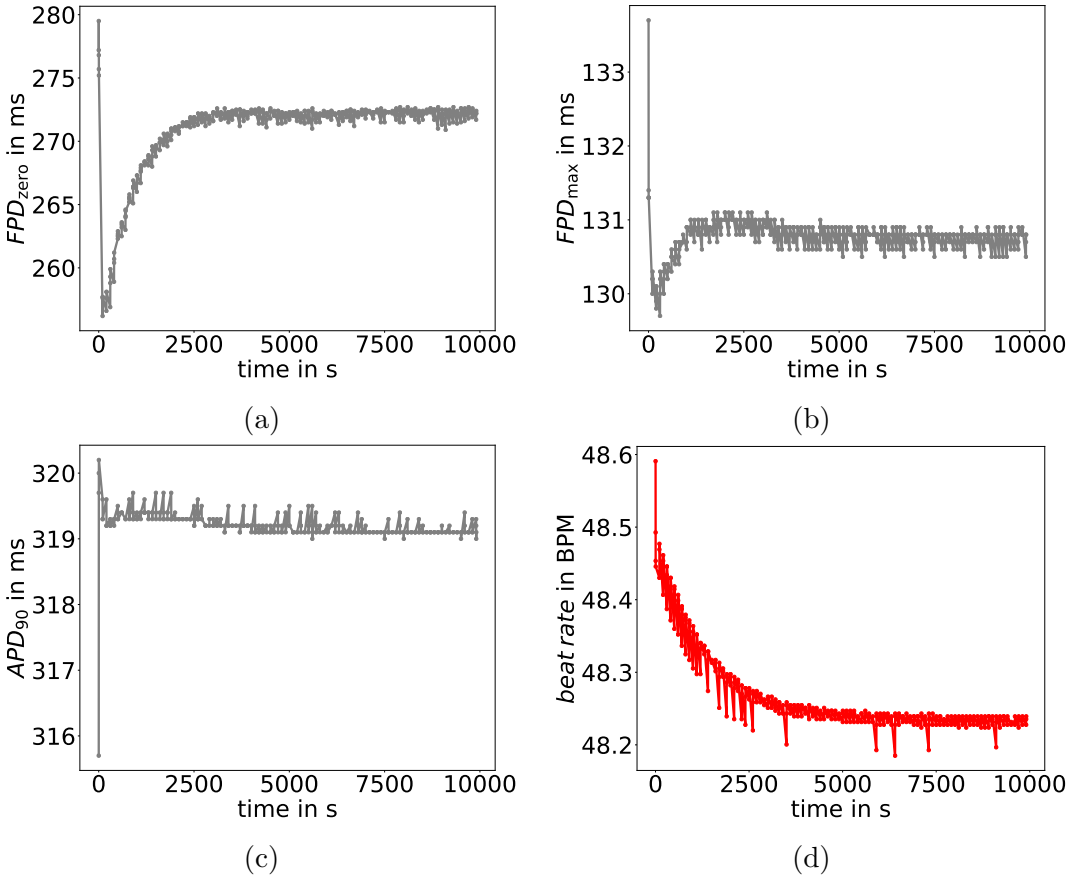


Figure 4.13: Time evolution of four summary statistics. The summary statistics were obtained from a control simulation (no drug). The summary statistics were extracted from the output of a simulation with varying printing timestep. Every 100 s, only 6 s of simulation were printed to file. This allowed us to keep the size of the output file manageable (15 GB). Outlying data points due to faulty detection were removed following the procedure detailed in Section A.4.1. The phenotype realisation chosen is illustrated in Figure 4.12.

drug, concentration	FPD_{zero}	FPD_{max}	APD_{90}	*beat rate*
control	-0.42%	0.23%	0.05%	0.12%
nifedipine, 100 nM	-0.11%	-0.60%	-0.48%	0.10%
nifedipine, 1000 nM	-0.40%	-0.16%	0.02%	0.00%

Table 4.6: Relative error introduced by the approximation of the steady-state of summary statistics used in this thesis. The value chosen was obtained on the median of the summary statistics between 2.000 s and 2.006 s. The reference is the steady-state values approximated by the median of the summary statistics between 9.900 s and 9.906 s. The summary statistic values were obtained after the application of the outlier filter described in Section A.4.1.

drug, concentration	FPD_{zero}	FPD_{max}	APD_{90}	*beat rate*
control	1.69%	0.42%	0.22%	0.49%
nifedipine, 100 nM	-5.91%	-6.66%	-5.86%	1.15%
nifedipine, 1000 nM	4.84%	-6.39%	-5.09%	1.37%

Table 4.7: Relative error introduced by the approximation of the steady-state of summary statistics with the first beats of the simulation. This approximation is not used in this thesis and is presented here for reference only. The value chosen was obtained on the median of the summary statistics between 0 s and 6 s. The reference is the steady-state values approximated by the median of the summary statistics between 9.900 s and 9.906 s. The summary statistic values were obtained after the application of the outlier filter described in Section A.4.1.

4.6 Discussion

In order to keep the computation cost manageable (about 10 h on 8 cores for one simulation), we have accepted to incur the error that is summarised in Section 4.5. This error prevents us from examining the effects of low doses of drugs as the slight effects of drugs on summary statistics at low doses [96] would not be distinguishable from the error introduced by our approximations.

It could be argued that we have been too conservative in the selection of the time-point for approximating the steady state. Indeed, the errors presented in Table 4.6 are much smaller than those due to the resolution choices. Having said this, we observed in Table 4.7 that the reliability of earlier approximations is drug-dependent. We chose a close approximation for the steady-state of the tested drug to provide a safety margin. This safety margin guards us against inaccurate predictions for potential drugs that would take longer to reach steady-state.

Chapter 5

In silico-in vitro investigation of the electrophysiological response of engineered cardiac tissue to drugs

In this chapter, we present investigate the electrophysiological response of engineered cardiac tissue to drugs. First, we provide mechanistic insight into the shape of the waveform of the experimentally measured FPS, through an *in silico* study (Section 5.1). Then, we determine the limitations of the model and summary statistics we have chosen for our study (Section 5.2). We investigate the effect of phenotype variation on the action potential duration in Section 5.3. Section 5.4 contains a comprehensive investigation of the impact of twelve drugs on various repolarisation time biomarkers. Finally, Section 5.5 provides a discussion of the results presented in this chapter.

5.1 Insight into the dynamics of the measured field potential signal

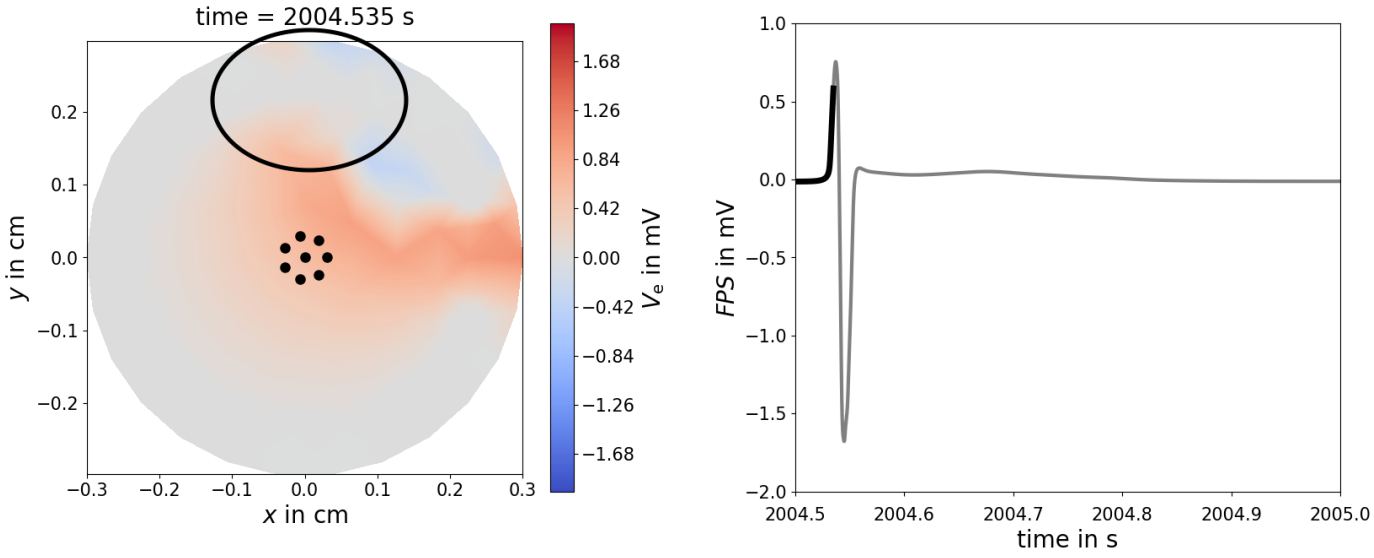
A lack of mechanistic insight into the role of the underlying ionic, cellular and tissue level factors influencing FPS morphology has challenged the use of this signal to study cardiac electrophysiology [97]. Tissue-scale simulations allow us to study the mechanism by which the FPS emerges from the values of V_e in the tissue. In addition, insights on the underlying factors that produce the FPS can be obtained from comparison with the action potential signal, $\overline{V_\mathrm{m}}^{\mathrm{rec}}$. The action potential signal is defined similarly to the FPS as the average of V_m over the recording electrode. Formally,

$$\overline{V_\mathrm{m}}^{\mathrm{rec}}\big|_n = \frac{1}{|\mathbf{rec}|}\sum_{l\in\mathbf{rec}} V_\mathrm{m}|_{n,l}, \tag{5.1}$$

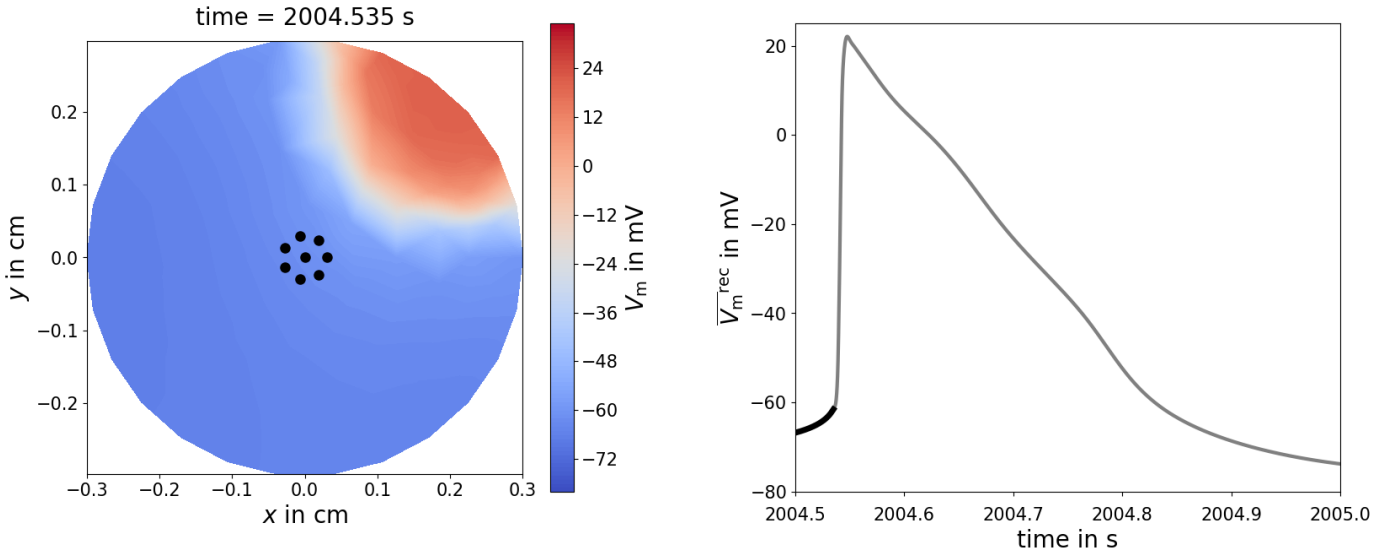
where $V_\mathrm{m}|_{n,l}$ is the transmembrane potential evaluated at timestep n and linear spatial index l, and **rec** and $|\mathbf{rec}|$ are as defined in Equation (4.10). Although the study of the FPS is in its infancy, the ionic, cellular and tissue factors underlying the action potential signal have been the subject of numerous studies [37]. We will use the action potential signal as a reference to understand the underlying factors of the FPS.

We will also use the comparison between FPS and $\overline{V_\mathrm{m}}^{\mathrm{rec}}$ to estimate the similarity between the time-to-repolarisation measurements in the two signals. The time to repolarisation is defined as the duration between the depolarisation and the repolarisation in a given cardiac beat. As mentioned in Section 2.2, the time to repolarisation is important in the context of drug safety testing. A significant increase in time to repolarisation after the addition of a drug may suggest that the drug is arrhythmogenic. The general definition of time to repolarisation has to made specific to measure the time to repolarisation from a given signal. The action potential signal summary statistic APD_{90} is the gold standard for measuring the time to repolarisation [97]. The FPS summary statistics FPD_{max} and FPD_{zero} are candidates for measuring time

to repolarisation on the FPS. We collectively refer to $FPD_{\max}$, FPD_{zero} and APD_{90} as *time-to-repolarisation biomarkers*. The action potential duration at 90% repolarisation measures a duration that starts at the $\overline{V_{\text{m}}}^{\text{rec}}$ upstroke, while $FPD_{\max}$ and FPD_{zero} measure a duration that starts at the FPS spike trough. Here, we will determine whether the time of the FPS depolarisation spike trough corresponds to that of the $\overline{V_{\text{m}}}^{\text{rec}}$ depolarisation. If it does, the validity of the start time for the $FPD_{\max}$ and the FPD_{zero} measurements will be established.



(a)



(b)

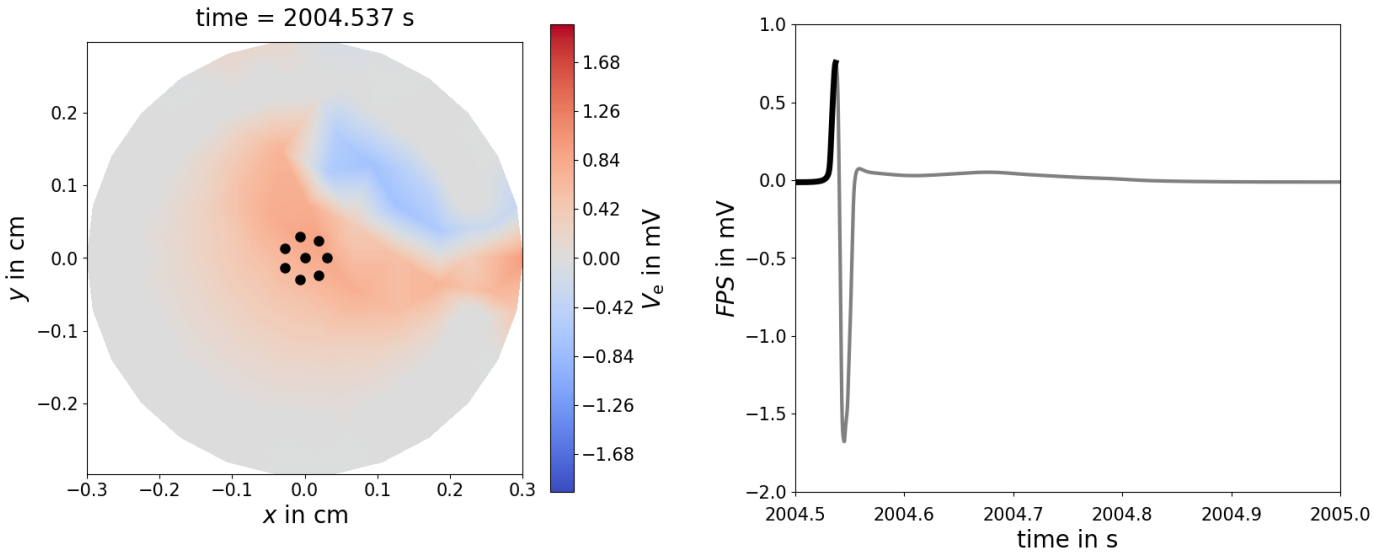
Figure 5.1: Stills of V_e and V_m in the domain Ω, and the FPS and $\overline{V_m}^{rec}$ values, before the depolarisation wave reaches the recording electrode. The bold black lines in the FPS and $\overline{V_m}^{rec}$ represent the values prior to the time at which V_e and V_m are displayed. The black dots represent the mesh nodes located within the recording electrode. The black circle highlights the broken V_e depolarisation wave that is caused by the grounded reference electrode. Figure (a) presents V_e (left) and the FPS (right), and Figure (b) presents V_m (left) and $\overline{V_m}^{rec}$ (right). The phenotype distribution used for the simulation is shown in Figure 4.12.

We study the formation of the depolarisation wave in a control simulation after about 33 min of simulation (see Section 4.5.3 for an explanation of the simulation time choice). Figure 5.1 presents the values of V_e and V_m throughout the tissue before the depolarisation wave reaches the recording electrode. We notice that the depolarisation wave is initiated in the region of the tissue containing the most AL phenotypes, that is, where ρ_v is minimal (see Figure 4.12 for the phenotype realisation used). This is expected as AL CMs have a higher beat rate than VL CMs [20]. The region with the most AL cells is always expected to pace the tissue.

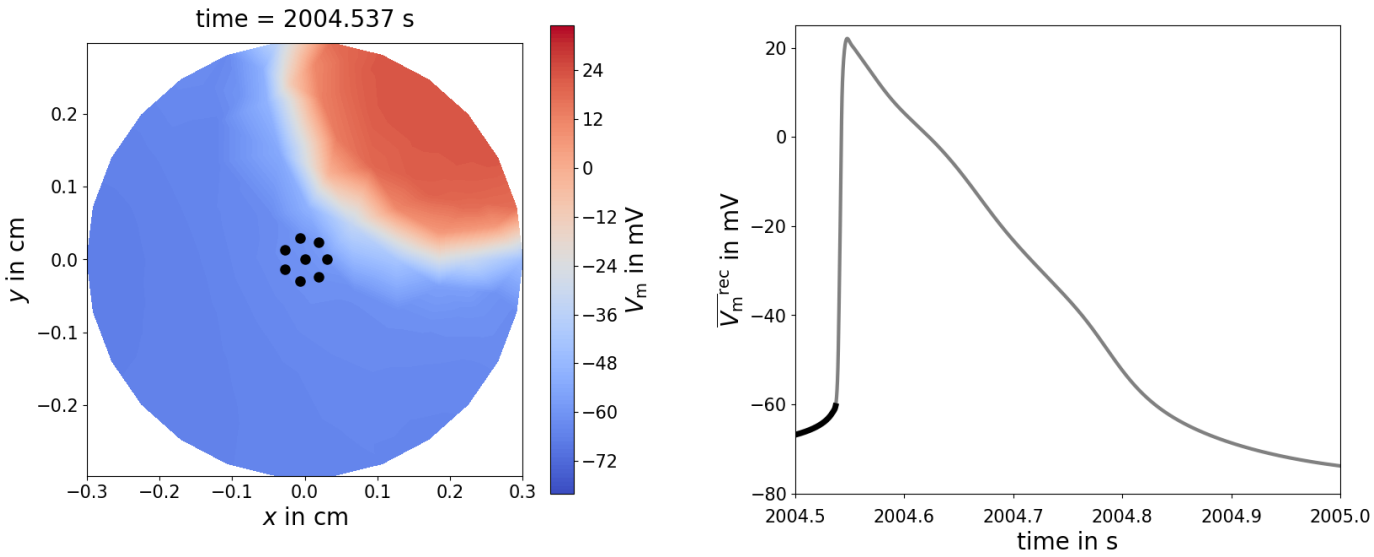
We observe that the depolarisation wave front in V_e is broken (i.e. $V_e = 0$) in the region of the reference electrode. In Figure 5.1a, we have circled the portion of the reference electrode where this phenomenon is most obvious. This phenomenon suggests that the grounding electrode is correctly simulated as V_e is expected to be null over the reference electrode (see Equation (4.2)). In Figure 5.1b, the V_m depolarisation wave progresses in a manner consistent with the system presented in Equation (4.3) and Equation (4.4).

We notice that the V_m depolarisation wave is preceded by positive values for V_e. This phenomenon appears to be due to current originating from neighbouring cells [98]. At the time presented in Figure 5.1, the FPS has risen because the positive portion of the V_e wave has reached the recording electrode. At this time, the upstroke in V_m has not yet reached the recording electrode. However, a slight elevation in $\overline{V_m}^{rec}$ can be observed.

Figure 4.12 presents the state of the tissue only 2 ms after Figure 5.1. This time corresponds to the peak of the spike in FPS. At that time, the action potential upstroke has not yet occurred. This suggests that the peak of the FPS spike does not correspond to the upstroke in $\overline{V_m}^{rec}$.

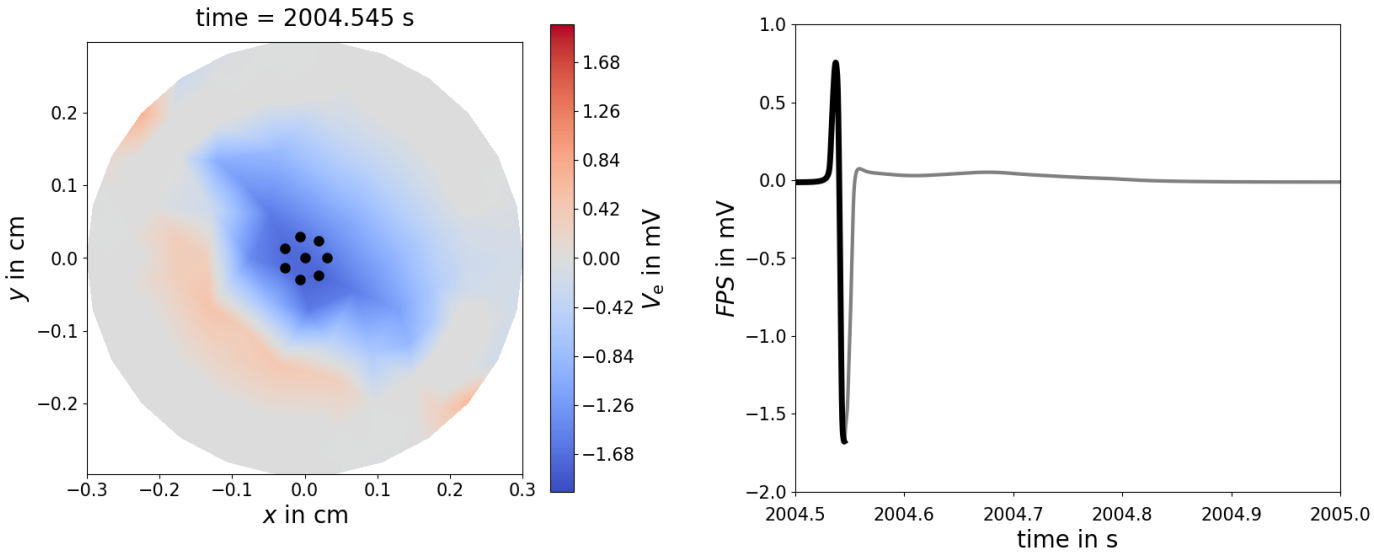


(a)

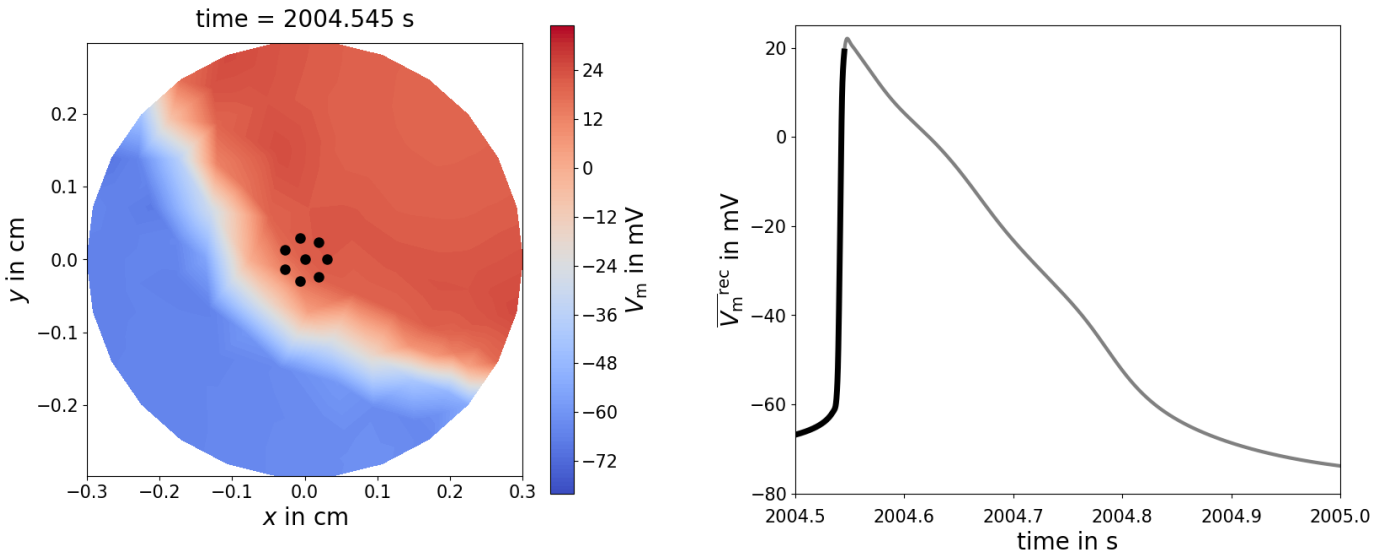


(b)

Figure 5.2: Stills of V_e and V_m in the domain Ω, and the FPS and $\overline{V_m}^{rec}$ values, when the *FPS* is at the spike peak. The black dots represent the mesh nodes located within the recording electrode. Figure (a) presents V_e (left) and the *FPS* (right), and Figure (b) presents V_m (left) and $\overline{V_m}^{rec}$ (right). The phenotype used for the simulation is shown in Figure 4.12.



(a)



(b)

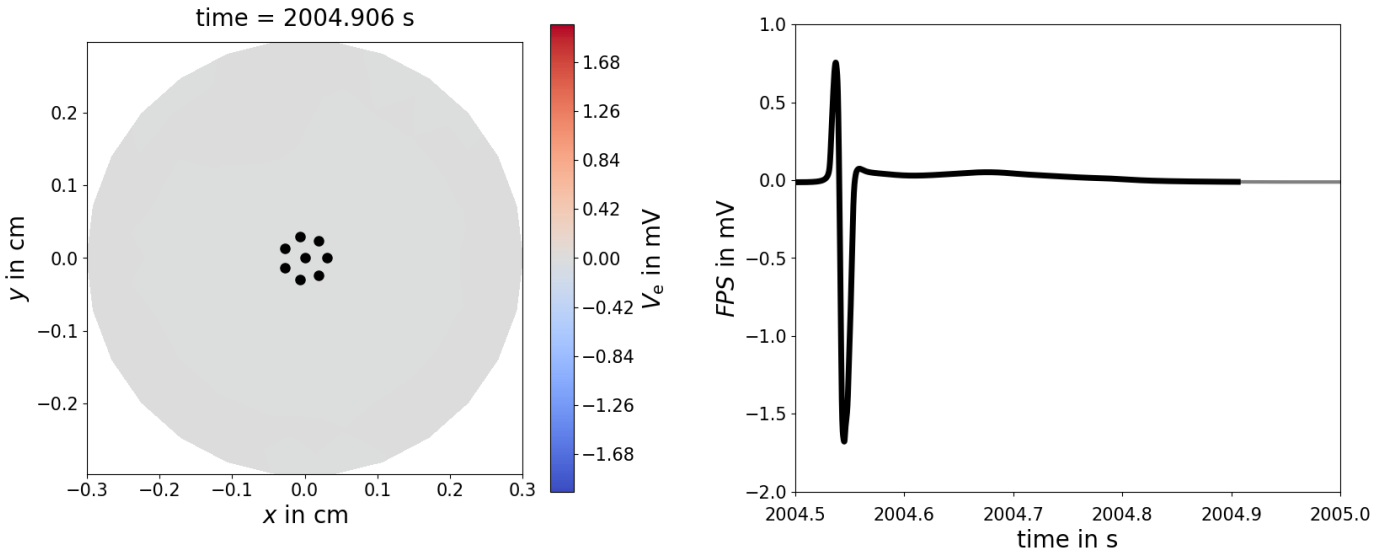
Figure 5.3: Stills of V_e and V_m in the domain Ω, and the FPS and $\overline{V_m}^{rec}$ values, when the *FPS* is at the spike trough. The black dots represent the mesh nodes located within the recording electrode. Figure (a) presents V_e (left) and the *FPS* (right), and Figure (b) presents V_m (left) and $\overline{V_m}^{rec}$ (right). The phenotype used for the simulation is shown in Figure 4.12.

Figure 5.3 gives an overview of the state of the tissue when the FPS reaches its spike trough. We note that the depolarisation wave, characterised by positive values of V_{m}, appears as negative values for V_{e}. The explanation is that the depolarisation is caused by a rapid influx of Na^+ from the extracellular medium into the cell (see Section 2.1.1). The resulting loss of positive charge in the extracellular medium causes the trough in the FPS [99]. With the phenotype realisation, and on the domain presented here, we observe that the time of the FPS spike trough corresponds almost perfectly to the time of the $\overline{V_{\mathrm{m}}}^{\mathrm{rec}}$ upstroke. Given the mechanistic understanding detailed above (Na^+ influx), we speculate that this observation can be extrapolated to other phenotype realisations and domains.

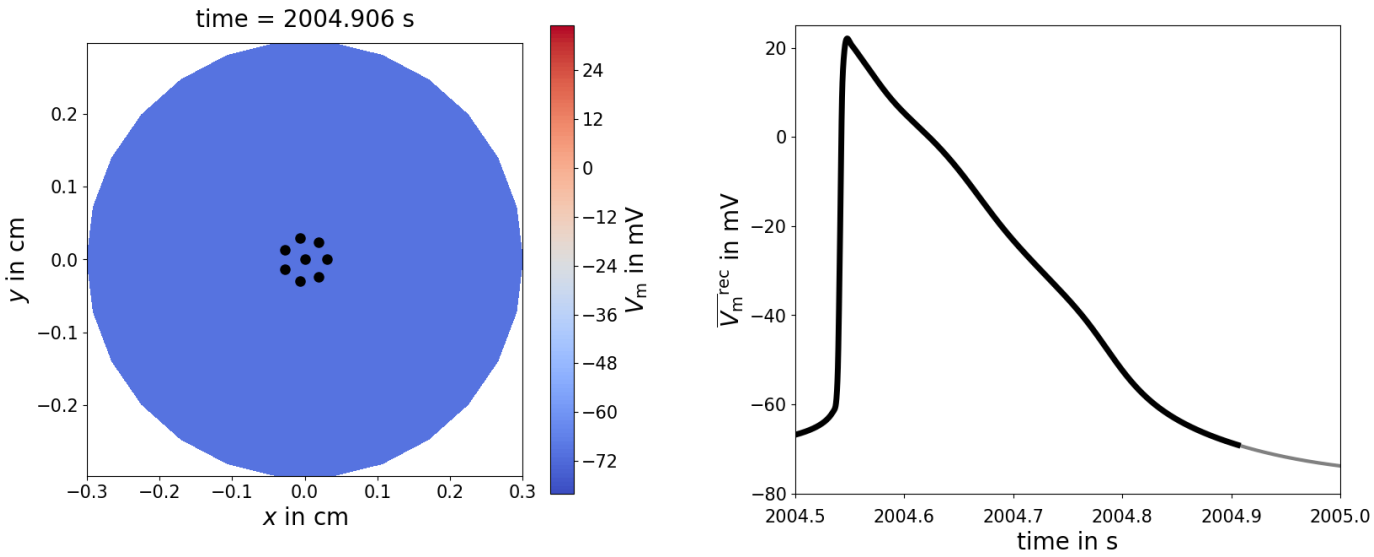
The last still presented in Figure 5.4 summarises the state of the hECT at the end of the action potential. It can be observed that the end of the action potential (loosely defined as the time when $\overline{V_{\mathrm{m}}}^{\mathrm{rec}}$ reaches about $-70\,\mathrm{mV}$) corresponds to the end of the field potential (loosely defined as a constant $0\,\mathrm{mV}$ value).

In this section, we have learnt about the pacemaking role of the most AL region in the tissue. This helps us appreciate the impact of the AL cell type on the tissue behaviour. We have confirmed that the grounding electrode is correctly implemented in the simulation. This observation strengthens our confidence in our simulation implementation. Finally, we have observed that the FPS spike trough occurs at the same time as the $\overline{V_{\mathrm{m}}}^{\mathrm{rec}}$ upstroke, in the example presented. Following the argument presented at the beginning of this section, this observation suggests that the start time for FPD_{max} and the FPD_{zero} is valid.

So far we have deliberately excluded from the analysis the repolarisation wave. Indeed, the interpretation of the different portions of the repolarisation wave is complex. The shape of the repolarisation wave in the FPS largely depends on whether a drug was administered. The following section includes a study of the repolarisation wave in control and under drug treatment.



(a)



(b)

Figure 5.4: Stills of V_e and V_m in the domain Ω, and the FPS and $\overline{V_m}^{rec}$ values, when the action potential over the recording electrode has ended. The black dots represent the mesh nodes located within the recording electrode. Figure (a) presents V_e (left) and the *FPS* (right), and Figure (b) presents V_m (left) and $\overline{V_m}^{rec}$ (right). The phenotype used for the simulation is shown in Figure 4.12.

5.2 Drug-dependent field potential duration biomarker validity

In the example presented in Section 5.1, we have shown the validity of the start time of FPD_{max} and FPD_{zero}. This result was obtained by comparison with the APD_{90} start time, the $\overline{V_{\text{m}}}^{\text{rec}}$ depolarisation upstroke. Here, we follow a similar methodology to determine the validity of the end time of FPD_{max} and the end time of FPD_{zero}. The end time of FPD_{max} is the time of the FPS repolarisation at maximum and the end time of FPD_{zero} is the time of the FPS repolarisation at zero-crossing (see Section 4.4.1). We compare these end times to the end time of APD_{90}, the time of the $\overline{V_{\text{m}}}^{\text{rec}}$ 90% repolarisation (see Section 4.4.2). This time is taken as the gold standard, as mentioned in Section 5.1. The closer the field potential duration end times are to the time of $\overline{V_{\text{m}}}^{\text{rec}}$ 90% repolarisation, the more valid they are. A difficulty in asserting the validity of field potential duration end times is their high sensitivity to the application of a drug. Here, we study the validity of field potential duration end times under varied drug conditions (including the absence of drugs). We also interrogate the time evolution of membrane ionic currents to determine which ionic current features are captured by the time-to-repolarisation biomarkers under varied drug conditions. The interpretation of the membrane ionic current variables in the model is given in Table 5.1. The drugs that we chose to study here have known mechanisms of action. These drugs are representatives of several classes of ion-channel blocking drugs. We utilise their representativity to provide insight into the validity of field potential duration end times for several classes of ion-channel blocking drugs. In addition, we identify the ionic current features captured by the time-to-repolarisation biomarkers for several classes of ion-channel blocking drugs.

variable name	**full name**
I_{Na}	fast sodium current
I_{CaL}	L-type calcium current
I_{to}	transient outward current
I_{Kr}	rapid delayed rectifier potassium current
I_{Ks}	slow delayed rectifier potassium current
I_{K1}	inward rectifier potassium current
I_{f}	funny current
I_{NaK}	sodium-potassium pump current
I_{NaCa}	sodium-calcium exchanger current
I_{pCa}	calcium pump current
I_{bCa}	background calcium current
I_{bNa}	background sodium current

Table 5.1: Interpretation for the membrane ionic current variables in the model.

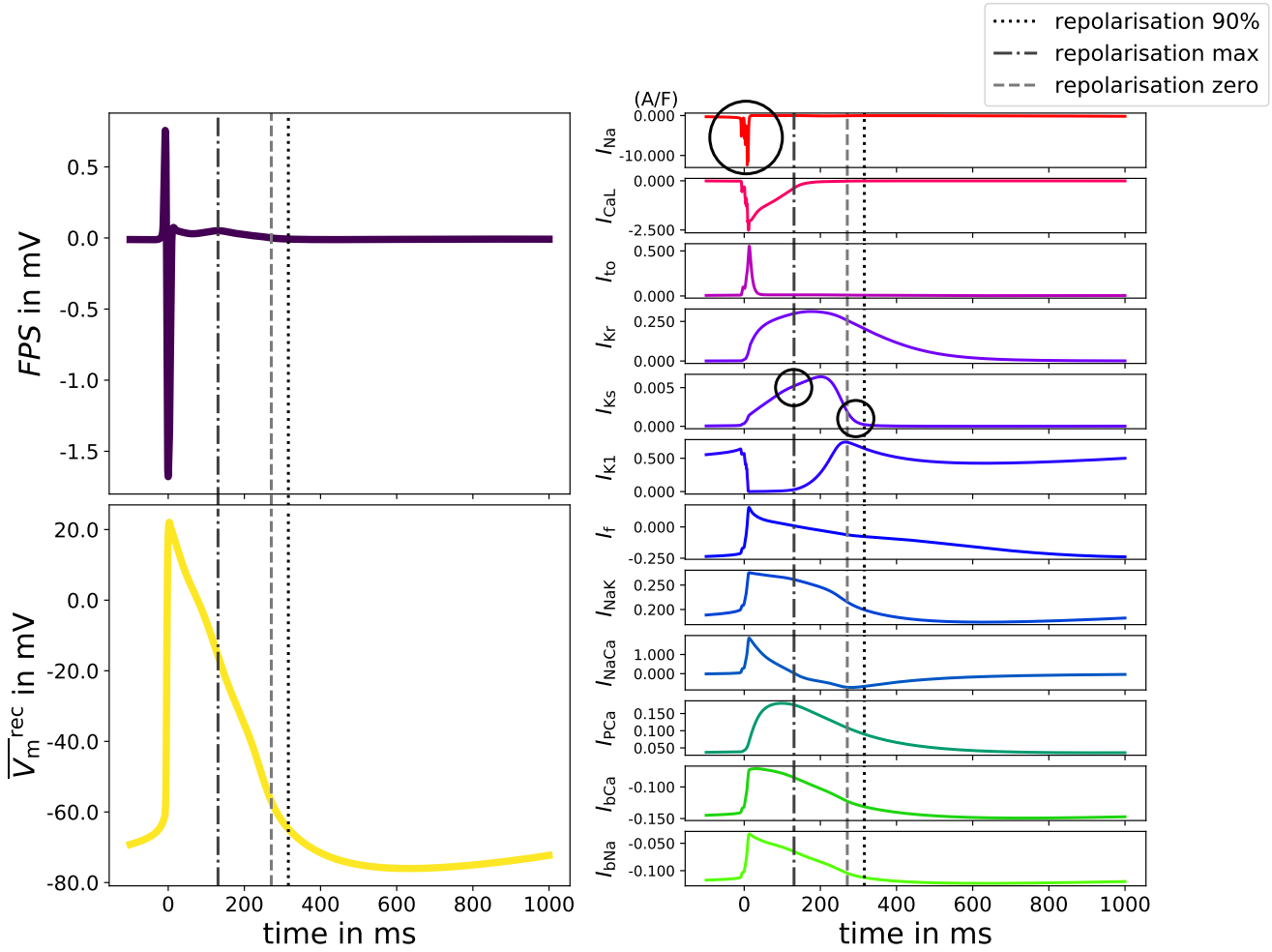


Figure 5.5: Comparison of the field potential, action potential and membrane ionic currents for the second-to-last beat before 2006 s (simulation end time). This beat was chosen as it is the last complete beat before 2006 s. The field potential is presented in the top-left corner, the action potential in the bottom-left corner, and the membrane ionic currents on the right. This simulation was performed in control conditions (no drug). Time zero corresponds to the spike trough and the different repolarisation times are shown as dashed or dotted lines. This presentation assumes that the $\overline{V_m}^{rec}$ upstroke and the FPS spike trough happen simultaneously (see Figure 5.3 for validation). This assumption allows us to compare repolarisation times across $\overline{V_m}^{rec}$ and the FPS. Different styles of grey lines are used to denote where repolarisation occurs. The different line styles were chosen to distinguish the various definitions of repolarisation we consider. We denote by "repolarisation 90%" the $\overline{V_m}^{rec}$ 90% repolarisation, as defined for the computation of the summary statistic APD_{90} (see Section 4.4.2). We denote by "repolarisation max" the FPS repolarisation at maximum, as defined for the computation of FPD_{max}; and "repolarisation zero" the FPS repolarisation at zero-crossing, as defined for the computation of FPD_{zero} (see Section 4.4.1). Important ionic current features discussed in the text are circled. The phenotype used for the simulation is shown in Figure 4.12.

In Figure 5.5 we present from various perspectives the simulated recording of a beat in control conditions. The FPS of the beat is shown, along with $\overline{V_{\mathrm{m}}}^{\mathrm{rec}}$, and all of the membrane ionic currents. The ionic currents presented are averaged over the recording electrode, as in Equation (4.10) or Equation (5.1). The slightly jerky shape of the ionic currents originates from this averaging process. We note that the I_{Na}, I_{CaL}, I_{f}, I_{to}, I_{K1}, I_{Kr}, and I_{Ks} ionic currents included in the cellular model we use [16] were individually fitted by [16] to match experimental ionic current data collected by [20]. By contrast, the I_{NaCa}, I_{NaK}, I_{pCa}, I_{bNa}, I_{bCa} currents were only optimised to match experimental $V_{m,\mathrm{cell}}$ signals [20] (see Section 3.1.3 for more detail). Therefore, the values found for the I_{NaCa}, I_{NaK}, I_{pCa}, I_{bNa}, I_{bCa} current parameters is questionable. In addition, we observe that the five currents at the bottom of Figure 5.5 (those optimised for $V_{m,\mathrm{cell}}$) have waveforms that look suspiciously like the action potential of $\overline{V_{\mathrm{m}}}^{\mathrm{rec}}$. These waveforms may be artefacts of the optimisation procedure used by [16], rather than indications of the physiology of the currents. Overall, the validity of the simulated five currents is doubtful. This conclusion calls into question the generalisability of the cellular model to predicting signals other than $V_{m,\mathrm{cell}}$. In particular, we predict that it is unclear whether V_{e}, which is derived from the cellular model through the bidomain equations, can be fully trusted. As the FPS is derived from V_{e}, the validity of the simulated FPS can also be put into question. Having said this, our study of the simulated FPS lays a pipeline for its robust analysis. When a cellular model including updated formulations for the five currents is produced, our work will help choose the best statistic to summarise time to repolarisation in the FPS.

We now compare the FPD_{max} and FPD_{zero} summary statistics with the APD_{90} reference. We assumed earlier that the closer the field potential duration end times are to the time of the $\overline{V_{\mathrm{m}}}^{\mathrm{rec}}$ 90% repolarisation, the more valid they are. In Figure 5.5, we observe that the time of the FPS repolarisation at zero-crossing is much closer to

the time of the $\overline{V_{\mathrm{m}}}^{\mathrm{rec}}$ 90% repolarisation than the FPS repolarisation at maximum. This suggests that FPD_{zero} is more valid than FPD_{max} in the control case.

We now determine which ionic current features are captured by the biomarkers. Based on their definitions, the biomarkers should capture the time that elapses between the start of depolarisation and the end of repolarisation. The fast sodium current (I_{Na}) is associated with depolarisation while the rapid delayed rectifier potassium current (I_{Kr}) and the slow delayed rectifier potassium current (I_{Ks}) are associated with repolarisation (see Section 2.1.1). These currents are non-zero for only specific times. We refer to the time at which a current becomes non-zero as its *start*, and the time at which a current becomes zero again as its *end*. Given the characteristics of I_{Na}, I_{Kr} and I_{Ks} previously outlined, we expect the time-to-repolarisation biomarkers to capture the duration between the start of I_{Na} and the end of I_{Kr} or I_{Ks}.

In Figure 5.5, the FPS spike trough and the $\overline{V_{\mathrm{m}}}^{\mathrm{rec}}$ 90% repolarisation occur simultaneously with the start of the I_{Na} current. This confirms that the biomarkers capture the start of depolarisation correctly. We note that the time of the $\overline{V_{\mathrm{m}}}^{\mathrm{rec}}$ 90% repolarisation is earlier than the end of I_{Kr}. The time of 90% repolarisation is also earlier than the end of I_{Kr} in simulations of adult native CMs [100]. However, this phenomenon is less pronounced in the latter case. The phenomenon is particularly marked here because of the prolonged duration of the I_{Kr} current in the Paci2013 model [16] as compared with the adult native CMs model used in [100]. The prolonged duration of the I_{Kr} current in the Paci2013 model contributes to the long duration observed here between the time of the $\overline{V_{\mathrm{m}}}^{\mathrm{rec}}$ 90% repolarisation and the end of I_{Kr}. After comparing the time of the $\overline{V_{\mathrm{m}}}^{\mathrm{rec}}$ 90% repolarisation to I_{Kr}, we consider the other repolarisation current, I_{Ks}. We observe that the $\overline{V_{\mathrm{m}}}^{\mathrm{rec}}$ 90% repolarisation captures the end of I_{Ks}. In summary, $\overline{V_{\mathrm{m}}}^{\mathrm{rec}}$ 90% repolarisation does not capture the end of I_{Kr}, but it does capture the end of I_{Ks}. The capture of the end of either of these two repolarisation currents is an indication that $\overline{V_{\mathrm{m}}}^{\mathrm{rec}}$ 90% repolarisation is a

	$[IC_{50}]_{\mathrm{CaL}}$	n_{CaL}	$[IC_{50}]_{\mathrm{Na}}$	n_{Na}	$[IC_{50}]_{\mathrm{Kr}}$	n_{Kr}
Nifedipine	4.34×10^1	0.56	7.98×10^3	1.38	3.13×10^4	0.69
Nitrendipine	9.20×10^1	0.53	2.89×10^3	0.84	2.12×10^4	0.39
Droperidol	7.67×10^3	1.16	4.19×10^3	1.02	3.70×10^2	0.62
Domperidone	9.21×10^3	0.94	1.85×10^3	1.13	8.50×10^1	1.16
Pimozide	5.92×10^1	0.77	2.50×10^2	1.93	5.00×10^1	1.02
Terfenadine	3.47×10^2	1.00	-	-	7.76×10^1	1.62
Disopyramide	4.38×10^5	1.00	2.25×10^4	1.22	1.50×10^4	0.37
Dl-sotalol	-	-	3.20×10^5	1.00	3.86×10^5	1.00
Quinidine	9.69×10^3	1.00	1.82×10^4	1.00	8.19×10^2	1.40
Ranolazine	1.79×10^5	1.00	3.40×10^4	1.49	9.00×10^3	1.20
Vandetanib	4.56×10^3	1.23	6.00×10^3	1.26	9.00×10^2	1.05
Tamoxifen	2.50×10^3	1.90	2.75×10^3	3.87	2.43×10^3	1.79

Table 5.2: Conductance-block parameters of the drugs considered in this study. These parameters were obtained with the CiPA protocol [92]. The subscript Kr corresponds to the rapid delayed rectifier ion channel (also referred to as *hERG*), Na to the fast sodium channel, CaL to the L-type calcium channel. The $[IC_{50}]$ values are given in nM. The symbol "-" indicates that the corresponding drug does not block the ion channel.

meaningful indicator of repolarisation. As $\overline{V_{\mathrm{m}}}^{\mathrm{rec}}$ 90% repolarisation captures the end of I_{Ks}, we conclude that APD_{90} captures the end of repolarisation correctly. The time of the FPS repolarisation at zero-crossing is also close to the end of I_{Ks}, which indicates that FPD_{zero} also captures the time to repolarisation well. In sharp contrast, the FPS repolarisation at maximum occurs before the I_{Ks} peak. This suggests that FPD_{max} does not reflect the time to repolarisation well.

Another test for the validity of the biomarkers FPD_{max} and FPD_{zero}, in addition to that of the underlying FPS model, is to determine whether the biomarkers are robust to drug perturbations. We investigate whether they are consistently close to APD_{90} as different drugs are added to the tissue. We also determine if they track the same ionic current features across varying drugs and concentrations. The conductance-block parameters for the different drugs we consider are presented in Table 5.2. These parameters were provided by Liudmila Polonchuk's laboratory at Roche.

5.2.1 Example I_{CaL} blocker: nifedipine

We first investigate the reliability of FPD_{zero} and FPD_{max} for capturing the time to repolarisation in drugs only blocking I_{CaL}. We focus on a representative drug of this class, nifedipine. We show how under the action of nifedipine FPD_{zero} and FPD_{max} fail to properly capture the repolarisation time in our simulated signal.

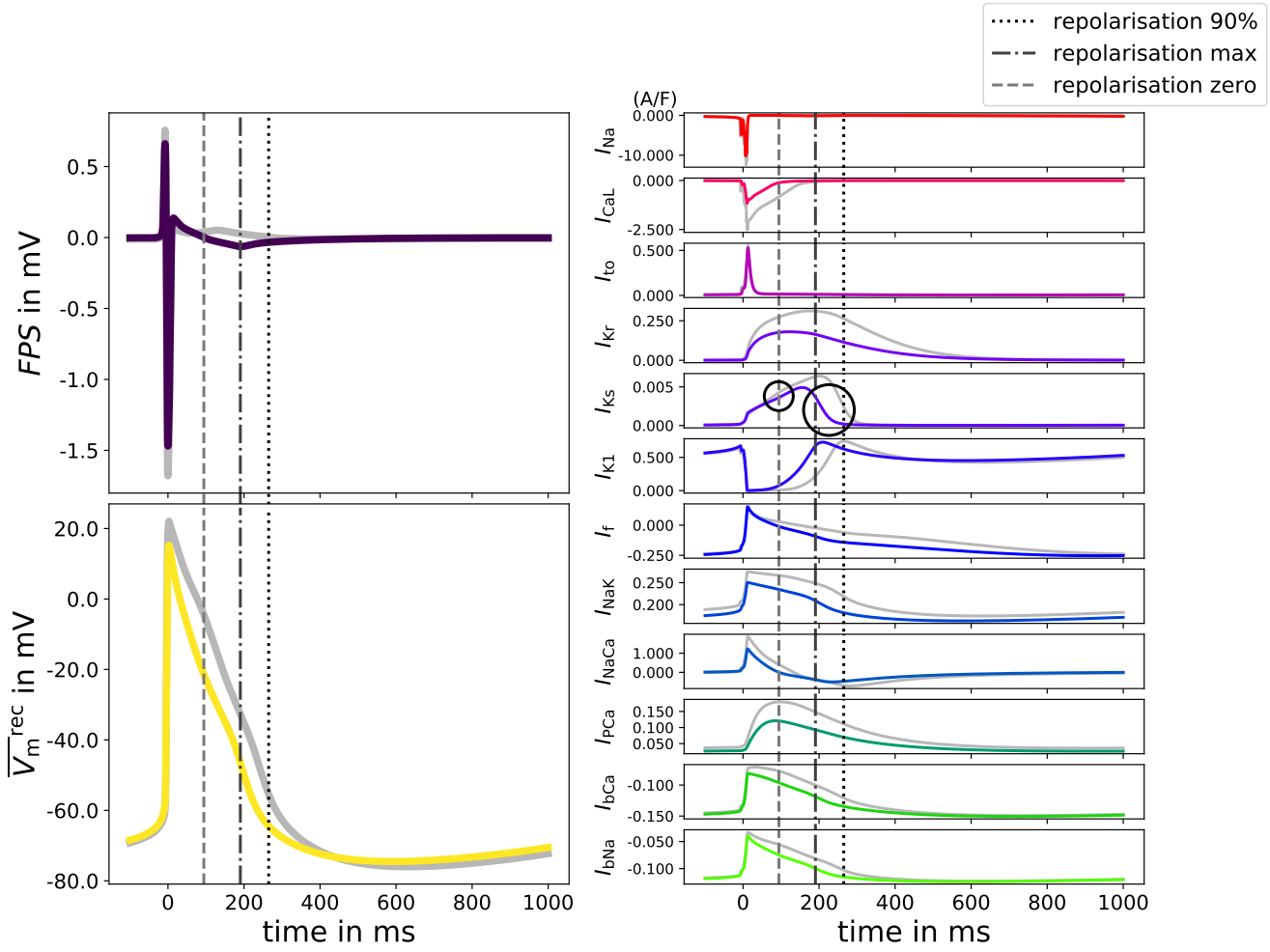


Figure 5.6: Comparison between simulated field potential, action potential and ionic currents for the second-to-last beat before 2006 s. This simulation was performed with the addition of nifedipine at concentration 100.00 nM. Coloured lines indicate the simulation results with addition of nifedipine while faint grey lines indicate the control case.

Figure 5.6 shows the effect of the addition of nifedipine at concentration 100.00 nM

on the FPS, the action potential signal, and the ionic currents. After the addition of the drug, the time of the FPS repolarisation at maximum is closer to the time of the $\overline{V_{\mathrm{m}}}^{\mathrm{rec}}$ 90% repolarisation than the time of the FPS repolarisation at zero crossing. This would suggest that FPD_{max} is a more reliable measure of field potential duration than FPD_{zero}. However, we can tell that this is not the case by observing the ionic current features captured by the FPS repolarisation at maximum. In the control case (Figure 5.5), the FPS repolarisation at maximum captures a time before the peak of I_{Ks}. By comparison, the FPS repolarisation at maximum captures a time after the peak of I_{Ks} in the nifedipine 100.00 nM case. In summary, the FPS repolarisation at maximum does not capture the same ionic features between the control and drug-pertubed case, for nifedipine. We notice that the repolarisation wave is inverted in the nifedipine 100.00 nM case, while it is not in the control case. This repolarisation wave inversion caused by the addition of nifedipine may explain the fact that the FPS repolarisation at maximum captures different ionic features between the control and drug-perturbed case. The inconsistency in the ionic features detected by the FPS repolarisation at maximum makes the comparison between control and drug-pertubed case difficult. The inconsistency suggests that relative changes in FPD_{max} caused by the addition of nifedipine are not reliable.

Similarly, we observe that the FPS repolarisation at zero-crossing has shifted from a time after the I_{Ks} peak in the control case (Figure 5.5) to a time before the peak of I_{Ks} in the nifedipine 100.00 nM case (Figure 5.6). Like the FPS repolarisation at maximum, the FPS repolarisation at zero crossing does not capture the same ionic features between the control and drug-pertubed case for nifedipine. A possible reason for this inconsistency is again the repolarisation wave inversion caused by the addition of nifedipine. We infer that the reliability of relative changes in FPD_{zero} between the control and drug-perturbed case is poor for nifedipine.

Given that nifedipine is the representative of I_{CaL} monoblocking drugs in our

study, we infer from our previous observations that the reliability of relative changes in FPD_{max} and FPD_{zero} is questionable for I_{CaL} monoblocking drugs. As previously noted in Section 3.1.3, the cellular model we use [16] inaccurately describes calcium dynamics within the cell [19, 70]. With the addition of an I_{CaL} perturbation, we speculate that this inaccuracy may lead to an unrealistic FPS. This potentially unrealistic behaviour may explain the unsatisfactory predictions we obtain with the biomarkers computed on the FPS, FPD_{max} and FPD_{zero}.

Figure 5.7 gives an overview of variables of interest for the addition of nifedipine at concentration 1000.00 nM. The FPS repolarisation at maximum and the FPS repolarisation at zero crossing capture the same ionic current features as in the nifedipine 100.00 nM case. These ionic current features are distinct from those captured by the FPS repolarisation at maximum and the FPS repolarisation at zero crossing in the control case. These observations bear both positive and negative connotations. The positive is that FPD_{max} and FPD_{zero} are consistent across the nifedipine cases. The negative is that FPD_{max} and FPD_{zero} are inconsistent with the control case at the two concentration of nifedipine tested. By contrast, we highlight that $\overline{V_{\text{m}}}^{\text{rec}}$ repolarisation 90% is consistent across the control, nifedipine 100.00 nM and 1000.00 nM cases. The $\overline{V_{\text{m}}}^{\text{rec}}$ repolarisation 90% always captures the end of I_{Ks}. This consistency suggests that the underlying $\overline{V_{\text{m}}}^{\text{rec}}$ signal reacts realistically to nifedipine. This is in contrast with the potentially unrealistic behaviour of the FPS. The previously hypothesised lack of generalisability of the cellular model to V_{e} may explain the difference in validity between the simulated FPS and $\overline{V_{\text{m}}}^{\text{rec}}$.

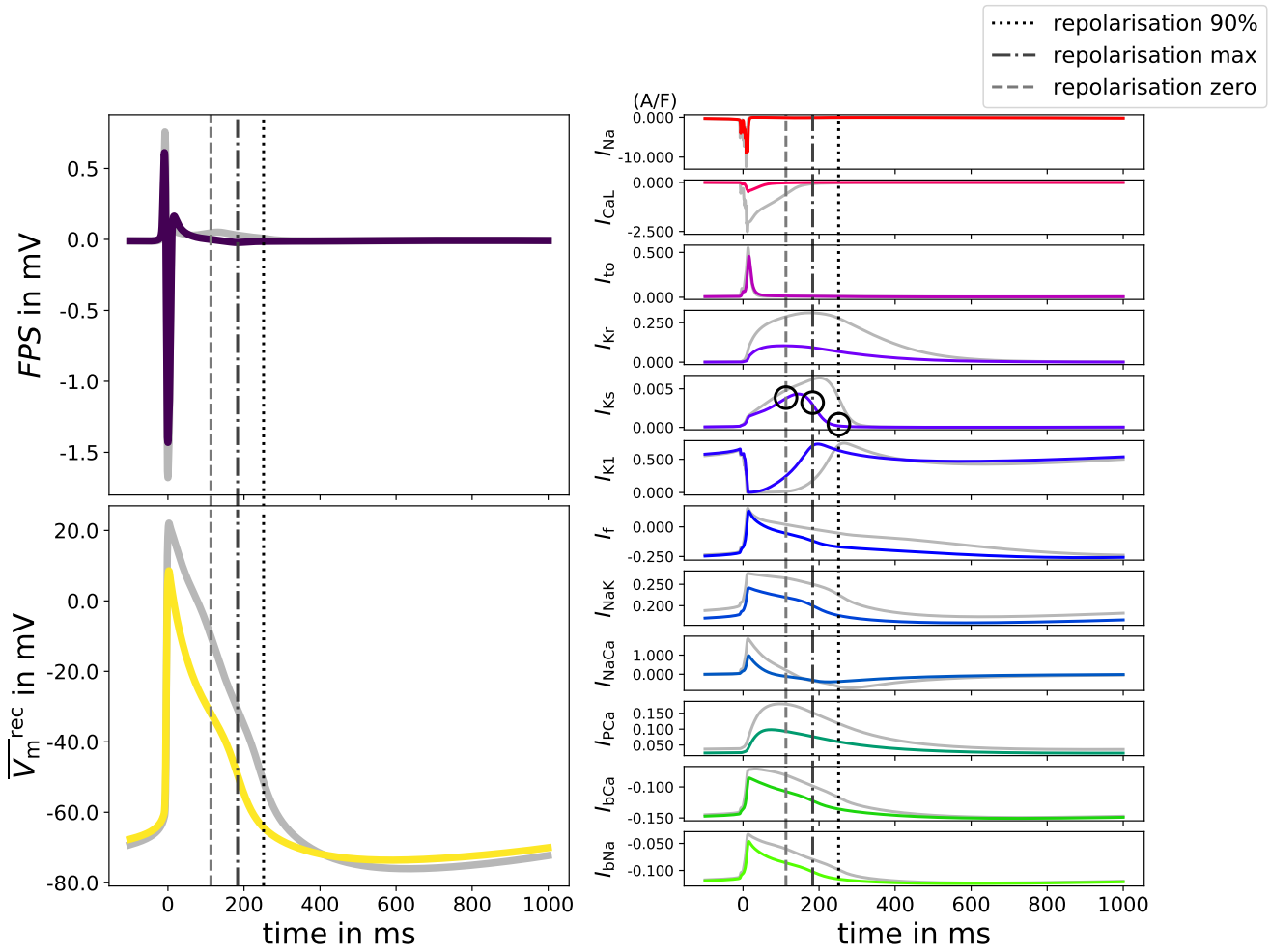


Figure 5.7: Comparison between simulated field potential, action potential and ionic currents for the second-to-last beat before 2006 s. This simulation was performed with the addition of nifedipine at concentration 1000.00 nM.

5.2.2 Example I_{Kr} blocker: droperidol

The FPD_{max} and FPD_{zero} biomarkers perform better with the I_{Kr} blocking drug droperidol. They display consistent behaviour in tracking the same ionic current features across concentrations. Figure 5.8 shows results for droperidol at concentration 316.46 nM, and Figure 5.9 for droperidol at concentration 1000.00 nM. As in the control case (Figure 5.5), the FPS repolarisation at zero-crossing is near the end of I_{Ks} for both droperidol concentrations. The FPS repolarisation at maximum captures

times before the peak of I_{Ks} in both the control and droperidol cases.

We observe that the FPS repolarisation at maximum is far from the $\overline{V_{\mathrm{m}}}^{\mathrm{rec}}$ repolarisation 90% for both of the concentrations of droperidol. This calls into question the validity of FPD_{max}. Conversely, the FPS repolarisation at zero-crossing is close to $\overline{V_{\mathrm{m}}}^{\mathrm{rec}}$ for both of the concentrations of droperidol. We infer that FPD_{zero} is a qualitatively reliable biomarker for I_{Kr} blocking drugs. In addition, the FPS theoretical model may be more reliable for I_{Kr} blocking drugs. The $\overline{V_{\mathrm{m}}}^{\mathrm{rec}}$ repolarisation 90% again performs best at detecting the repolarisation. As in the control case, it captures the end of I_{Ks} for both droperidol concentrations.

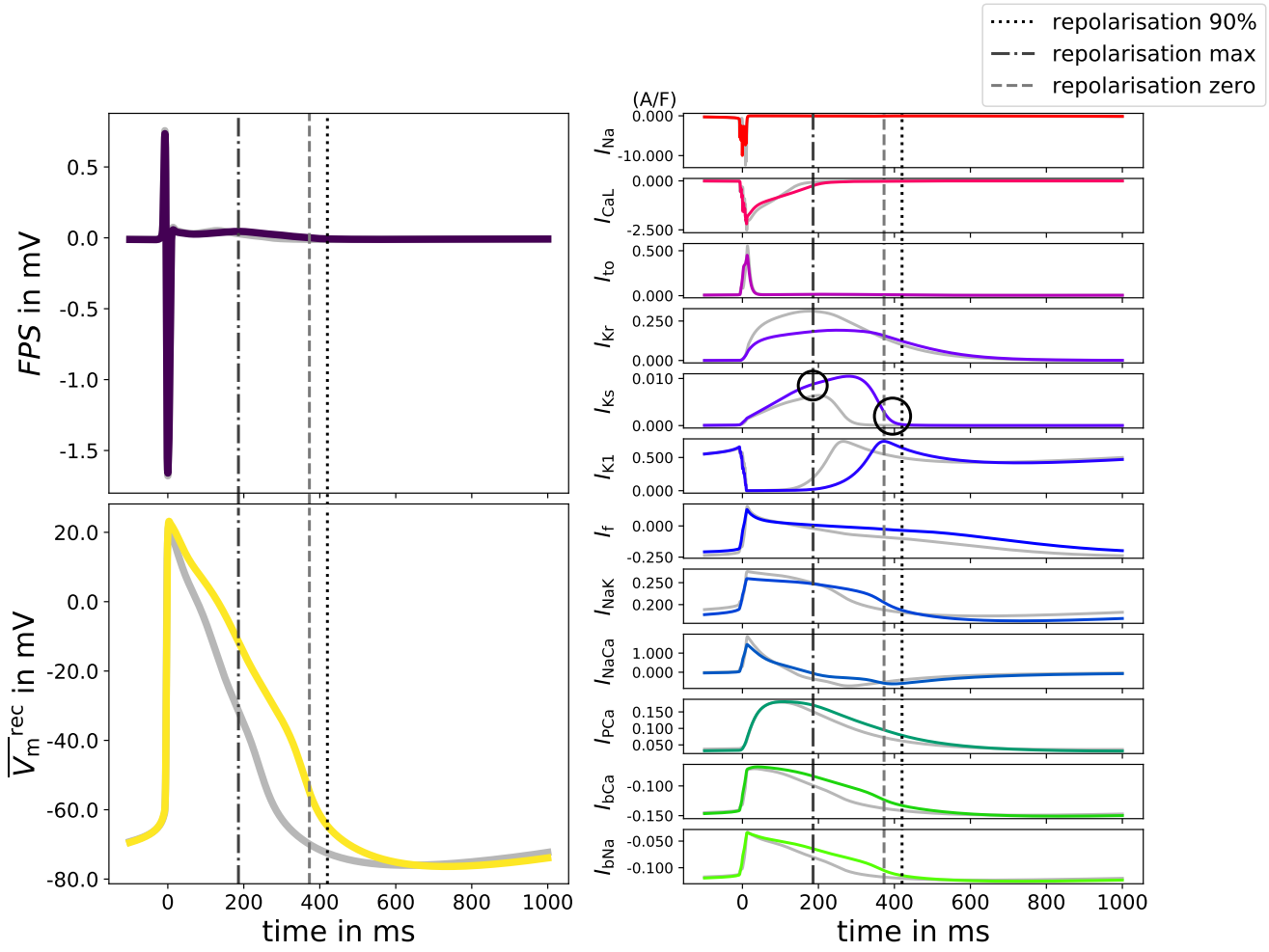


Figure 5.8: Comparison between simulated field potential, action potential and ionic currents for the second-to-last beat before 2006 s. This simulation was performed with the addition of droperidol at concentration 316.46 nM.

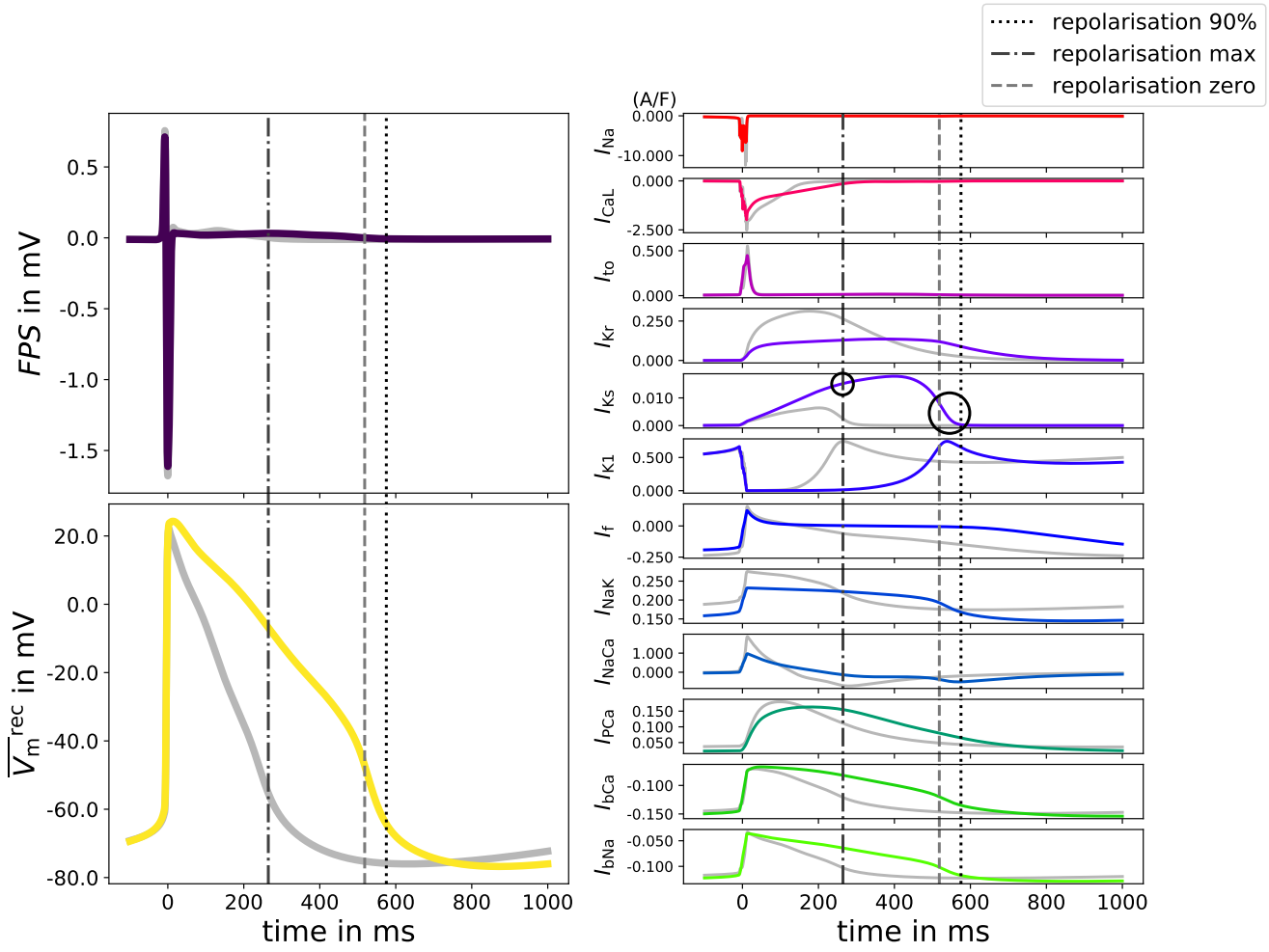


Figure 5.9: Comparison between simulated field potential, action potential and ionic currents for the second-to-last beat before 2006 s. This simulation was performed with the addition of droperidol at concentration 1000.00 nM.

5.2.3 Example I_{CaL} and I_{Kr} balanced blocker: pimozide

We now study the class of drugs for which the I_{CaL} and I_{Kr} blocking effects are balanced. We study pimozide as a representative of this class. We find that pimozide presents a case where FPD_{zero} is more reliable than FPD_{max}. The reason is that the FPS repolarisation at zero-crossing is easier to detect correctly than the FPS repolarisation at maximum. We explain the difficulty in correctly detecting the FPS repolarisation at maximum on the pimozide-perturbed FPS here.

Figure 5.10 displays the results for pimozide at concentration 9.49 nM, and Figure 5.11 the results for pimozide at concentration 30.00 nM. The FPS repolarisation at zero-crossing is close to the I_{Ks} end for both concentrations (closer for 9.49 nM, however). This suggests that FPD_{zero} is an acceptable biomarker for measuring the time to repolarisation in the pimozide-perturbed case.

The FPD_{max} summary statistic is not detected as reliably as FPD_{zero} for pimozide. In Figure 5.10, the FPS repolarisation at maximum marks a time before the peak of I_{Ks}. This is consistent with the FPS repolarisation at maximum captured in the control case (see Figure 5.5). However, Figure 5.11 introduces an instance where the repolarisation at maximum captures a time much closer to the end of the repolarising currents. This inconsistency can be explained by the complexity of the detection of the FPS repolarisation at maximum. In order to detect the repolarisation at maximum with a rule-based method, various thresholds have to be enforced. In particular, a minimum width for the repolarising peak was selected to improve detection accuracy. In the ambiguous case presented in Figure 5.11, the extremum automatically detected is up for debate. A previous repolarisation extremum, too flat to be detected by our algorithm, could be argued to be the correct one. Having said this, the difficulty in correctly detecting the repolarisation at maximum is a drawback for the use of FPD_{max}. By contrast, the FPD_{zero} does not suffer from the same detection uncertainty.

Again, the $\overline{V_{\mathrm{m}}}^{\mathrm{rec}}$ repolarisation 90% marks the end of the I_{Ks} current for pimozide, as it did for all the other cases presented so far. As previously stated, this behaviour is satisfactory for time-to-repolarisation biomarkers. It confirms that APD_{90} captures time to repolarisation well.

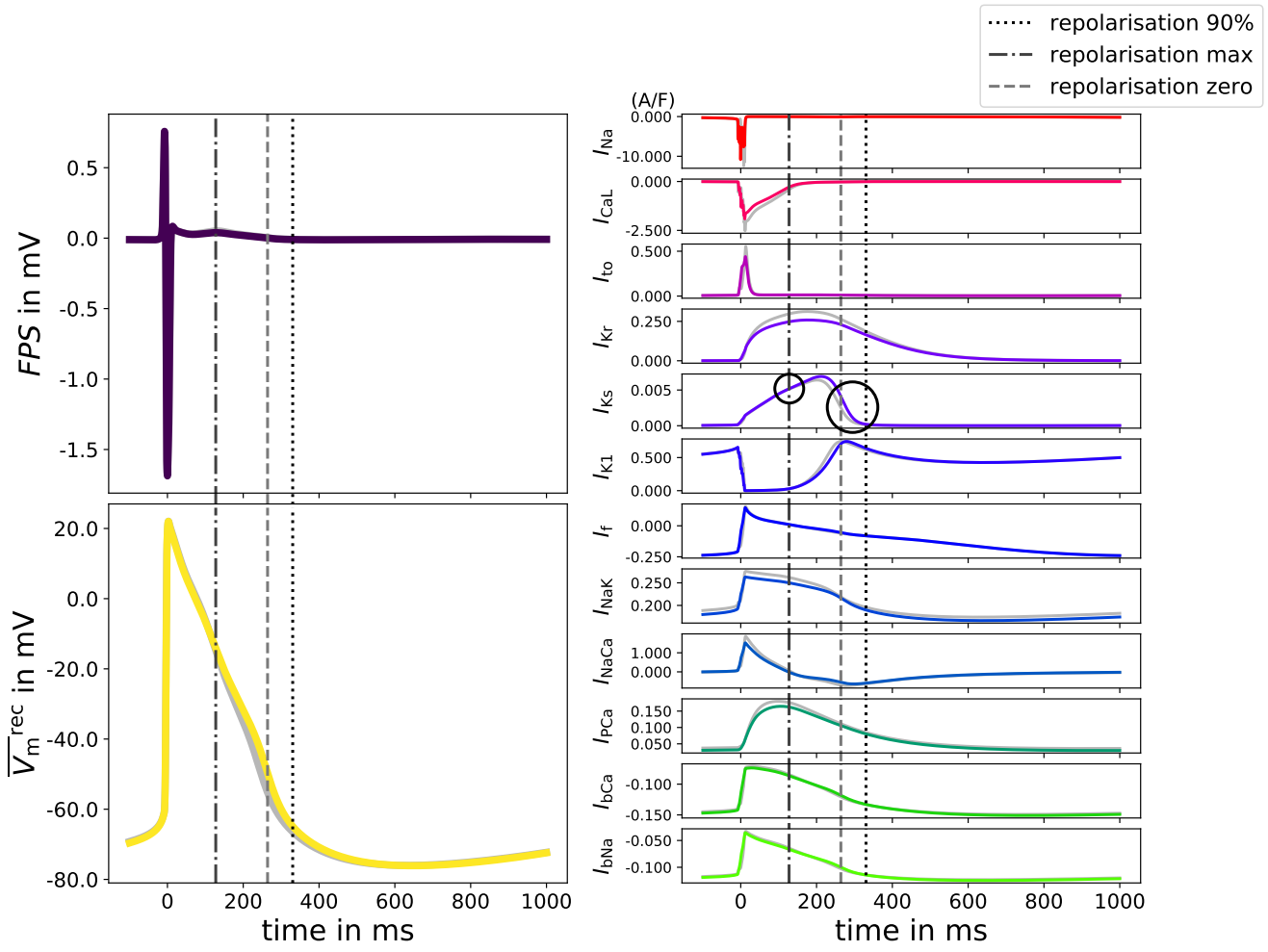


Figure 5.10: Comparison between simulated field potential, action potential and ionic currents for the second-to-last beat before 2006 s. This simulation was performed with the addition of pimozide at concentration 9.49 nM.

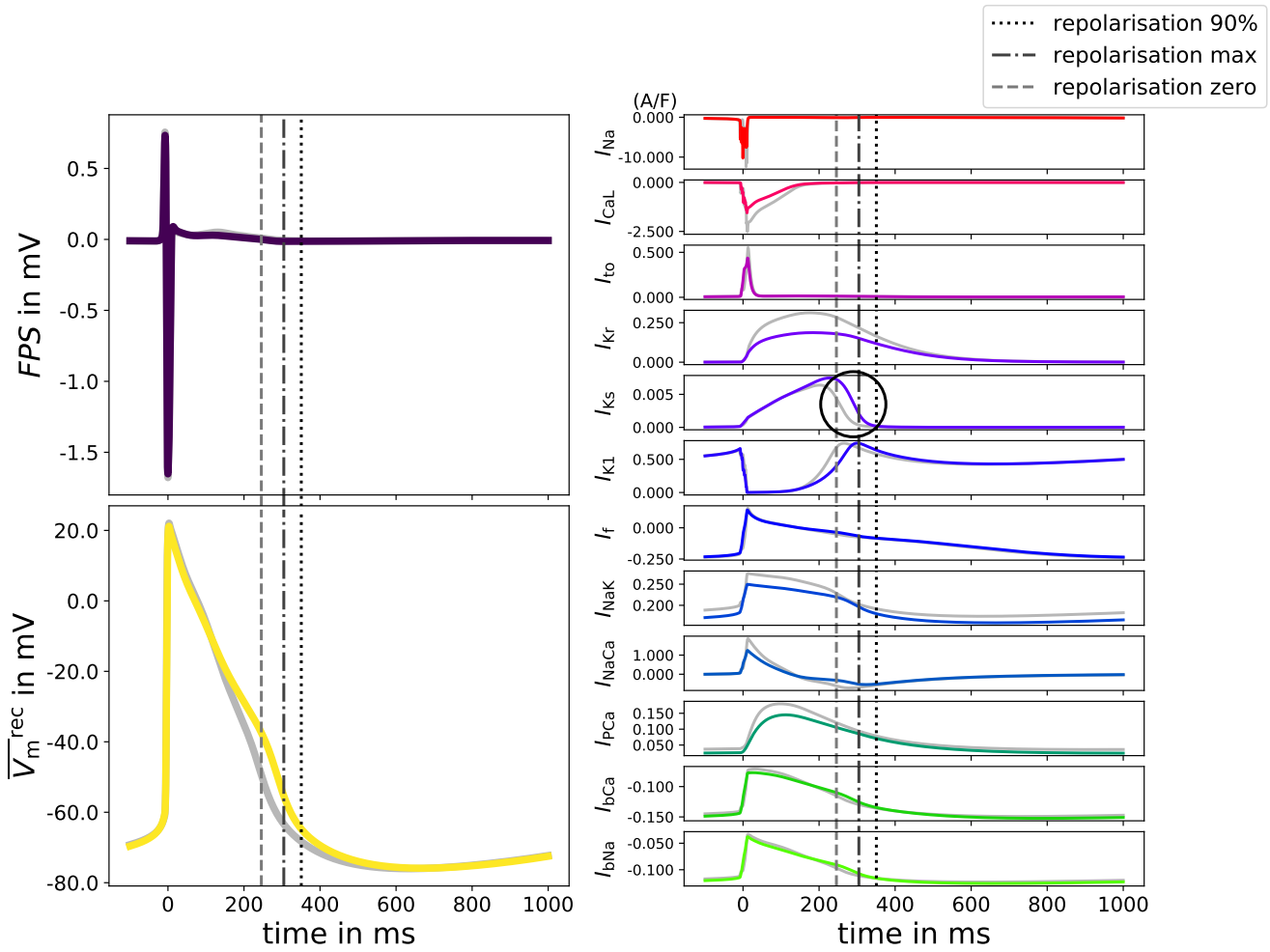


Figure 5.11: Comparison between simulated field potential, action potential and ionic currents for the second-to-last beat before 2006 s. This simulation was performed with the addition of pimozide at concentration 30.00 nM.

5.2.4 Example I_{Na}, I_{CaL} and I_{Kr} multiblocker: quinidine

Our comparison of time-to-repolarisation biomarkers ends with the multi-channel blocker quinidine. Quinidine blocks I_{CaL}, I_{Kr}, and, for the first time in the comparison, I_{Na}. Figure 5.12 presents results for quinidine at concentration 9490.00 nM. No beat can be observed in the FPS or $\overline{V_m}^{rec}$ at the highest quinidine concentration (30 000.00 nM), for the phenotype realisation studied. This is the reason why results for a single quinidine concentration are shown here.

In Figure 5.12, the FPS repolarisation at zero crossing is closer to the $\overline{V_{\mathrm{m}}}^{\mathrm{rec}}$ repolarisation 90% than the FPS repolarisation at maximum. This suggests that FPD_{zero} is more reliable than FPD_{max} for capturing the time to repolarisation for I_{Na}, I_{CaL} and I_{Kr} multiblockers. All the time-to-repolarisation biomarkers capture the same repolarising ionic current features as they did in the control case. This is evidence of their consistency. As in the control case, the $\overline{V_{\mathrm{m}}}^{\mathrm{rec}}$ repolarisations 90% and the FPS repolarisation at zero crossing both capture a time close to the end of the I_{Ks} current (the $\overline{V_{\mathrm{m}}}^{\mathrm{rec}}$ repolarisation 90% is closer, however). The FPS repolarisation at maximum captures a time before the peak of I_{Ks}, as it did in the control case.

The results obtained with quinidine strengthens our confidence in FPD_{zero} and APD_{90} for measuring time to repolarisation in I_{CaL}, I_{Kr} and I_{Na} multi-channel blocking drugs. Once more, the validity of FPD_{max} is called into question, in the case of I_{CaL}, I_{Kr} and I_{Na} multi-channel blocking drugs here.

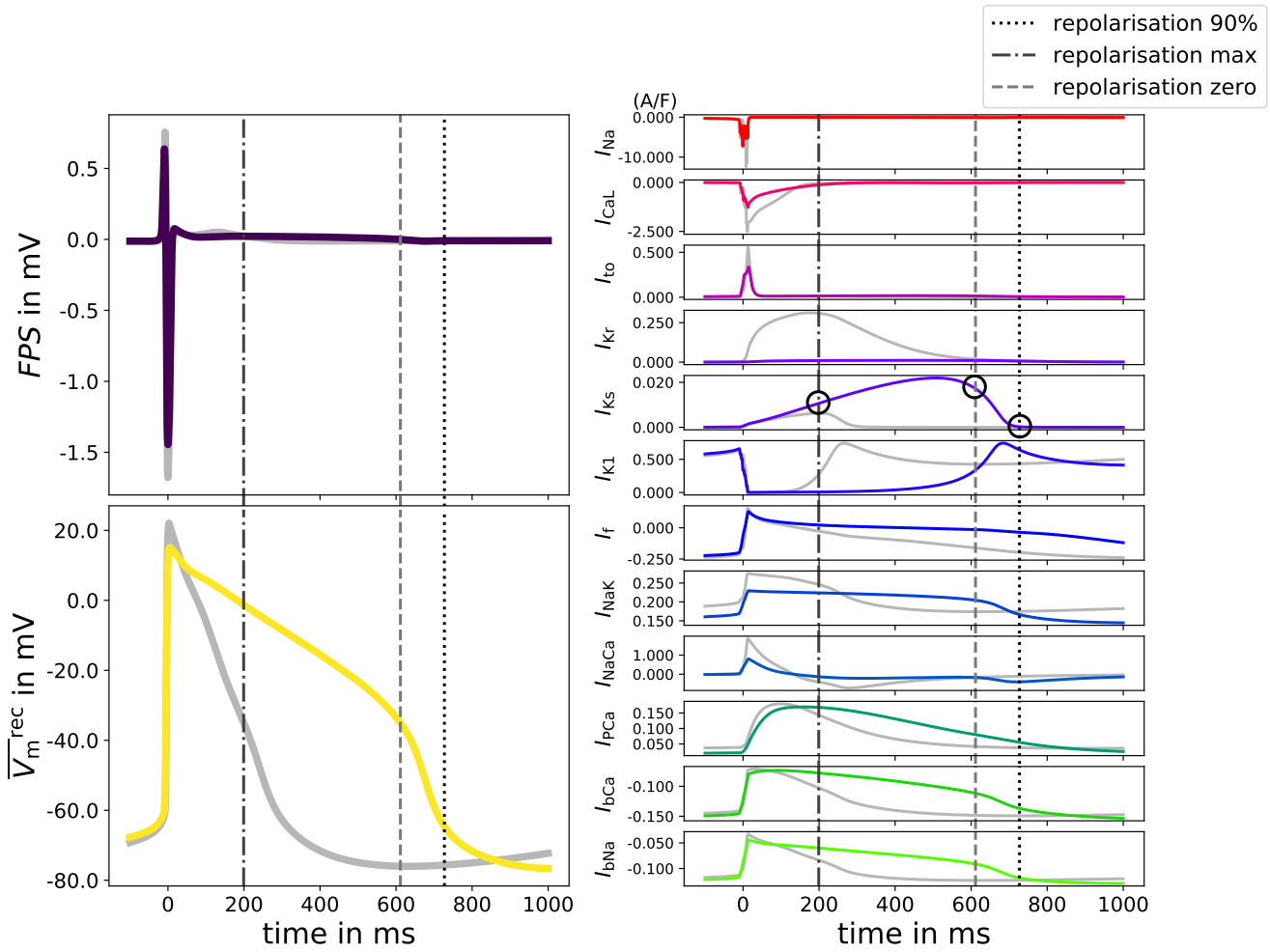


Figure 5.12: Comparison between simulated field potential, action potential and ionic currents for the second-to-last beat before 2006 s. This simulation was performed with the addition of quinidine at concentration 9490.00 nM.

5.2.5 Conclusion

The validity of the time-to-repolarisation biomarkers based on the FPS, $FPD_{\max}$ and FPD_{zero}, depends on the drug applied. The effect of the I_{Kr} blockers, I_{Kr} and I_{CaL} balanced blockers, and the I_{Kr}, I_{CaL} and I_{Na} multichannel blockers, can be evaluated correctly by the FPD_{zero} biomarker. By contrast, the $FPD_{\max}$ biomarker substantially differs from the APD_{90} gold standard for these classes of drugs. This points to a weakness of the $FPD_{\max}$ biomarker. This being said, $FPD_{\max}$ consistently tracks the

same ionic current features for I_{Kr} monoblockers and I_{Kr}, I_{CaL} and I_{Na} multichannel blockers. This consistency advocates in favour of the validity of the relative changes in FPD_{max} between control and drug-perturbed cases, across concentrations, for these classes of drugs. Precautions should be taken when interpreting relative changes in FPD_{max} results for I_{Kr} and I_{CaL} balanced blockers. For these drugs the detection of the correct repolarisation maximum is difficult and outlying results may occur. Finally, FPD_{max} and FPD_{zero} are unreliable for I_{CaL} blockers. This observation can be explained by errors in the theoretical model and the inversion of the repolarisation wave (see Section 5.2.1 for details).

As expected, APD_{90} correctly captured the time to repolarisation in all cases. The experimental signals in our possession do not however include $\overline{V_{\mathrm{m}}}^{\mathrm{rec}}$, so that the experimental APD_{90} cannot be computed. Given this limitation, going forwards the experimental FPD_{zero} or FPD_{max} will be compared to the simulated FPD_{zero}, FPD_{max} or APD_{90}. We will utilise limitations delineated in this section to interpret results.

5.3 Influence of ρ_{V} on action potential duration

The phenotypes of the cells present in the hECTs used in our experiments were not measured. Based on the literature, we chose the average ρ_{v} in the simulated hECTs to be 0.54 (see Section 4.2). Here, we test the model robustness to variations in ρ_{v}. Figure 5.13 presents the sensitivity of the relative change $\Delta_{\mathrm{rel}}^{APD_{90}}$, defined in Equation (4.11), to changes in ρ_{v}. We chose to study the relative changes in APD_{90} because of the reliability of this biomarker as a measure of time to repolarisation (see Section 5.2).

We observe in Figure 5.13 that $\Delta_{\mathrm{rel}}^{APD_{90}}$ does not vary monotonically with ρ_{V}. A biological explanation of this phenomenon can be found in the fact that ρ_{v} denotes the proportion of VL cells at a point in the tissue. Values of ρ_{v} in $]0, 1[$ do not

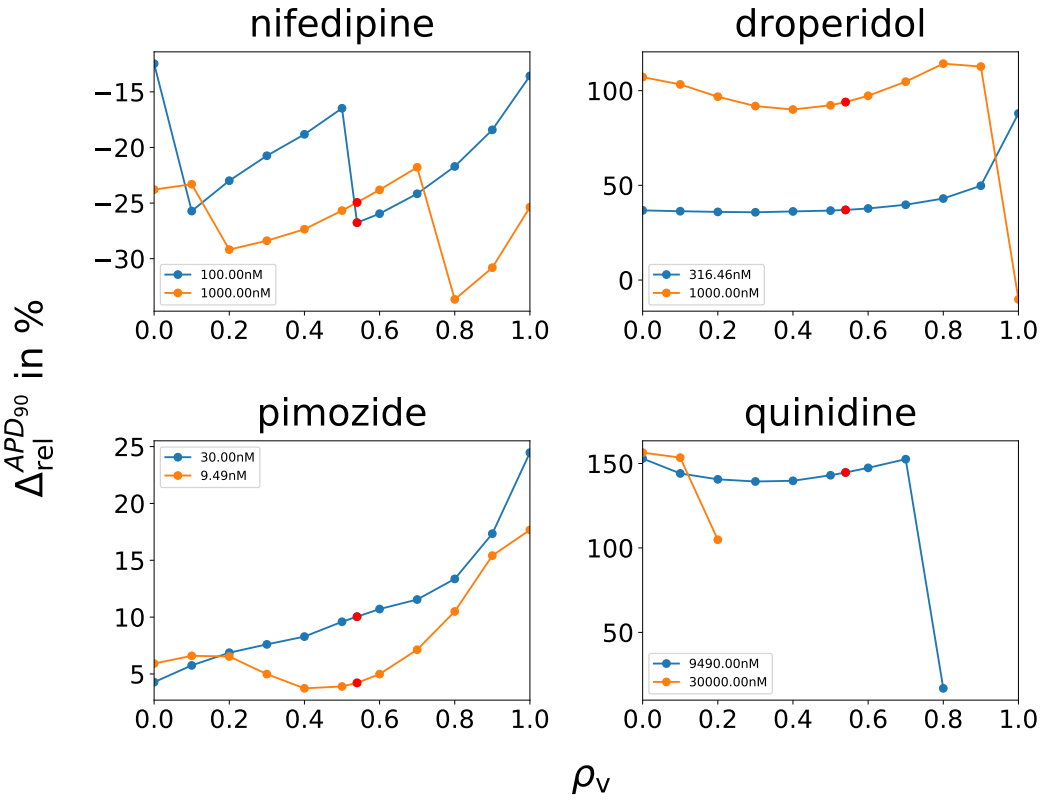


Figure 5.13: Changes in APD_{90} relative to the control case, as ρ_{v} is varied. The APD_{90} presented here are computed on $V_{\text{m,cell}}$. Four drugs are considered, including one I_{CaL} blocker (nifedipine), one I_{Kr} blocker (droperidol), one I_{CaL} and I_{Kr} balanced blocker (pimozide), and one I_{Na}, I_{CaL} and I_{Kr} multiblocker (quinidine). The red dots indicate where $\rho_{\text{v}} = 0.54$. Missing values indicate that no beat could be detected for the corresponding value of ρ_{v}. In all cases, APD_{90} was extracted at its steady state, as defined by Equation (4.14).

define hybrid AL-VL cells. Instead, they define a mixed group of cells with either VL or AL phenotype within a small area relative to the surface of the tissue [21]. Within this small area, the presence of even a small proportion of cells belonging to one phenotype can have a large impact on the electrophysiology of the other cells. This can explain the large changes in $\Delta_{\text{rel}}^{APD_{90}}$ for droperidol between the cases where $\rho_{\text{v}} = 0.9$ and where $\rho_{\text{v}} = 1.0$. The complete absence of AL cells appears to have had a drastic effect on $\Delta_{\text{rel}}^{APD_{90}}$ in this case. A mathematical explanation for the observed variation of $\Delta_{\text{rel}}^{APD_{90}}$ with ρ_{V} originates in the nonlinearity of the underlying cellular

model [16]. Given this nonlinearity, there is no reason for the derived output $\Delta_{\text{rel}}^{APD_{90}}$ to vary linearly with the input ρ_{v}.

5.4 *In silico* and *in vitro* effects of drugs on time-to-repolarisation biomarkers

Previous sections have gathered insight on the biological information contained in the FPS (Section 5.1), characterised the biomarkers limitations (Section 5.2), and presented the influence of the hECT phenotypes on time to repolarisation (Section 5.3). These sections have laid the foundations for the study of the effect of drugs on the time-to-repolarisation summary statistics FPD_{max}, FPD_{zero} and APD_{90}. In addition to these summary statistics, we also study here the closely related summary statistics $FPDc_{\text{max}}$, $FPDc_{\text{zero}}$ and $APDc_{90}$. These summary statistics are normalised for variations in beat duration with Fridericia's formula [101], such that

$$FPDc_{\text{zero}}[\text{ms}/\text{s}^{\frac{1}{3}}] = \frac{FPD_{\text{zero}}[\text{ms}]}{beat\ duration^{\frac{1}{3}}[\text{s}^{\frac{1}{3}}]}, \tag{5.2}$$

$$FPDc_{\text{max}}[\text{ms}/\text{s}^{\frac{1}{3}}] = \frac{FPD_{\text{max}}[\text{ms}]}{beat\ duration^{\frac{1}{3}}[\text{s}^{\frac{1}{3}}]}, \tag{5.3}$$

$$APDc_{90}[\text{ms}/\text{s}^{\frac{1}{3}}] = \frac{APD_{90}[\text{ms}]}{beat\ duration^{\frac{1}{3}}[\text{s}^{\frac{1}{3}}]}, \tag{5.4}$$

where units are indicated in square brackets and are as found in [102] or in the CardioExcyte96 software.

We have conducted an *in silico* study exploring the impact of 12 drugs, given at two different concentrations, on 10 different phenotype realisations of hECT. We have performed a tissue simulation for each drug, each concentration, and each phenotype realisation. In addition, we have conducted a tissue simulation for each phenotype realisation in control conditions (no drug). In total, we performed 250 tissue simulations. We also performed simulations of the cellular model (see Section 3.1.3) for each

drug, each concentration, and three different phenotypes. The three different phenotypes considered for cellular simulations are the ventricular phenotype ($\rho_V = 1$), the atrial phenotype ($\rho_V = 0$) and a mixed phenotype such that $\rho_V = 0.54$. The value of ρ_V chosen in the mixed phenotype cellular simulation corresponds to the average value of ρ_V across phenotype distribution realisations (previously denoted by μ, see Section 3.5). With this choice of ρ_V we aim for the mixed phenotype cellular simulation to approximate the average behaviour of the tissue model across phenotype distribution realisations. Here, we determine whether there is similarity between the predictions of the mixed phenotype cellular simulations and those of the tissue simulations.

We compared the simulations to experiments conducted for the same 12 drugs and two concentrations as those considered in the simulations. We possess up to five experimental repeats for each experimental condition. One repeat corresponds to the addition to one hECT of a given drug at a given concentration. We have compared the time to repolarisation between simulated and experimental data by evaluating the differences between the same biomarker (e.g. FPD_{zero}) computed on the simulated and experimental traces. In addition, we have contrasted the simulated APD_{90} and $APDc_{90}$ with the experimental FPD_{zero}, $FPDc_{\text{zero}}$, FPD_{max}, and $FPDc_{\text{max}}$. The motivation for the latter comparisons is that all of the biomarkers listed are meant to capture the same underlying value that is the time to repolarisation. We have shown in Section 5.2 that APD_{90} is the best biomarker to capture time to repolarisation. As APD_{90} was not determined experimentally, we have compared the simulated APD_{90} to experimental field potential duration biomarkers.

The first step in our comparison was to exclude inconsistent experimental traces. We discarded an experimental trace if

$$\sigma_{\boldsymbol{FPD}_{\mathbf{zero}}} \geq 25\% \times \widetilde{FPD}_{\text{zero}}, \tag{5.5}$$

where $\sigma_{\boldsymbol{FPD_{zero}}}$ is the standard deviation of FPD_{zero} in the trace considered, and $\widetilde{FPD}_{\text{zero}}$ is the median value of FPD_{zero} in the trace. This heuristic allows to exclude experimental traces where there is too much intra-trace variation to trust the measurement performed.

Many drugs, drug concentrations, and simulated realisations or experimental repeats were analysed. We reduced the dimensionality of this *in silico-in vitro* dataset by computing the median summary statistic value among realisations (for simulations) or repeats (for experiments). The median experimental summary statistic value for a drug, d, at a concentration, c, is denoted by $\widetilde{SS}^{d,c}_{\text{exp}}$, and the median simulated summary statistic value for d at c is $\widetilde{SS}^{d,c}_{\text{sim}}$. If more than 60% of experimental traces for a given drug concentration were either excluded for satisfying Equation (5.5) or were such that no biomarker could be detected (e.g. because of beat cessation), we consider that $\widetilde{SS}^{d,c}_{\text{exp}}$ is not defined. Similarly, if more than 60% of simulated traces were such that no biomarker could be detected, $\widetilde{SS}^{d,c}_{\text{sim}}$ is not defined. In addition, we excluded the experimental traces with early after depolarisations (EADs) or ectopic beats from the calculation of $\widetilde{FPD}^{d,c}_{\text{max,exp}}$. The reason for this exclusion is that our algorithm mistakes the EADs and the ectopic beats for FPS repolarisations at maximum in those traces.

We define a metric to assess the closeness of experimental and simulated results. The metric we chose is the average root mean squared error between drugs, $\overline{RMSE_d}$, such that

$$\overline{RMSE_d} = \frac{1}{|D|} \sum_{d \in D} RMSE_d, \tag{5.6}$$

where the root mean squared error for d, $RMSE_d$, is defined as

$$RMSE_d = \sqrt{\frac{1}{|C_d|} \sum_{c \in C_d} \left(\widetilde{SS}^{d,c}_{\text{exp}} - \widetilde{SS}^{d,c}_{\text{sim}} \right)^2}. \tag{5.7}$$

The set of concentrations of d with defined $\widetilde{SS}^{d,c}_{\text{exp}}$ and $\widetilde{SS}^{d,c}_{\text{sim}}$ is denoted by C_d. Finally,

sim. biomarker, exp. biomarker	sim. tissue	sim. mixed	sim. atrial	sim. ventricular
FPD_{zero}, FPD_{zero}	25.8	-	-	-
$FPDc_{\text{zero}}$, $FPDc_{\text{zero}}$	24.4	-	-	-
APD_{90}, FPD_{zero}	28.6	29.7	33.4	52.0
$APDc_{90}$, $FPDc_{\text{zero}}$	24.6	25.8	28.4	49.2
FPD_{max}, FPD_{max}	49.1	-	-	-
$FPDc_{\text{max}}$, $FPDc_{\text{max}}$	46.0	-	-	-

Table 5.3: Average root mean squared error of the relative change in biomarkers between all 12 drugs. The difference between the simulated biomarker and the experimental biomarker given in the first column is used to compute the RMSE. In the case of simulated APD_{90}, we have included tissue as well as single cell results. The label "sim. mixed" corresponds to the simulation of the single cell model with $\rho_{\text{V}} = 0.54$. Drug concentrations where any biomarker was absent were not included in the RMSE computation. This ensured the fairness of the comparison. The values are given in percentage points. The abbreviation "sim." stands for simulated, and the abbreviation "exp." stands for experimental. The summary statistics APD_{90} and $APDc_{90}$ refer to *tissue* simulation results (second column) as well as *cellular* simulation results (third to fifth columns).

the 12 drugs we consider in the comparison (listed in Table 5.2) form a set called D.

A summary of the comparison between experimental and simulated results is given in Table 5.3. Henceforth, we use APD_{90} and $APDc_{90}$ to refer to both *tissue* simulation results as well as *cellular* simulation results. When considering APD_{90} and $APDc_{90}$ summary statistics, we specify their origin (tissue or cell) when unclear from context. We can observe in Table 5.3 that the comparison between experimental and simulated $FPDc_{\text{zero}}$ has the smallest average root mean squared error among the biomarkers compared. This signifies that the $FPDc_{\text{zero}}$ biomarker yields the closest match between experimental and simulated data. In this sense, the $FPDc_{\text{zero}}$ biomarker performs best. This result can be explained by three reasons. Firstly, FPD_{zero} can be more reliably computed than FPD_{max} (as explained in Section 5.2). Secondly, the same biomarker ($FPDc_{\text{zero}}$) was compared between simulations and experiments, as opposed to the mixed-biomarker comparisons we performed with the simulated APD_{90}. Lastly, Fridericia's correction for beat duration lessens the impact

of differences in beat duration between experimental and simulated data.

The second best results are obtained by comparing the simulated tissue $APDc_{90}$ and the experimental $FPDc_{\text{zero}}$. There is only a 0.2 percentage point difference between these results and those obtained with the simulated $FPDc_{\text{zero}}$. The reasons for this performance are the remarkable precision of APD_{90} in capturing time to repolarisation (see Section 5.2), Fridericia's correction, and the good performance of FPD_{zero} for capturing time to repolarisation in experimental data. The comparison between the simulated mixed cellular $APDc_{90}$ and the experimental $FPDc_{\text{zero}}$ achieves the third best results. A small 1.2 percentage point difference separates this predictive performance with that achieved with the simulated $FPDc_{\text{zero}}$. This shows that the cellular model can give a prediction for the time to repolarisation that is almost as accurate as the best prediction obtained with the tissue model. This observation supports the use of the cellular model as a computationally inexpensive alternative to tissue simulations.[1] The comparison between simulated atrial $APDc_{90}$ and experimental $FPDc_{\text{zero}}$ achieves the fourth best results. Only a 4.0 percentage point error is added to the error incurred with the $FPDc_{\text{zero}}$ comparison. This result indicates that even the original AL Paci2013 model predicts the experimental data well relative to the best prediction achieved by the tissue model. Therefore, simulated atrial $APDc_{90}$ provides the simplest way to predict experimental $FPDc_{\text{zero}}$ with error only slightly higher than that achieved with the simulated $FPDc_{\text{zero}}$. In addition, the simulated atrial $APDc_{90}$ is obtained from a cellular simulation, which is quick to compute.

The worst comparisons are obtained with the simulated ventricular APD_{90} and $APDc_{90}$. The comparisons with the experimental FPD_{zero} and $FPDc_{\text{zero}}$ are given in Table 5.3 and the comparisons with the experimental FPD_{max} and $FPDc_{\text{max}}$ in Table B.1. We hypothesise from the poor comparison results that the VL phenotype

[1] Cellular simulations can be executed at a fraction of the computational cost of tissue simulations. A cellular simulation only takes about 1 min 30 s to compute on one processor core. This is 420 times quicker than the tissue simulations, with eight times less processor cores (the tissue simulation takes about 10 h30 min on eight processor cores, see Table 4.5).

does not reflect the mixed phenotype present in the tissue. We know that the tissue is paced by its most AL region (where ρ_V is minimal). This AL pacing may explain the inability of VL APD_{90} and $APDc_{90}$ to reproduce the experimentally observed field potential duration. The second worse comparisons are those contrasting simulated and experimental $FPD_{\max}$ and $FPDc_{\max}$. The main reason for these poor results is the difficulty in properly detecting the FPS repolarisation at maximum, as explained in Section 5.2.

In absolute terms, Table 5.3 paints a dissatisfying picture of the quality of the theoretical predictions. The best prediction we achieve, with FPD_{zero}, bears a 24.4 percentage points average error. Given that the median simulated control $FPDc_{\text{zero}}$ is 248 ms, an average 24.4 percentage point error translates to a 61 ms absolute error. As presented in Chapter 2, a more than 10 ms increase in heart-rate-corrected QT interval is a cause for concern of TdP risk. In this context, a 61 ms average error is very substantial. Next, we assess the quality of our predictions at a more fine-grained level. We break down the assessment by class of ion channel-blocking drugs. Our motivation for this categorisation originates from the observation that the validity of the time-to-repolarisation biomarkers, as well as the validity of the underlying mathematical model, are drug-dependent (see Section 5.2).

5.4.1 I_{CaL} blockers

We begin the *in silico-in vitro* comparison with the two I_{CaL} channel blockers present in our dataset, nifedipine and nitrendipine. In Figure 5.14 we compare the simulated and experimental FPD_{zero}. We observe that both simulated and experimental results predict a decrease in FPD_{zero} relative to the control case when the drugs are added. This is in line with the expected effects of I_{CaL} blockers (see Section 2.1.1). We notice that FPD_{zero} decreases as the drug concentration is increased for both drugs in experiments, and for nitrendipine only in simulations. The observed simulated increase

of FPD_{zero} as the drug concentration of nifedipine is increased is likely due to model error and the repolarisation wave inversion (see Section 5.2.1). The large interquartile range obtained for the experimental FPD_{zero} with the addition of nifedipine at 1000 nM can be explained. The value obtained for FPD_{zero} in well H2 is an outlier relative to the other experimental FPD_{zero} values. The experimental traces obtained from the well H2 display a flat zero-crossing, which makes the FPS repolarisation at zero-crossing hard to detect. The outlying FPD_{zero} from well H2 accounts for the large interquartile range reported. The comparison between simulated and experimental $FPDc_{\text{zero}}$ values, presented in Figure 5.15, follows the same pattern present in Figure 5.14. Overall, Fridericia's correction does not affect the promixity of simulated and experimental results.

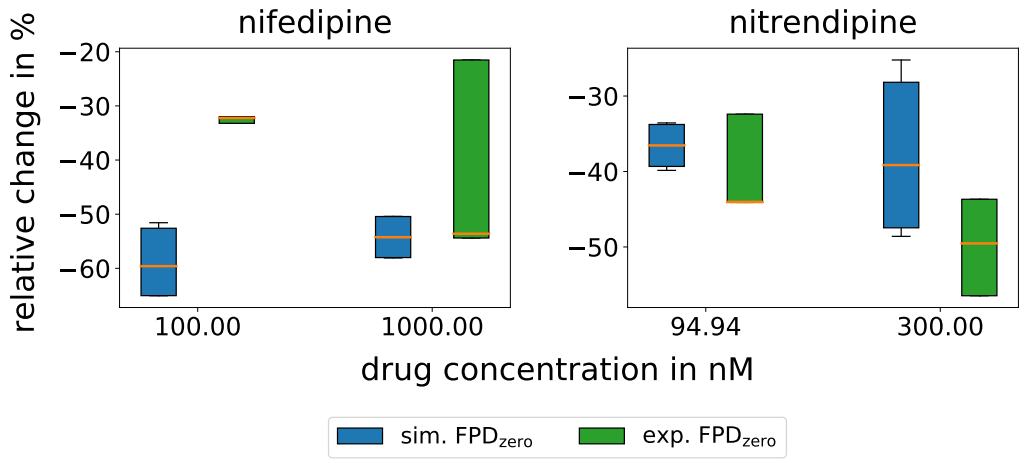


Figure 5.14: Change in FPD_{zero} caused by the addition of nifedipine or nitrendipine. The change is computed relative to the control case (no drug). Simulated as well as experimental results are presented. The abbreviation "sim." stands for simulated, and the abbreviation "exp." stands for experimental. In the simulated and experimental cases, we possess several values for each concentration of a drug. With simulations, different values are obtained from 10 different realisations of the Gaussian random field. With experiments, different values are obtained from experimental repeats. We present the variability across values with a boxplot. The median is marked by an orange line. The box indicates the interquartile range and the whiskers the 15th-to-85th-percentile range. Outliers are omitted to allow for a clearer presentation. The simulated biomarkers were extracted from simulated traces between 2000 s and 2006 s, as justified in Section 4.5.3. The full biomarker data were uploaded to an online repository and are available upon request. The size of these data prohibited us from including them in this thesis.

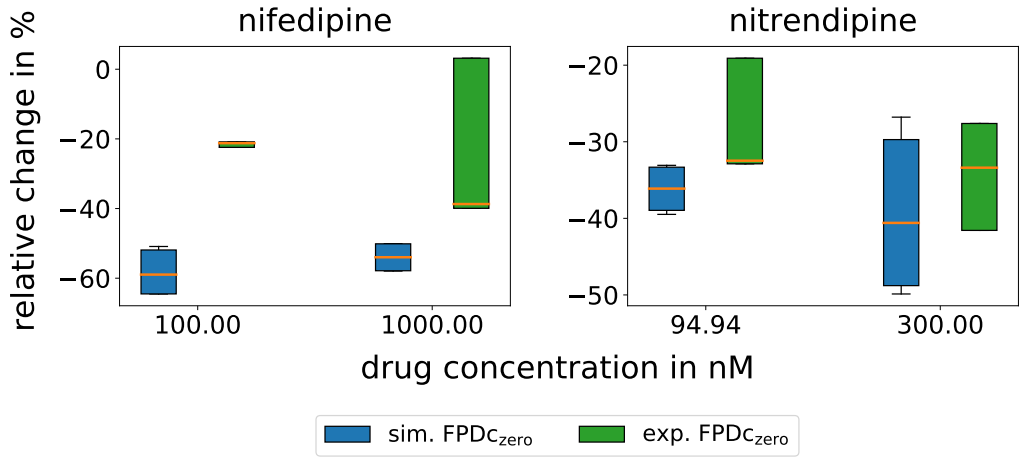


Figure 5.15: Change in $FPDc_{\text{zero}}$ caused by the addition of nifedipine or nitrendipine. Details are as for Figure 5.14.

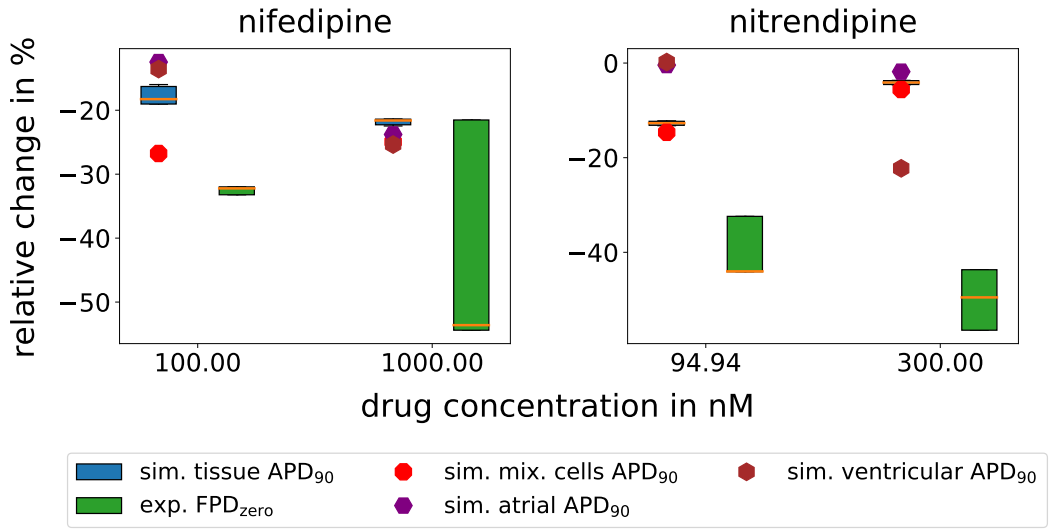


Figure 5.16: Change in simulated APD_{90} and experimental FPD_{zero} caused by the addition of nifedipine or nitrendipine. The simulated tissue APD_{90} is computed on $\overline{V_{\text{m}}}^{\text{rec}}$. The abbreviation "mix." stands for mixed. The atrial, ventricular and mixed cells APD_{90} are computed using the homogenised Paci2013 model (see Section 3.1.3 and **??** for more information). The atrial APD_{90} is computed with $\rho_{\text{V}} = 0$, the ventricular APD_{90} with $\rho_{\text{V}} = 1$, and the mixed cells APD_{90} with $\rho_{\text{V}} = 0.54$. Biomarker values are extracted at steady state.

Figure 5.16 presents the results from the comparison between simulated APD_{90} and experimental FPD_{zero}. We have included the simulated APD_{90} obtained from tissue simulations as well as cellular simulations. The simulated tissue APD_{90} displays the expected decrease in FPD_{zero} as the concentration of nifedipine is increased, but not when the concentration of nitrendipine is increased. This appears to be due to the behaviour of the mixed cell phenotype, as only the mixed cell APD_{90} increases with increased nitrendipine concentration. Deficiencies in the I_{CaL} description within the cellular model may explain the incorrect behaviour, as previously discussed in Section 5.2.1. In opposition to the mixed cellular APD_{90}, the atrial APD_{90} and the ventricular APD_{90} both decrease with increased concentration. Similar simulated cellular behaviour can be observed for nifedipine. The variation of APD_{90} with respect to the phenotype chosen were previously explored in Section 5.3.

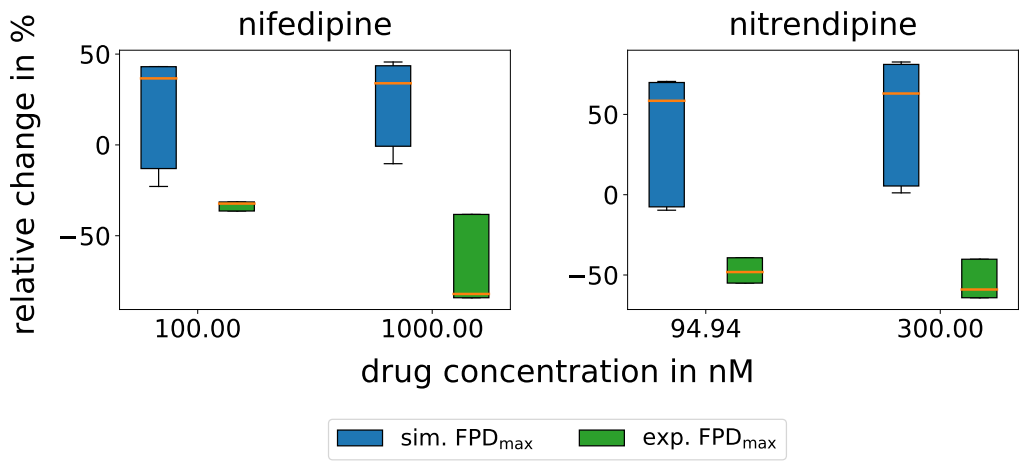


Figure 5.17: Change in $FPD_{\max}$ caused by the addition of nifedipine or nitrendipine. Details are as for Figure 5.14.

In Figure 5.17, we show the comparison between the simulated $FPD_{\max}$ and the experimental $FPD_{\max}$. While the experimental $FPD_{\max}$ decreases with increases in drug concentration, the simulated $FPD_{\max}$ does not. This discrepancy between simulated and experimental results is likely a consequence of model error and the repolarisation wave inversion, as discussed in Section 5.2.

5.4.2 I_{Kr} blockers

We continue the *in silico-in vitro* comparison with two I_{Kr} blocking drugs, droperidol and domperidone. Figure 5.18 presents the comparison for FPD_{zero}. The expected relative increase in FPD_{zero} when one of these drugs is added (see Section 2.1.1) can be observed for both concentrations of droperidol in the simulated cases, and for the lower concentration in the experimental case. For the higher concentration, no values are given because experimental traces are unreliable (as previously defined). Although the simulation correctly predicts an increase in FPD_{zero} at the lower concentration, the model overpredicts its value. This is particularly clear for domperidone at concentration 300 nM where the model predicts a two-fold increase but the exper-

iments exhibit a modest 10% increase. In Figure 5.19, we display the comparison for $FPDc_{\text{zero}}$. We observe similar patterns as in Figure 5.18. The difference is that the correction for beat duration brings simulated and experimental values closer.

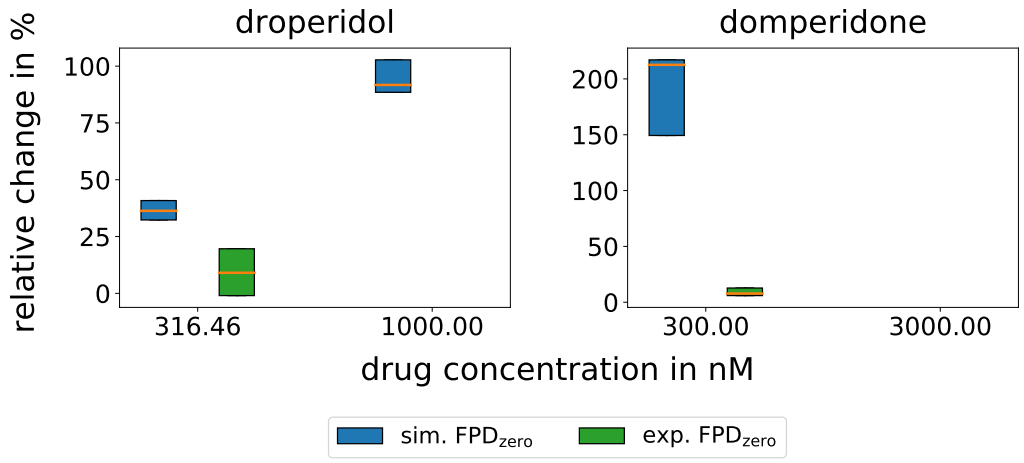


Figure 5.18: Change in FPD_{zero} caused by the addition of droperidol or domperidone. Details are as for Figure 5.14.

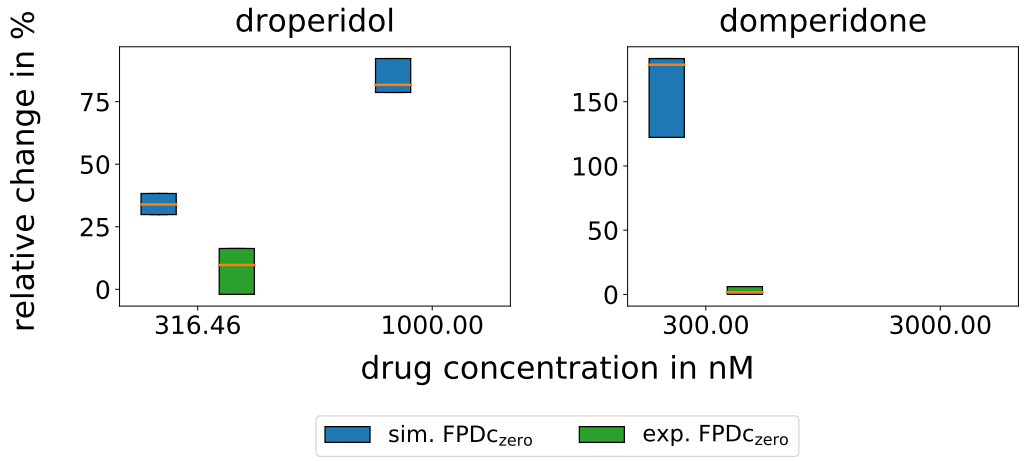


Figure 5.19: Change in $FPDc_{\text{zero}}$ caused by the addition of droperidol or domperidone. Details are as for Figure 5.14.

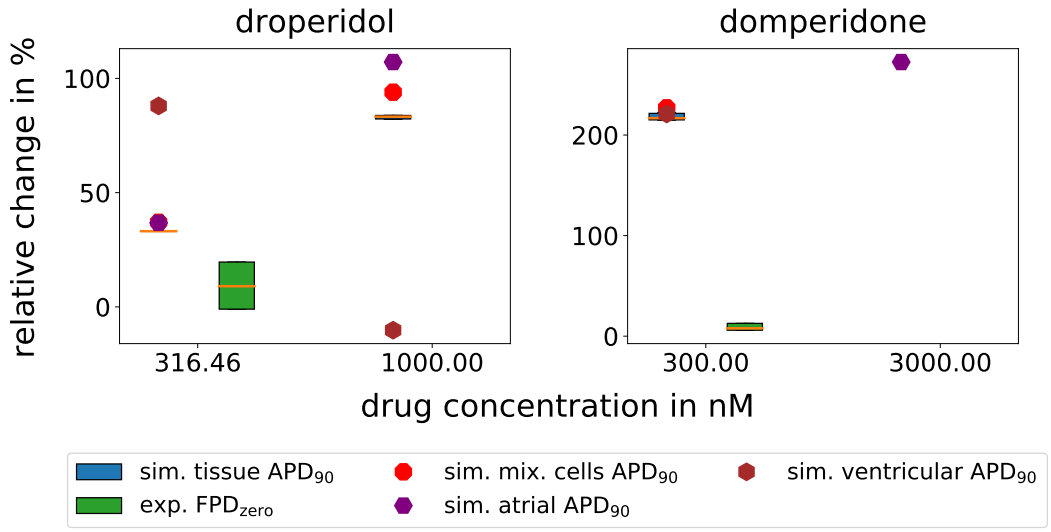


Figure 5.20: Change in simulated APD_{90} and experimental FPD_{zero} caused by the addition of droperidol or domperidone. Details are as for Figure 5.16.

Figure 5.20 presents the comparison between simulated APD_{90} and experimental FPD_{zero}. As previously, both tissue simulations and experiments correctly predict an increase in time to repolarisation. However, the model again overpredicts the time to repolarisation. This time the overprediction was obtained with APD_{90}, as opposed to FPD_{zero}. This repeated observation suggests that the oversensitivity to hERG block is a feature of the model rather than that of a particular time-to-repolarisation biomarker.

We now focus our attention to the predictions obtained with the cellular models. For droperidol, the mixed and atrial cellular APD_{90} closely track the tissue APD_{90}. Therefore, the mixed and AL cellular models also display an oversensitivity to hERG block. This observation allows us to specify what part of the mathematical model is oversensitive to hERG block. It indicates that the oversensitivity to hERG block is a feature of the *cellular* model rather than the *tissue* model.

The ventricular cellular APD_{90} stands out by decreasing as the concentration of droperidol increases. This unexpected behaviour was discussed in Section 5.3. For domperidone, the ventricular and mixed APD_{90} are close to the tissue APD_{90} at the

lower concentration. The atrial APD_{90} is only defined at the higher concentration. No beat can be registered in the AL simulation at the lower concentration. This is surprising as the toxicity of a drug is usually assumed to increase with dosage. Here, the AL simulation predicts that the beat is only conserved at the higher concentration of the drug. Having said this, this observation may be explained by the fact that at this concentration, the I_{CaL} blocking effects of domperidone may be sufficiently strong to partially compensate the I_{Kr} blocking effects of domperidone in the AL simulation.

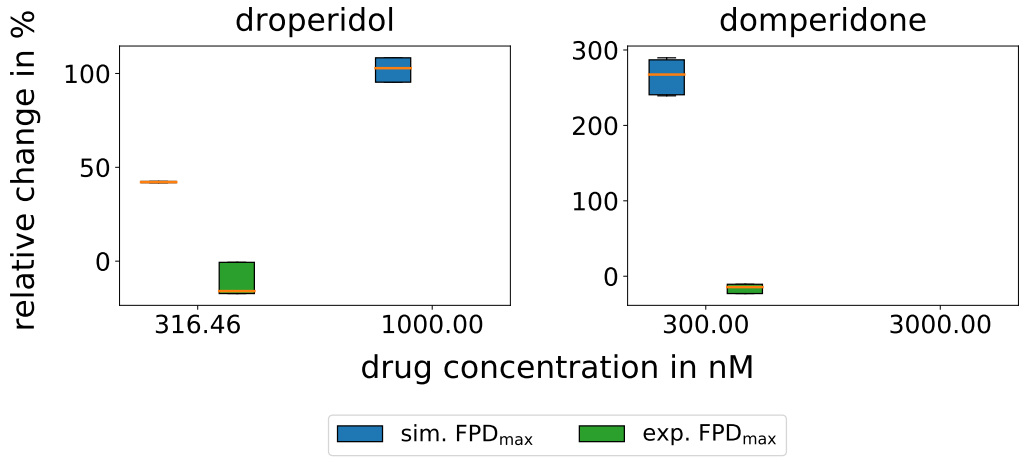


Figure 5.21: Change in FPD_{max} caused by the addition of droperidol or domperidone. Details are as for Figure 5.14.

Figure 5.21 summarises the *in silico-in vitro* comparison with FPD_{max}. Large increases in simulated FPD_{max} can be observed, but a small decrease in experimental FPD_{max} is observed at the lowest concentration. This decrease can be explained by the difficulty to correctly detect the FPS repolarisation at maximum, which we already highlighted in Section 5.2. The FPS repolarisation-at-maximum detection algorithm is very sensitive to small changes in the FPS. It may be that in some of the droperidol and domperidone experimental traces we misdetected an early peak for the repolarisation wave, when the real repolarisation wave was inverted. For example, we assessed on one beat the consequence of detecting an inverted repolarisation wave in well C7 for domperidone, instead of the earlier repolarisation wave we detected before.

A 24% increase in FPD_{max} at 300 nM can be observed, in line with the experimental FPD_{zero} presented in Figure 5.18. This contrasts with an 11% decrease in FPD_{max} obtained for the same beat with the method detecting the earlier repolarisation wave. This drastic change confirms that the strong sensitivity of the FPD_{max} biomarker to the FPS waveform is a drawback for its use in the case of I_{Kr} blockers here.

5.4.3 I_{CaL} and I_{Kr} balanced blockers

The next class of drug we studied is the I_{CaL} and I_{Kr} balanced blockers. These drugs have the property that they block I_{CaL} and I_{Kr} in similar proportions. Since I_{CaL} and I_{Kr} have opposite effects on the time to repolarisation (see Section 2.1.1), we expect drugs in this class to have a small net effect on time to repolarisation. The name "balanced blockers" originates from this observation. Here, we study two balanced blockers: pimozide and terfenadine.

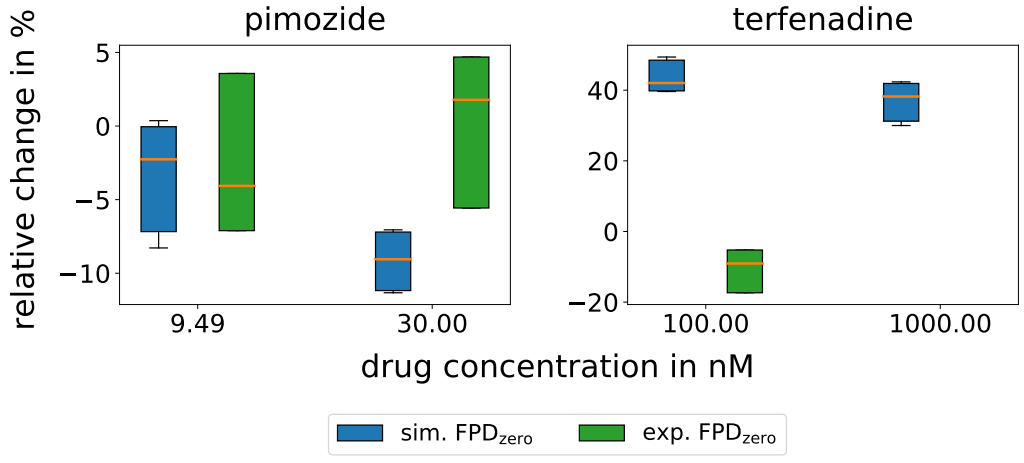


Figure 5.22: Change in FPD_{zero} caused by the addition of pimozide or terfenadine. Details are as for Figure 5.14.

Figure 5.22 shows the impact of the addition of pimozide and terfenadine on FPD_{zero}. We observe that both the simulated and experimental FPD_{zero} display small changes for pimozide, as we expected. However, for terfenadine large changes

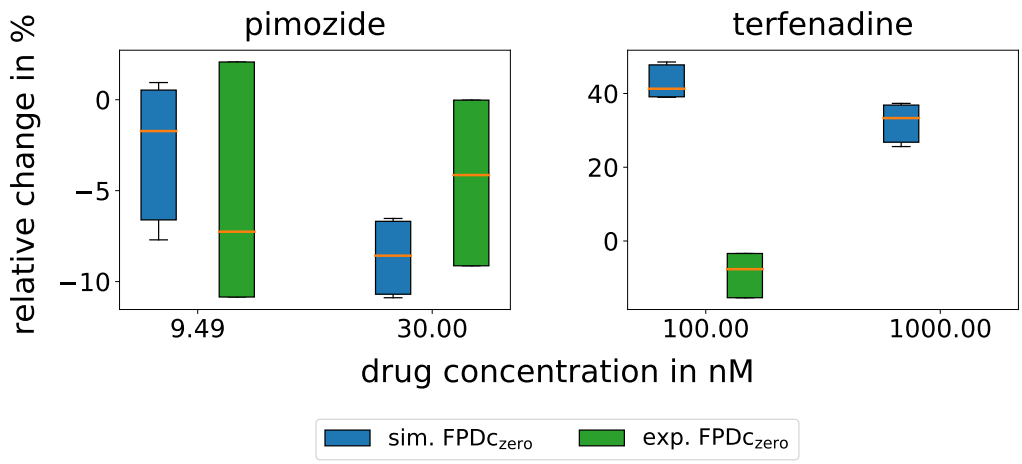


Figure 5.23: Change in $FPDc_{\text{zero}}$ caused by the addition of pimozide or terfenadine. Details are as for Figure 5.14.

in simulated FPD_{zero} can be observed. In particular, the large change in simulated FPD_{zero} observed at the drug concentration 100 nM contrasts with the smaller change in experimental FPD_{zero} for the same concentration. The reason why large changes in simulated FPD_{zero} occur with terfenadine but not with pimozide is that terfenadine is slightly more I_{Kr} blocking, relative to I_{CaL}, than pimozide. This slight change is, however, overamplified by the model because of its oversensitivity to hERG block. At concentration 1000 nM, terfenadine causes a cessation of the beat in experimental traces, but not in simulated traces. The experimental quiescence, observed in other studies of terfenadine [49], may be due to the I_{CaL} blocking effects of terfenadine. These effects may not be well-captured by the model because of its deficiencies in the description of I_{CaL}. The comparison of the effects of pimozide and terfenadine on $FPDc_{\text{zero}}$ is given in Figure 5.23. The same comments made for the FPD_{zero} comparison apply.

We study the differences between simulated APD_{90} and experimental FPD_{zero} in Figure 5.24. The tissue, mixed cellular and atrial simulated APD_{90} display small changes for the two drug concentrations of pimozide. These small changes are in line with the experimental FPD_{zero}. By contrast, the ventricular simulated APD_{90} pre-

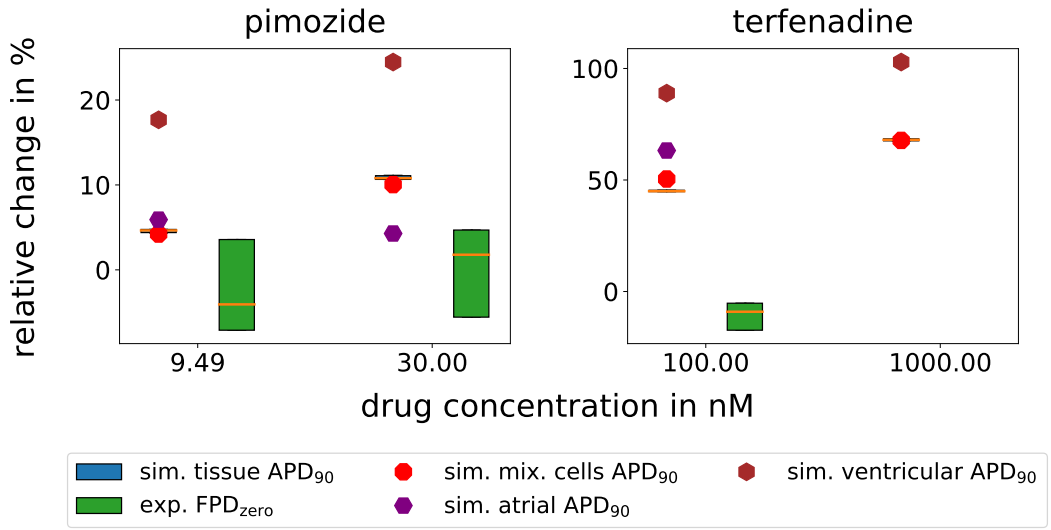


Figure 5.24: Change in simulated APD_{90} and experimental FPD_{zero} caused by the addition of pimozide or terfenadine. Details are as for Figure 5.16.

dicts higher changes. This comparison highlights that the VL model predictions differ from experimental observations for pimozide. For terfenadine, the simulated APD_{90} overpredicts the observed changes, like the simulated FPD_{zero} discussed before. The oversensitivity of the model to hERG block is again the cause of the overprediction. We notice that the AL model reproduces the experimentally observed cessation of the beat at the higher concenetration of terfenadine. This observation strengthens our confidence in the capacity of the AL model to recapitulate experimental data.

The comparison between simulated and experimental FPD_{max} is shown in Figure 5.25. Similar remarks to those made for the FPD_{zero} comparison apply. The only substantial difference is the large interquartile range presented by FPD_{max} at the higher concentration of pimozide. This can be explained by the unreliability of the detection of the FPS repolarisation at maximum, as previously highlighted in Section 5.2.

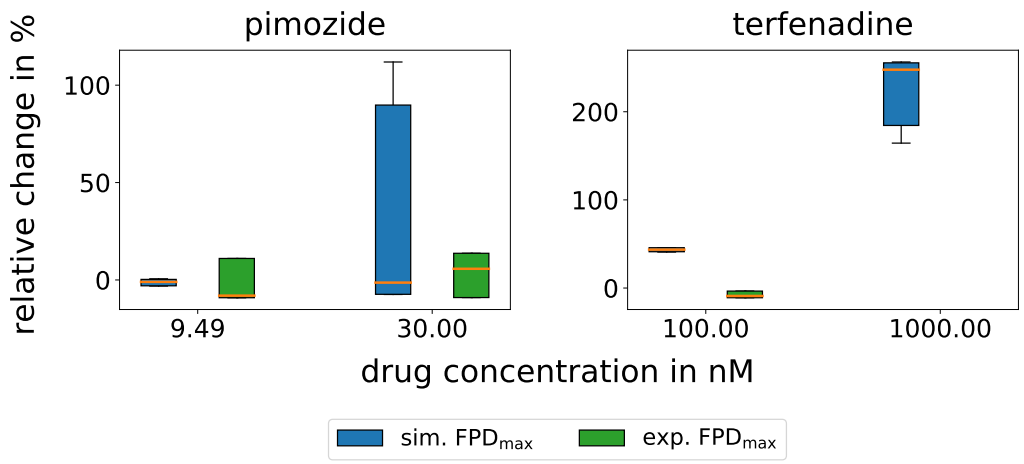


Figure 5.25: Change in FPD_{max} caused by the addition of pimozide or terfenadine. Details are as for Figure 5.14.

5.4.4 I_{Na} and I_{Kr} multiblockers

I_{Na} and I_{Kr} multiblocking drugs are the next class of drugs to be examined. Here, we study the two drugs disopyramide and dl-sotalol. Figure 5.26 presents the simulated-experimental FPD_{zero} comparison. The model oversensitivity to hERG block is again apparent in the disopyramide case. The oversensitivity explains the overprediction of the change in FPD_{zero} at the lower concentration, and the cessation of the beat displayed by the model at the higher concentration. The effect of dl-sotalol is particularly well captured by the model, as assessed with the FPD_{zero} biomarker. The accuracy of the model here may be due to the mild level of I_{Kr} block of dl-sotalol (see Table 5.2). At this mild level of I_{Kr} block, the model oversensitivity to I_{Kr} does not seem to impact on the FPD_{zero} prediction. Similar remarks can be made for the $FPDc_{\text{zero}}$ comparison. A notable difference is the absence of value for the experimental relative change in $FPDc_{\text{zero}}$ at the higher concentration of dl-sotalol. The reason for this absence is that no two consecutive spike troughs could be detected for an experimental trace of dl-sotalol. As a result no beat duration could be computed for this trace, and hence no $FPDc_{\text{zero}}$. The inability to compute $FPDc_{\text{zero}}$ for this

experimental trace made it so that more than 60% of experimental traces were excluded or without $FPDc_{\text{zero}}$ detection. In line with the rule given at the start of this section, this results in the experimental $FPDc_{\text{zero}}$ not being defined for the higher concentration of dl-sotalol.

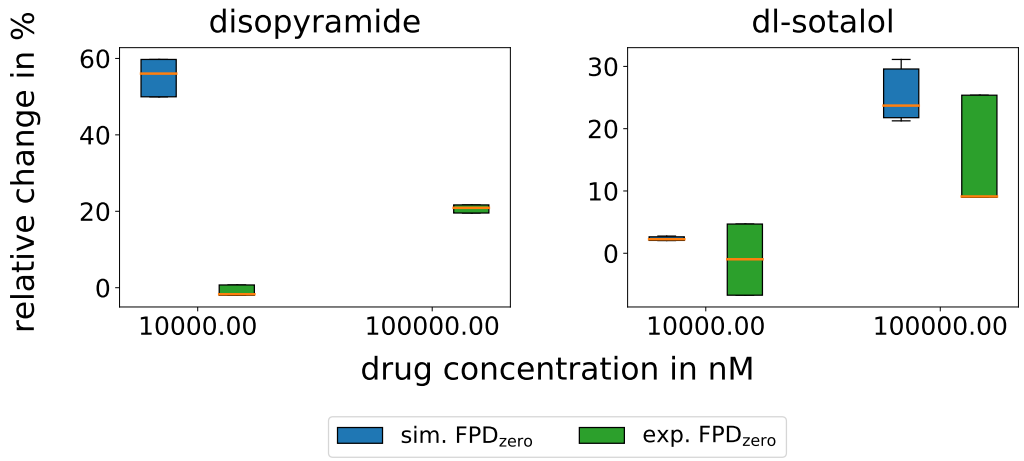


Figure 5.26: Change in FPD_{zero} caused by the addition of disopyramide or dl-sotalol. Details are as for Figure 5.14.

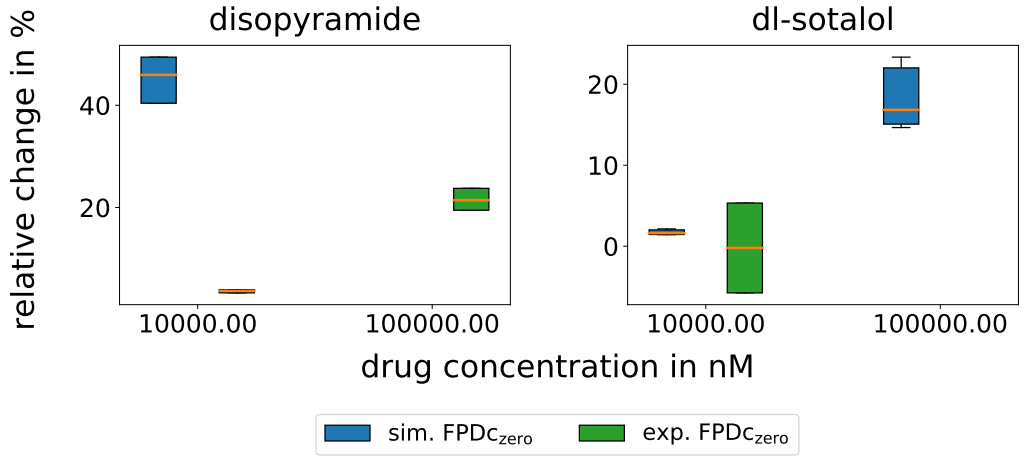


Figure 5.27: Change in $FPDc_{\text{zero}}$ caused by the addition of disopyramide or dl-sotalol. Details are as for Figure 5.14.

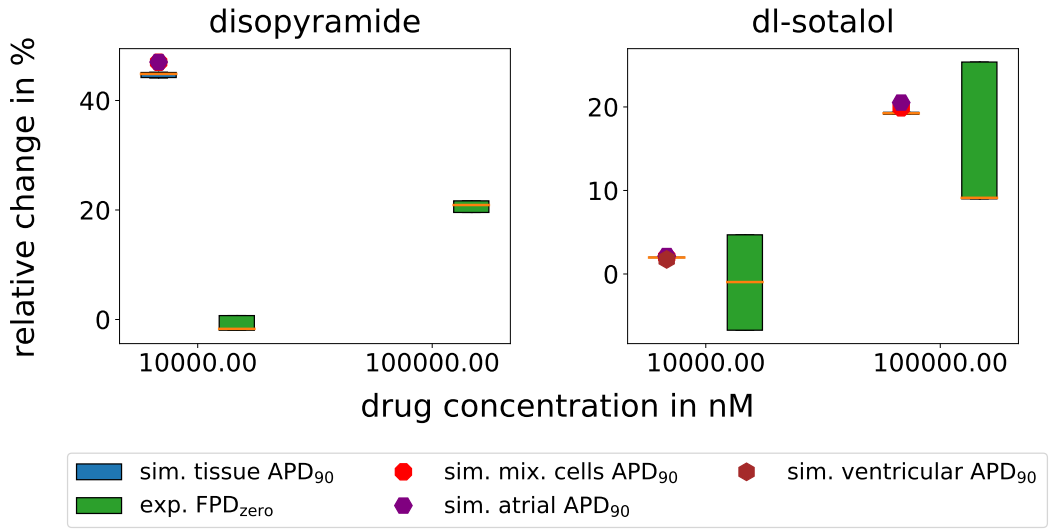


Figure 5.28: Change in simulated APD_{90} and experimental FPD_{zero} caused by the addition of disopyramide or dl-sotalol. Details are as for Figure 5.16.

In Figure 5.28, we present the comparison between simulated APD_{90} and experimental FPD_{zero} for disopyramide and dl-sotalol. Similar comments to those made for FPD_{zero} apply. We add that the oversensitivity of the cellular model to hERG block is manifest with the VL model. At both concentrations of disopyramide, and at the higher concentration of dl-sotalol, no beat can be seen in the VL simulation. Apart from the VL model behaviour, the cellular APD_{90} very closely track the tissue simulations in Figure 5.28.

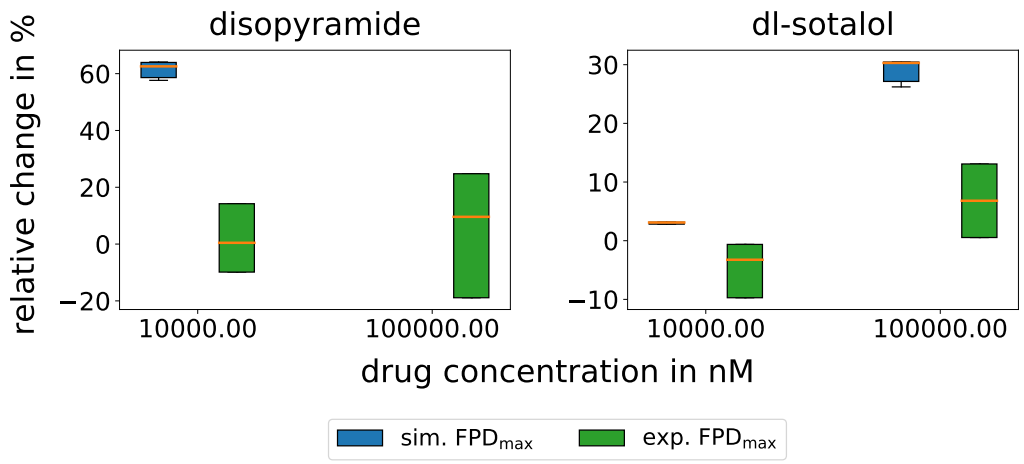


Figure 5.29: Change in FPD_{max} caused by the addition of disopyramide or dl-sotalol. Details are as for Figure 5.14.

Figure 5.29 displays the comparison of the impact of disopyramide and dl-sotalol on FPD_{max}. Similar remarks to those made previously for disopyramide and dl-sotalol apply here too. The *in silico-in vitro* agreement for dl-sotalol is however less close than with FPD_{zero}. This strengthens the hypothesis that FPD_{max} captures time to repolarisation less reliably than FPD_{zero}.

5.4.5 I_{Na}, I_{CaL} and I_{Kr} multiblockers

We finally present our simulated and experimental results for I_{Na}, I_{CaL} and I_{Kr} multiblocking drugs. There are four of these drugs in our dataset: quinidine, ranolazine, vandetanib and tamoxifen. For conciseness, only the results for quinidine and ranolazine are presented in the main text. The results for vandetanib and tamoxifen can be found in Section B.1.5.

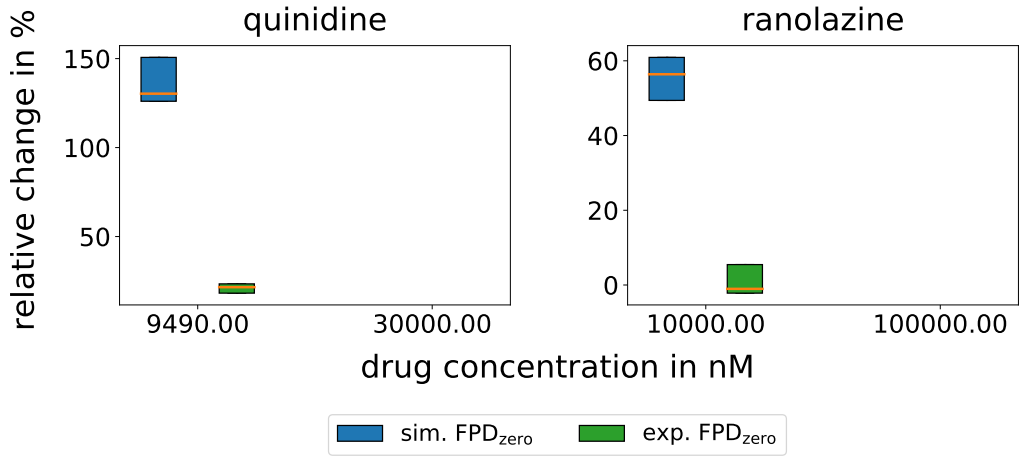


Figure 5.30: Change in FPD_{zero} caused by the addition of quinidine or ranolazine. Details are as for Figure 5.14.

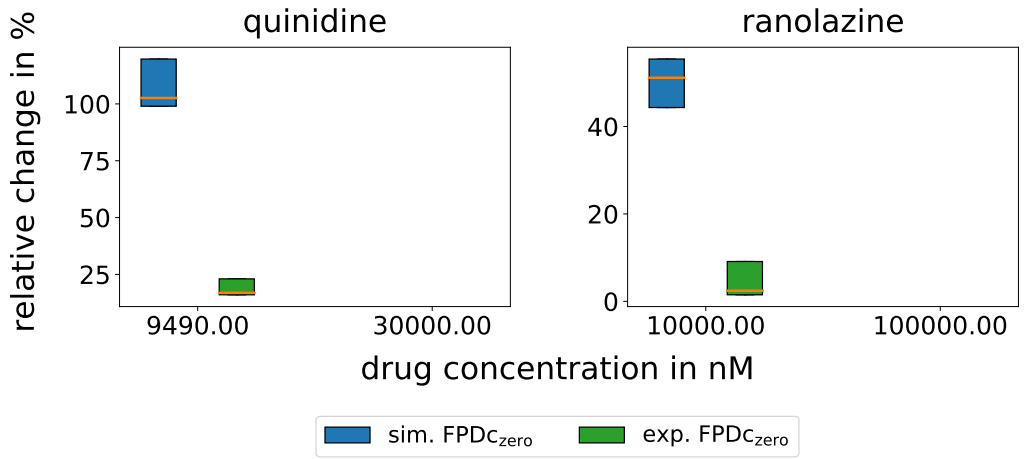


Figure 5.31: Change in $FPDc_{\text{zero}}$ caused by the addition of quinidine or ranolazine. Details are as for Figure 5.14.

Figure 5.30 presents the FPD_{zero} comparison for quinidine and ranolazine. We know from Table 5.2 that quinidine and ranolazine block I_{Kr} more than I_{CaL}. The experiments reflect this fact by showing increases in FPD_{zero} at the lower concentrations of the two drugs. The simulations also show increases, but they far exceed the experimental observations. This difference between experimental and simulated FPD_{zero} again highlights the model oversensitivity to hERG block. A positive point for the model is that the experimentally observed cessations of the beat for quinidine and ranolazine are reproduced in simulations. Figure 5.31 shows the comparison between simulated and experimental $FPDc_{\text{zero}}$ for quinidine and ranolazine. The only difference compared to Figure 5.30 is that the gap between experimental and simulated results has been reduced thanks to the correction for beat rate.

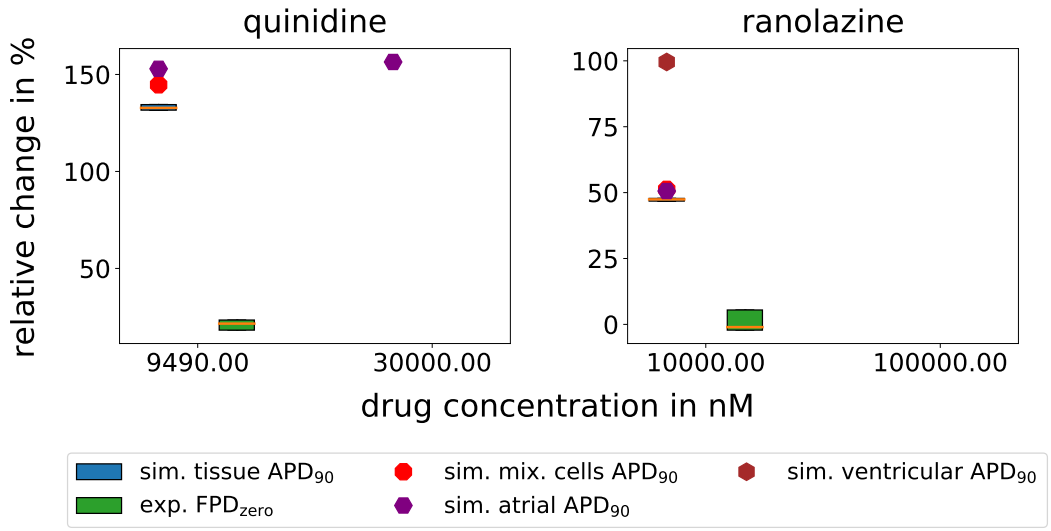


Figure 5.32: Change in simulated APD_{90} and experimental FPD_{zero} caused by the addition of quinidine or ranolazine. Details are as for Figure 5.16.

Figure 5.32 displays the comparison between simulated APD_{90} and experimental FPD_{zero} after the addition of quinidine, and ranolazine. The tissue and mixed cellular APD_{90} follow a similar pattern of time-to-repolarisation overprediction at the lower concentrations of the two drugs, and correct cessation of the beat prediction at the higher concentrations. The VL model again performs particularly poorly. It

wrongly predicts a cessation of the beat at the lower concentration of quinidine, and overpredicts the time to repolarisation even more than the tissue model at the lower concentration of ranolazine. The AL model performs similarly to the tissue model, with the exception of the higher concentration of quinidine. At this concentration, the AL model fails to capture cessation of the beat. Here, the large prediction failure of the VL model, and the more modest failure of the AL model, highlight the benefits of utilising the mixed cellular model for predicting time to repolarisation.

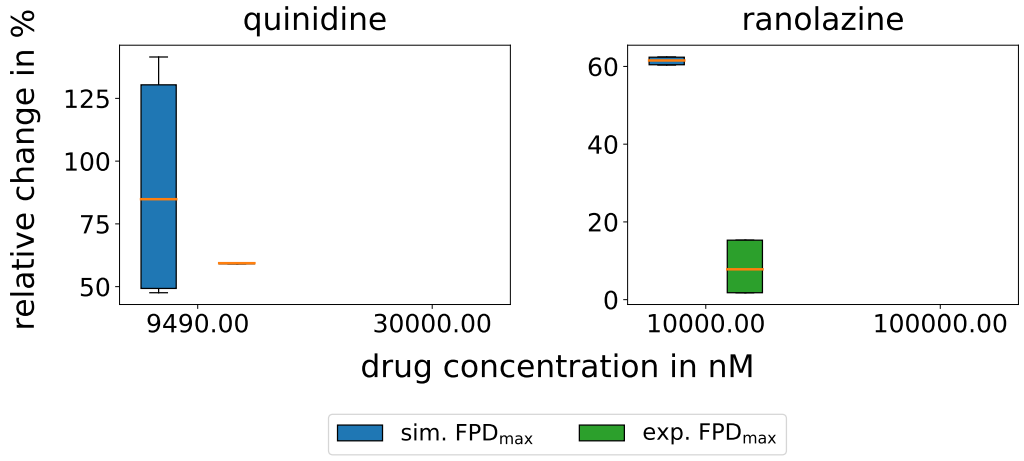


Figure 5.33: Change in $FPD_{\max}$ caused by the addition of quinidine or ranolazine. Details are as for Figure 5.14.

In Figure 5.33, we present the impact of the addition of quinidine or ranolazine on $FPD_{\max}$. The large uncertainty exhibited by the simulated $FPD_{\max}$ is a consequence of the difficulty to correctly detect the FPS repolarisation at maximum. With both drugs, the model overpredicts the change in $FPD_{\max}$, as compared with experiments. As already mentioned, this overprediction is explained by the oversensitivity of the model to hERG block. In the case of ranolazine, an additional factor adds to the explanation. Ranolazine blocks the late sodium current, which is not included in the model. This blockage contributes to the shorter $FPD_{\max}$ in experiments as compared to simulations.

5.5 Discussion

In this chapter, we have investigated the effect of 12 drugs on hECT through an *in silico-in vitro* study. Time-to-repolarisation summary statistics were used to assess those effects. After interrogating the validity of the summary statistics, we conducted a thorough investigation of their changes as drugs were added to the hiPSC-CM monolayers. Simulated and experimental changes were compared to estimate the accuracy of the predictions of the theoretical model.

The *in silico-in vitro* comparison presented in this chapter showcased numerous deficiencies in the theoretical model and summary statistics. The first theoretical model deficiency is its oversensitivity to hERG block. We have noted in Section 5.4 that this deficiency originates from the cellular model. This oversensitivity has already been noted by Bowler (2018) [25]. The simplest potential solution would be to modify the conductance of I_{Kr} with the aim to reduce the time-to-repolarisation change when an I_{Kr} blocking perturbation is performed. Should this solution fail, structural changes to the formulation of the I_{Kr} model may be needed.

The second theoretical model deficiency is the inaccuracy of the calcium dynamics formulation in the cellular model. The consequences of this inaccuracy could be observed in the simulations we conducted to assess the impact of I_{CaL} blocking drugs. The inaccuracy has previously been noted by Paci *et al.* (2018) [19] and Koivumäki *et al.* (2018) [70]. An alternative formulation of the Ca^{2+} release from the sarcoplasmic reticulum was presented to correct for the problem [19, 70]. However, only a VL hiPSC-CM model with corrected Ca^{2+} dynamics is available. A corrected AL hiPSC-CM model is still to be developed.

The third theoretical model deficiency is the unreliability of the FPS generated. We emphasised in Section 5.2 that the imprecise calibration of the I_{NaCa}, I_{NaK}, I_{pCa}, I_{bNa}, I_{bCa} current parameters was an issue for the reliability of the simulated FPS. In addition, we noted that the time-to-repolarisation biomarker extracted from $\overline{V_{\mathrm{m}}}^{\mathrm{rec}}$

coincides with a consistent ionic feature (e.g. the end of I_{Ks}, as noted in Section 5.2) while time-to-repolarisation biomarkers extracted from the FPS do not. Further work should be conducted to calibrate I_{NaCa}, I_{NaK}, I_{pCa}, I_{bNa} and I_{bCa} to improve the generalisability of the model to the prediction of the FPS. If experimental data are not available for this calibration, an alternative would be to optimise the I_{NaCa}, I_{NaK}, I_{pCa}, I_{bNa}, I_{bCa} current parameters to reproduce the experimentally observed FPS.

A fourth theoretical model deficiency originates from the fact that we did not calibrate the bidomain parameters χ, $\mathbf{\Sigma}_{\mathrm{e}}$ and C_{m}. We chose to continue the study of drug effects on hECT initiated by Bowler (2018) [25]. We kept the χ, $\mathbf{\Sigma}_{\mathrm{e}}$ and C_{m} parameters used by Bowler, which model a tissue composed of adult CMs. The parameters for a tissue made of hiPSC-CMs may be different. Hwang *et al.* (2015) [103] reported a value of χ approximately equal to $4000\,\mathrm{cm}^{-1}$ in their study of hiPSC-CMs. This value is three times higher than that used in this study ($1400\,\mathrm{cm}^{-1}$). Having considered this result, the cell lines used in [103] are different from that used in our experimental data (iCell Cardiomyocytes, version two). In our study, we were careful to have the parameter values of our models originate from experimental studies of the same hiPSC-CM cell line as that used in our experiments. Different hiPSC-CM cell lines can display large differences in their electrophysiology [26]. For example, the value of σ_i used in our study ($0.3\,\mathrm{mS\,cm}^{-1}$), derived experimentally from an iCell hiPSC-CM monolayer, is more than an order of magnitude higher than that reported [22] for a Cor.4U hiPSC-CM monolayer ($0.01\,\mathrm{mS\,cm}^{-1}$). Future work may aim to quantify the sensitivity of the FPS to the bidomain parameters. The most sensitive parameters could be considered for experimental measurement in the iCell Cardiomyocyte cell line (ideally, with iCell Cardiomyocytes version two).

A final deficiency of the *in silico* prediction of drug effects with hECT is the lack of robustness of tissue time-to-repolarisation biomarkers. The tissue time-to-repolarisation biomarkers FPD_{zero} and FPD_{max} did not qualitatively match the gold

standard tissue APD_{90} biomarker for all the drugs considered in Section 5.2. This difference is partly explained by the unreliabilty of the simulated FPS, but also by the inability of the biomarkers to consistently capture the same ionic current features in the FPS. The unreliability of FPD_{max} was particularly apparent in Section 5.2 and Section 5.4. We recommend using FPD_{zero} instead of FPD_{max} to capture time to repolarisation in tissue, as originally proposed by Obergrussberger *et al.* [87]. Future work could attempt to use machine learning algorithms to learn complex features of the FPS that are more robust to drug perturbation than FPD_{zero}.

Chapter 6

Conclusion and future work

In this thesis, we have conducted the first *in silico-in vitro* study that evaluates the impact of a large number of drugs on the FPS. This study is also the first to have simulated the FPS experimentally measured by the CardioExcyte96 recording device. In Section 6.1 we summarise our methodology and findings, and we draw conclusions. In Section 6.2 we identify directions for future research.

6.1 Summary and conclusions

In Chapter 4, we introduced our *in silico-in vitro* methodology. We presented the experimental set-up that we mathematically modelled to conduct our *in silico* work. This experimental set-up had particularities that we accounted for in our modelling approach. The theoretical model was solved numerically with a simulation framework that we verified through a convergence analysis. The simulation of the theoretical model provided simulated results that we could compare to the experimental results. This comparison was enabled by the developement of a novel signal processing pipeline to extract summary statistics from simulated and experimental data. The

uncertainty in these summary statistics, introduced by numerical approximations to the solution of the model, was quantified. In particular, we determined that the model needed to be simulated for about 33 min to obtain sufficiently accurate estimates of summary statistics of interest (FPD_{zero}, FPD_{max}, APD_{90}, *beat rate*). To determine this minimal simulation time, we examined the time course of the summary statistics over a long duration (2 h45 min). The time course allowed us to quantify the error incurred by extracting the summary statistics before the steady-state had been reached. This quantification complements the pioneering work of Bowler (2018) [25], in which summary statistics were extracted after 10 s of simulation.

In Chapter 5, we utilised the *in silico-in vitro* methodology presented in Chapter 4 to gain insight into the effect of 12 drugs on the FPS. We layed the foundations for our work by characterising features of the FPS by comparison with the average of the membrane potential over the recording electrode ($\overline{V_{\text{m}}}^{\text{rec}}$). This characterisation allowed us to investigate the validity of the FPS biomarkers FPD_{zero} and FPD_{max} for capturing time to repolarisation. As we conducted simulations of hECT, we made the observation that a key parameter determining time to repolarisation was the phenotype of the cells studied. We developed this observation further by quantifying the impact of this parameter on time to repolarisation, in the presence of four different drugs. The work on the validity of time to repolarisation biomarkers as well as their sensitivity to phenotype variations helped us hypothesise mechanisms for the results we presented next. We presented the experimental and simulated effects of 12 drugs on time to repolarisation biomarkers. This presentation gave us insight into the predictive capability, as well as the limitations, of the theoretical model.

In Chapter 5, we had the opportunity to investigate a weakness of the *in silico* step of the CiPA initiative that we had outlined in Chapter 1. The CiPA *in silico* step consists in comparing a single simulated ventricular adult CM to a mixed *in vitro* AL and VL hiPSC-CM tissue. In Chapter 1, we emphasised that the dif-

ferences of maturity, phenotype and spatial scale between the *in silico* and *in vitro* assays challenged the validity of the comparison. In Chapter 5, we tested whether the *in silico-in vitro* comparison was sensitive to differences in phenotype and spatial scale between simulations and experiments. To do this, we compared the time-to-repolarisation biomarkers obtained from the simulation of a VL hiPSC-CM with the time-to-repolarisation biomarkers obtained from hECT experiments. We found that the simulation of a VL hiPSC-CM was least indicative of the experimental behaviour. Specifically, we showed that the time-to-repolarisation biomarkers APD_{90} and $APDc_{90}$ extracted from the VL $V_{\mathrm{m,cell}}$ trace yielded the worst prediction of experimental time to repolarisation. We observed that better *in silico-in vitro* agreement was obtained with a tissue simulation, a mixed cellular simulation, or an AL cellular simulation (in order of accuracy, from best to worst).

6.2 Future work

In this work, we faced a major difficulty in conducting the *in silico* study of the effect of drugs on hECT. The difficulty was that the computation of the solution of the mathematical model was very expensive. To reduce this computational cost, we performed the simulations on a very coarse mesh ($h = 750\,\mu\mathrm{m}$). We have shown in Section 4.5.1 that in spite of the coarseness of the mesh, the values of FPS summary statistics obtained are similar to those obtained with a fine mesh. We have verified the correct implementation of simulations through a convergence analysis. The convergence analysis conducted in this thesis, described in Section 4.3.2, was performed with a simplified model and geometry. Specifically, the analysis was conducted on a square domain without a grounding electrode. A more comprehensive convergence analysis should be performed in future work to conclusively verify that simulations are implemented correctly. This convergence analysis should be performed with the model

and geometry of the experimental system studied in this thesis (see Section 4.2). In particular, the model should include a grounding electrode, and the domain should preferentially be a disc. This thorough convergence analysis would study the model and geometry simulated in Chapter 5 more faithfully than the simplified convergence analysis we conducted. This being said, previous verification of the Chaste solver [104], including with a closely related problem [25], along with the simplified convergence analysis presented in this thesis, are strong arguments in favour of the validity of the implementation of the simulations. We expect that the thorough convergence analysis that we recommend will confirm the correct implementation of simulations.

In this study, we successfully employed various methods to reduce the computational cost incurred to simulate the effects of drugs on hECT (see Section 4.5). In spite of this success, the computational cost of simulations remained high enough to substantially impede our progress. Future work should aim to reduce the computational cost further. Without this further reduction, we speculate that *in silico* drug testing studies at the scale of hECT will not be widely adopted as a standard part of the pre-clinical drug safety testing protocol. A promising path to reducing this computational cost was outlined by Matsuno *et al.* (2019) [105]. A machine learning model was developed to act as a surrogate for a computationally expensive, mechanistic tissue electrophysiological model similar to the model used in this study. The surrogate model, fast to simulate, was used with success to predict the effects of four drugs on the QT interval. Future work could follow a similar approach to allow for the reduction of the computational cost of the simulation of hECT presented in this work.

In Section 5.5, we called attention to the weaknesses of the theoretical electrophysiological model and the summary statistics. Briefly, the first two weaknesses we noted were the oversensitivity of the cellular model to hERG block and the inaccuracy of the I_{CaL} current in the cellular model. The lack of reliability of the cellular model

to produce a realistic FPS (derived from cellular simulations via the bidomain model) is the third weakness we mentioned. The fourth weakness is our lack of calibration of the bidomain parameters. In this work, we continued the study of Bowler (2018) [25] and kept the same bidomain parameter values. The final weakness we highlighted is the lack of robustness of tissue time-to-repolarisation biomarkers to drug perturbations. We offered solutions to overcome these weaknesses. Briefly, these solutions are changing the formulation of I_{Kr} in the cellular model, developing an AL hiPSC-CM model, and individually calibrating the I_{NaCa}, I_{NaK}, I_{pCa}, I_{bNa} and I_{bCa} current parameters. In addition, the bidomain parameters should be measured experimentally with the iCell Cardiomyocyte cell line, and machine learning algorithms should be considered for learning features of the FPS that are robust to drug perturbation. We recommend implementing the solutions before utilising the electrophysiological model further. Once the solutions are implemented, the hiPSC-CM cell and tissue models could be shown to prevail over the CiPA adult ventricular cell model [106] for predicting experimental hECT behaviour *in silico*. The *in silico* prediction of experimental hECT behaviour would complement the current CiPA protocol. As previously discussed in Chapter 1, it could save time and expense, in addition to providing a mechanistic understanding of hECT behaviour. This understanding would help delineate the benefits and limitations of the hECT experimental model for predicting drug-induced arrhythmia in humans.

Another avenue for future research is to focus on the electromechanical behaviour of hECT, instead of solely on its electrophysiology. Ultimately, patients are affected by a cardiotoxic drug if it alters the contractility of their hearts. However, the effect of drugs on the contractility of the hiPSC-CM monolayer is not directly assessed either *in vitro* or *in silico* in the CiPA initiative [107]. Such assessment has the potential to complement the results of the electrophysiological studies conducted as part of CiPA. It is unclear whether *contractile cardiotoxicity* can be always be de-

tected from an electrophysiological cardiotoxicity assessment, for example for kinase-targeted cancer drugs [108, 109]. Drugs causing morphological damage or loss of subcellular components in CMs are responsible for structural, non-proarrythmic cardiotoxicity and may not be detected by electrophysiological micro electrode array (MEA) measurements [107], such as those studied in this thesis. Optical measurements following fluorescently-labeled calcium ions or myofibrils have been used in addition to impedance measurements to measure the effects of drugs on contractility more directly than MEA measurements. Impedance measurements were found to accurately predict tyrosine-kinase drug toxicity by Doherty *et al.* (2013) [110].

The CardioExcyte96 recording device, which produced the FPS experimental data used in this thesis, can also perform impedance measurements on the hECT. A combined study of the FPS and the impedance signal would provide insight into the electrophysiological and contractile effects of drugs. In this thesis, we have contributed the first part of this study by analysing the electrophysiological effects of 12 drugs. This work could be taken further by assessing the contractile effects of the drugs with the impedance signal. The combined study would allow us to build a more complete profile of the cardiotoxicity of a drug than that offered by the current CiPA initiative.

Appendix A

Supplementary information for Chapter 4

This appendix contains additional material relevant to the work covered in Chapter 4. A detailed description of the electrophysiological experiments that were conducted in Dr Liudmila Polonchuk's laboratory is provided in Section A.1[1] and detail about the method we developed for calculating the action potential duration at 90% repolarisation of hiPSC-CMs is provided in Section A.2.

A.1 Detailed description of the experiments

A.1.1 Sensor plate preparation and cell seeding

iCell Cardiomyocytes2 (Cellular Dynamics International, USA) used for the study were stored in liquid nitrogen until thawed and cultured according to manufacturer instructions on the CardioExcyte 96 sensor plates (NSP-96) with a 0.6 mm central (recording) electrode. The NSP-96 wells were coated with 10 µg/ml fibronectin (Sigma Aldrich, USA) in PBS (including Ca2+ and Mg2+; Thermofisher/Gibco 14040 – 083

[1]This description was written by Dr Liudmila Polonchuk and further edited by the author.

DPBS) for 2 hours at 37°C. The fibronectin was removed shortly before cell seeding. After the cells were seeded, the NSP-96 was left in the sterile cabinet to allow the cells to settle evenly. Medium exchange was performed according to the supplier recommendations. After 10 days in culture cells were treated with test compounds. Prior to dosing, all hiPSC-CM cells formed syncytial monolayers suitable for electrophysiological assessments via extracellular field potential.

A.1.2 Chemical reagents and solutions

The CDI maintenance medium was obtained from the cell provider. On the day of compound applications, culture media was completely removed from the wells and fresh serum-free BMCC media (N-Cardia, Germany) was added to ensure an exact volume per well. Cells were allowed to re-equilibrate for 2-3 hours, and online parameters were monitored to ensure a stable baseline. Chemical reagents provided by the Chemotherapeutic Agents Repository of the National Cancer Institute. Chemical stock solutions at 1000-fold of the target concentrations were prepared under sterile conditions in DMSO and stored at -20°C, according to Myocyte Study instructions [95]. Compounds were dosed under sterile conditions in single point additions (i.e. one concentration per well) in up to five replicates for each dose, following the dilution scheme provided by the CiPA protocol. Vehicle control was 0.1% DMSO, and different doses of dofetilide were used among participating sites as positive control. After application of the compound, measurements of the FPS were taken every 15 min for 30 s for a period of 1 h.

A.1.3 Data acquisition and analysis

The CardioExcyte 96 device uses electrical measurements to study pharmacological effects on CM ion channel activity through FPS recordings. Field potentials were

recorded using the CardioExcyte Control software (Nanion Technologies, Germany). FPS data of spontaneous beating cells were collected at 0.1 ms (10 kHz). Data acquisition was controlled by the CardioExcyte 96 Control software which operates the CardioExcyte 96 hardware. The CardioExcyte 96 Control software is used to define the experimental setup such as timing of sweeps, sweep interval and online analysis parameters, for details see [85–87]. Briefly, a mean beat was generated by aligning individual beats and calculating mean beat and standard deviation. A selection of parameters including primary and secondary (corresponding to arrhythmic events) beat differentiation for FPS (spike amplitude, beat rate, beat rate covariance, $FPD_{\max}$, $FPDc_{\max}$) were automatically detected. Data was analysed using DataControl 96 (Nanion Technologies, Germany).

A.2 Methods for the calculation of APD_{90}

A.2.1 Calculation of the depolarisation time in the hiPSC-CM method

The depolarisation time of the ith action potential, $t_{\text{dep},i}$, is defined by Equation (4.12) for the hiPSC-CM method. The method for computing the inverval of times between which we look for $t_{\text{dep},i}$, $[t_{\text{start},i}, t_{\text{end},i}]$, is given here. It is sensible to define $[t_{\text{start},i}, t_{\text{end},i}]$ to be an interval around the ith action potential, for example as a sliding window whose length is that of a typical beat duration, 1 s, and that is shifted by 1 s for every next action potential, so that for any i

$$t_{\text{end},i} - t_{\text{start},i} = 1\,\text{s}, \tag{A.1}$$

$$[t_{\text{start},i+1}, t_{\text{end},i+1}] = [t_{\text{end},i}, t_{\text{end},i} + 1\,\text{s}]. \tag{A.2}$$

The initial values $[t_{\text{start},0}, t_{\text{end},0}]$ and the final values $[t_{\text{start,stop}}, t_{\text{end,stop}}]$, where stop is the index of the last action potential detected in V_{cell}, are suitably specified. For any i, we call the interval $[t_{\text{dep},i}, t_{\text{dep},i+1}]$ the ith *interstroke interval*.

A.2.2 Calculation of the repolarisation time in the hiPSC-CM method

For practical purposes, the end of the ith action potential can be defined as the time when the transmembrane potential is 90% repolarised, that we denote by $t_{\text{rep},i}$. The value of the transmembrane potential when it is 90% repolarised, or more generally p repolarised, where p is a percentage, is denoted by $\hat{V}_i(p)$ and is defined in the hiPSC-CM method by

$$\hat{V}_i(p) = V_{\text{rest},i} + (1-p)\left(V_{\text{peak},i} - V_{\text{rest},i}\right), \tag{A.3}$$

where we define the resting potential of the ith action potential, $V_{\text{rest},i}$, as the 3rd decile of the values of the cellular transmembrane potential in the ith interstroke interval (see Figure A.1 for a visualisation). Similarly, $V_{\text{peak},i}$ is defined as the maximum of the values of the cellular transmembrane potential in the ith interstroke interval. The repolarisation time, $t_{\text{rep},i}$, can now be defined to be the first time after $t_{\text{dep},i}$ when V_{cell} is equal to $\hat{V}_i(0.9)$.

A.2.3 Calculation of the action potential duration at 90% repolarisation in Chaste

In Chaste, the ith resting potential, $V_{\text{rest},i}^{\text{chaste}}$, is defined as the minimum of the values of $V_{\text{m,cell}}$ in the ith interstroke interval. The hiPSC-CM method defines $V_{\text{rest},i}$ differently,

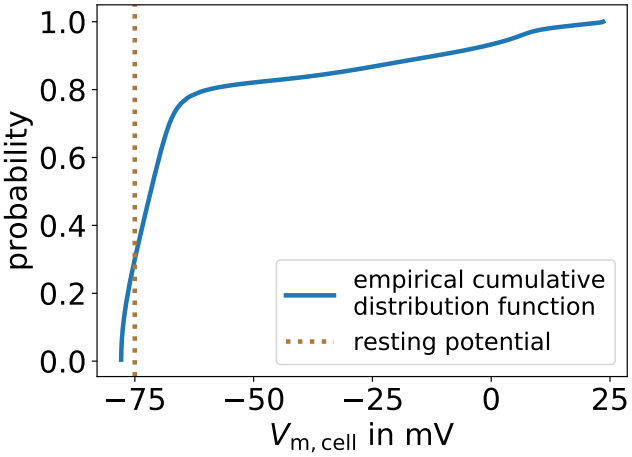


Figure A.1: Determination of the resting potential as defined in the hiPSC-CM method. In the hiPSC-CM method, the resting potential is defined as the 3rd decile of the distribution of the values of the cellular transmembrane potential in an interstroke interval, or *interstroke values* for short. The resting potential intersects with the empirical cumulative distribution function of interstroke values at probability 0.3, as expected from the definition of the resting potential. The particular values shown here come from the simulation of a VL-hiPSC-CM cell without drug. The cellular model used is the Paci2013 model.

as the 3rd decile of the values of V_{cell} in the ith interstroke interval, such that we have

$$V_{\mathrm{rest},i}^{\mathrm{chaste}} \leq V_{\mathrm{rest},i}. \tag{A.4}$$

The ith resting potential calculated by Chaste, $V_{\mathrm{peak},i}^{\mathrm{chaste}}$, is defined in the same way as that calculated in the hiPSC-CM method. It is defined as the maximum of the values of the cellular transmembrane potential in the ith interstroke interval. The definition by Chaste of the transmembrane potential at p repolarisation, $\hat{V}_i^{\mathrm{chaste}}(p)$, is the same as that defined by Equation (A.3), replacing $V_{\mathrm{rest},i}$ by $V_{\mathrm{rest},i}^{\mathrm{chaste}}$ and $V_{\mathrm{peak},i}$ by $V_{\mathrm{peak},i}^{\mathrm{chaste}}$. In particular, the value used by Chaste for the transmembrane potential at 90% repolarisation is denoted by $\hat{V}_i^{\mathrm{chaste}}(0.9)$.

An important consequence can be drawn from Equation (A.4) and from the manner in which $\hat{V}_i^{\mathrm{chaste}}(0.9)$ and $\hat{V}_i(0.9)$ are computed through Equation (A.3). This

consequence is that

$$\hat{V}_i^{\text{chaste}}(0.9) \leq \hat{V}_i(0.9). \tag{A.5}$$

Contrary to the hiPSC-CM method that only makes use of $\hat{V}_i(0.9)$ to define the repolarisation time of the ith action potential, $t_{\text{rep},i}$, Chaste makes use of $\hat{V}_i^{\text{chaste}}(0.9)$ to define both the depolarisation time, $t_{\text{dep},i}^{\text{chaste}}$, and the repolarisation time, $t_{\text{rep},i}^{\text{chaste}}$. Chaste defines $t_{\text{dep},i}^{\text{chaste}}$ to be the time when $V_{\text{m,cell}}$ crosses $\hat{V}_i^{\text{chaste}}(0.9)$ upwards, and $t_{\text{rep},i}^{\text{chaste}}$ to be the time $V_{\text{m,cell}}$ crosses $\hat{V}_i^{\text{chaste}}(0.9)$ downwards (see Figure 4.10a for an illustration). Given the shape of an action potential, an empirical consequence of this definition and of Equation (A.5) is that

$$t_{\text{dep},i}^{\text{chaste}} \leq t_{\text{dep},i}, \tag{A.6}$$

$$t_{\text{rep},i}^{\text{chaste}} \geq t_{\text{rep},i}. \tag{A.7}$$

Given the definition of the action potential duration at 90% repolarisation given by Equation (4.13), a consequence of Equation (A.6) and Equation (A.7) is that

$$APD_{90}^{\text{chaste}}\big|_i \geq APD_{90}\big|_i \,. \tag{A.8}$$

Practically, $APD_{90}^{\text{chaste}}\big|_i$ constitutes an overprediction of the action potential duration for hiPSC-CMs. This overprediction can be observed in Figure 4.10a. On the contrary, $APD_{90}\big|_i$ is a better approximation, as shown in Figure 4.10b.

A.3 Uncertainty quantification: resolution

The computation savings obtained with the coarse spatial resolution 750 µm is presented in Table A.1. We observe that vast computation savings, both in terms of time and number of computation cores, can be achieved by choosing a coarser mesh.

h	# cores	computation time
50 µm	20	18 043.8 s ≈ 5 h
750 µm	4	358.2 s ≈ 6 min

Table A.1: Comparison of computation time taken to simulate 6 s of the bidomain model with varying spatial resolution, h. The abbreviation "# cores" stands for the number of cores used in the simulation.

A.4 Uncertainty quantification: steady state of the summary statistics

A.4.1 Outlier removal in time series

We kept the summary statistic data points, s_i, satisfying the heuristic criterion

$$|s_i - s_{i-1}| + |s_{i+1} - s_i| < 4.25\left(|s_{i+1} - s_{i-1}| + |s_{i+2} - s_{i-2}|\right), \tag{A.9}$$

where s is a summary statistic time series. This insures that any given data point is close enough to its neighbours, relative to how neighbours are close to one another. We additionally keep the datapoints where

$$i = 1, 2, N-1, N, \tag{A.10}$$

where N is the number of summary statistics in the time series.

A.4.2 Relaxation to steady-state of drug simulations

Here, we present the time evolution of summary statistics in simulations where nifedipine was added. Figure A.2 presents the case where nifedipine was added at concentration 100 nM, and Figure A.3 presents the case for nifedipine at 1000 nM.

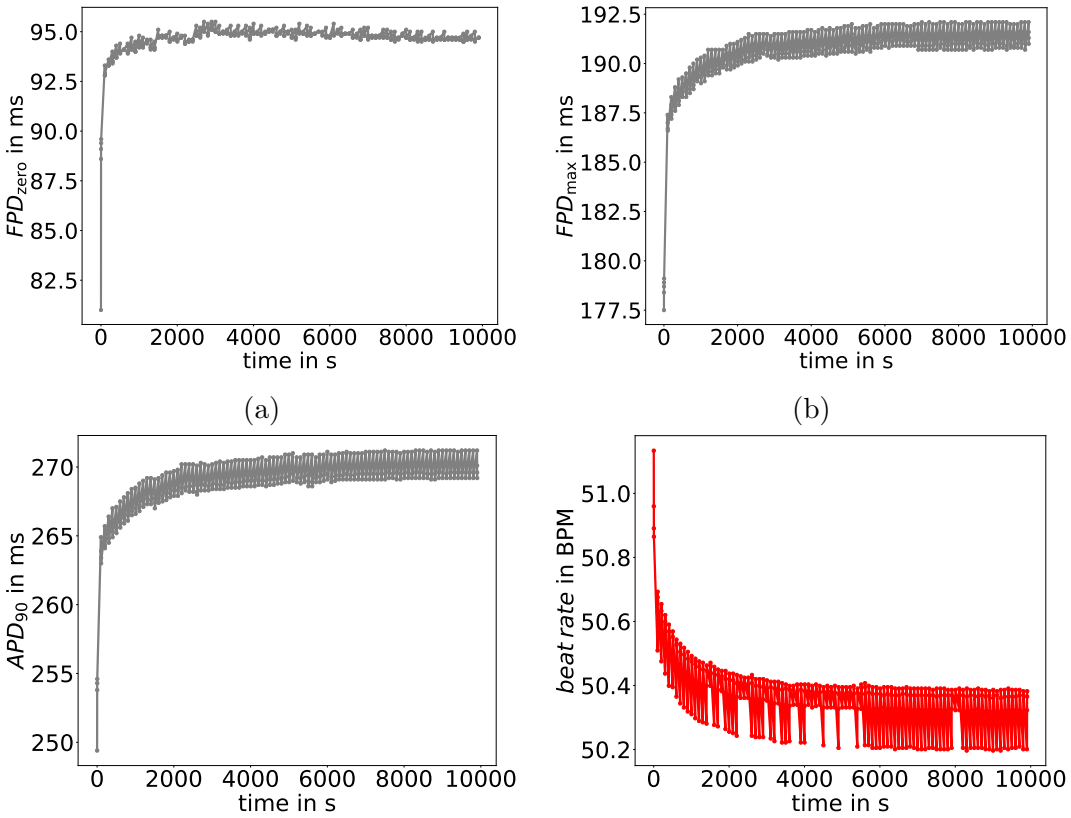


Figure A.2: Time evolution of four summary statistics. The summary statistics were obtained from a simulation where nifedipine at concentration 100 nM was added. The summary statistics were extracted from the output of a simulation with varying printing timestep. Every 100 s, only 6 s of simulation were printed to file. Outlying data points due to faulty detection were removed following the procedure detailed in Section A.4.1. The phenotype realisation chosen is illustrated in Figure 4.12.

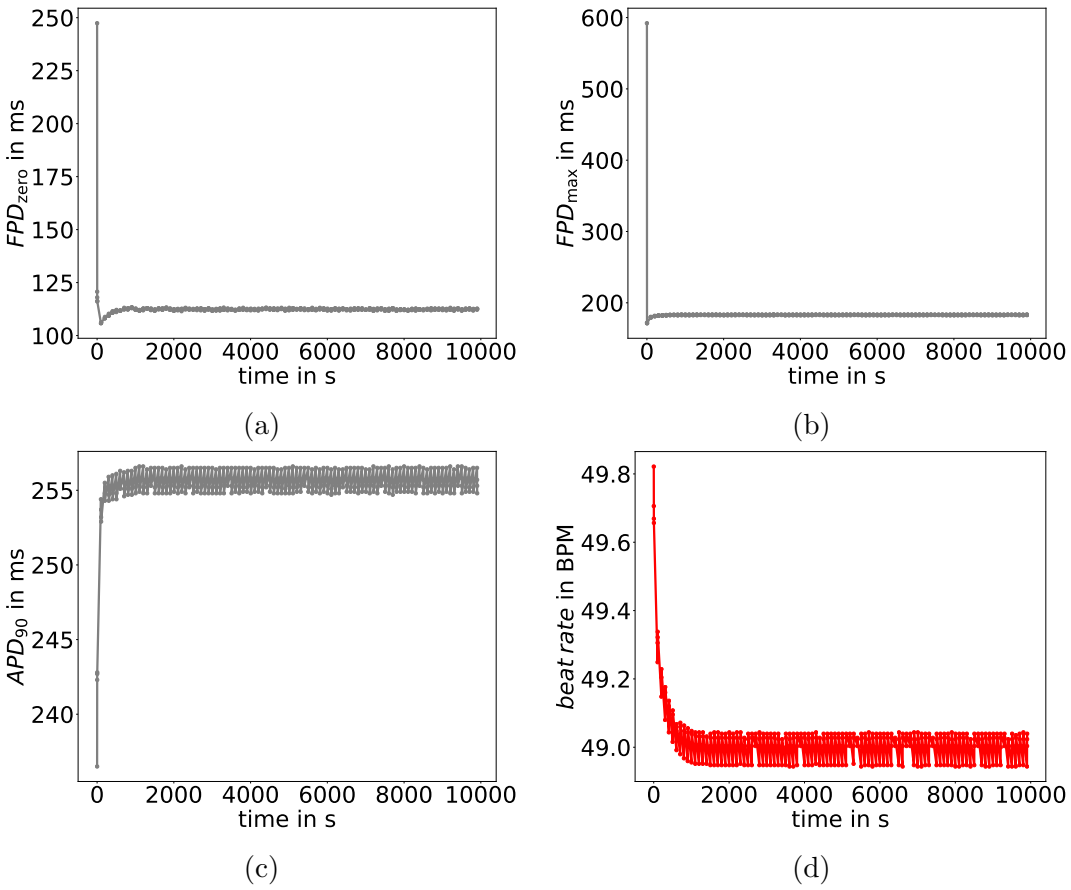


Figure A.3: Time evolution of four summary statistics. The summary statistics were obtained from a simulation where nifedipine at concentration 1000 nM was added. The summary statistics were extracted from the output of a simulation with varying printing timestep. Every 100 s, only 6 s of simulation were printed to file. Outlying data points due to faulty detection were removed following the procedure detailed in Section A.4.1. The phenotype realisation chosen is illustrated in Figure 4.12.

Appendix B

Supplementary information for Chapter 5

This appendix contains additional material relevant to the work covered in Chapter 5. In Section B.1 we present additional comparisons between the simulated and experimental impact of drugs on time to repolarisation biomarkers.

B.1 Effect of drugs on time to repolarisation biomarkers

In Table B.1, we present a summary of the *in silico-in vitro* comparison we conducted for 12 drugs. This summary shows the average root mean squared error (RMSE) of the simulated APD_{90} and $APDc_{90}$ prediction with respect to the experimental $FPD_{\max}$ and. $FPDc_{\max}$ observations. The *in silico-in vitro* comparison for the other biomarkers considered in our study can be found in Table 5.3.

sim. biomarker, exp. biomarker	sim. tissue	sim. mixed	sim. atrial	sim. ventricular
$APD_{90}, FPD_{\max}$	32.5	33.8	37.1	55.4
$APDc_{90}, FPDc_{\max}$	30.3	31.5	33.6	53.0

Table B.1: Average RMSE of the relative change in biomarkers between drugs. The difference between the simulated biomarker and the experimental biomarker given in the first column is used to compute the RMSE. We have included tissue as well as single cell results. The label "sim. mixed" corresponds to the simulation of the single cell model with $\rho_{\mathrm{V}} = 0.54$. Drug concentrations where any biomarker was absent were not included in the RMSE computation. This ensured the fairness of the comparison. The values are given in percentage point. The abbreviation "sim." stands for simulated, and the abbreviation "exp." stands for experimental.

The rest of this section presents a more in-depth simulated-experimental comparison for each class of ion blocking drugs. For I_{CaL}, I_{Kr}, I_{CaL} and I_{Kr}, I_{Na} and I_{Kr}, I_{Na} and I_{Kr} blocking drugs, and quinidine and ranolazine, we present comparisons between biomarkers that were not shown in Section 5.4. Specifically, we present comparisons between simulated $APDc_{90}$ and experimental $FPDc_{zero}$, and between simulated and experimental $FPDc_{max}$. For the I_{Na}, I_{CaL} and I_{Kr} multiblockers vandetanib and tamoxifen, we present the entire *in silico-in vitro* comparison here. The results for the other drugs in the same ion-channel-blocking class, quinidine and ranolazine, were already presented in the main text. The comments made for the comparisons shown in the main text also apply here. These include the cellular model oversensitivity to hERG block, the deficiency of its calcium dynamics formulation, the detection inaccuracy of FPS repolarisation at maximum, the satisfactory performance of the mixed cellular and AL model, and finally the poor performance of the VL model.

B.1.1 I_{CaL} blockers

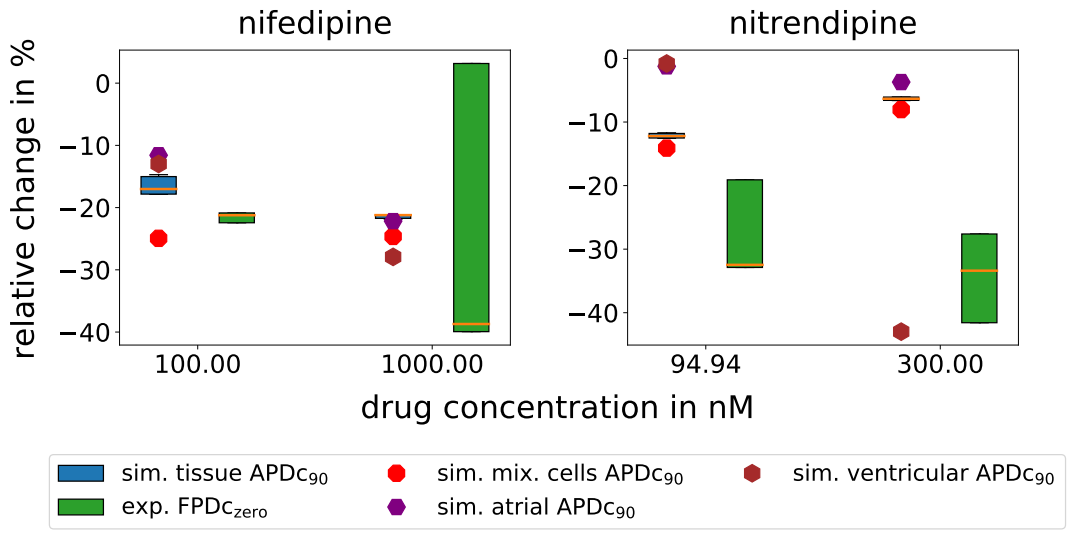


Figure B.1: Change in simulated $APDc_{90}$ and experimental $FPDc_{\mathrm{zero}}$ caused by the addition of nifedipine or nitrendipine. Details are as for Figure 5.16.

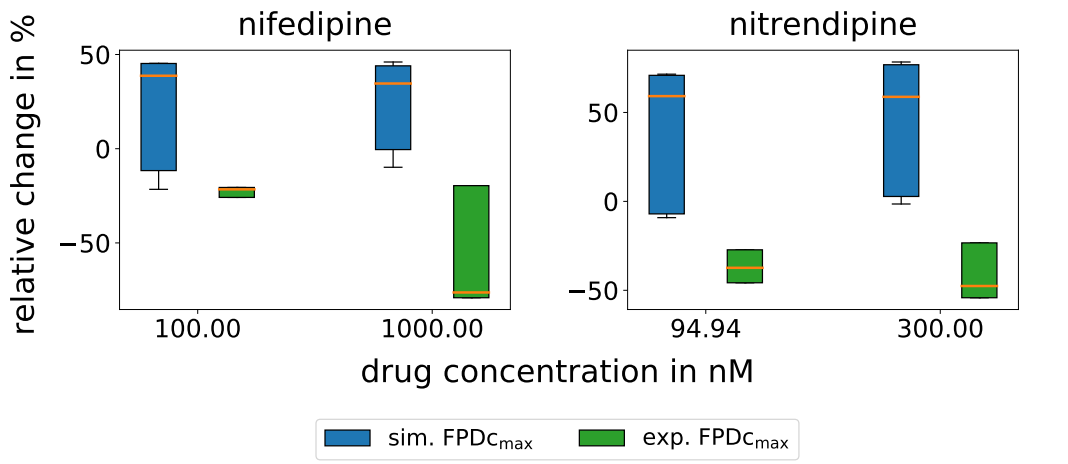


Figure B.2: Change in $FPDc_{\max}$ caused by the addition of nifedipine or nitrendipine. Details are as for Figure 5.14. Details are as for Figure 5.16.

B.1.2 I_{Kr} blockers

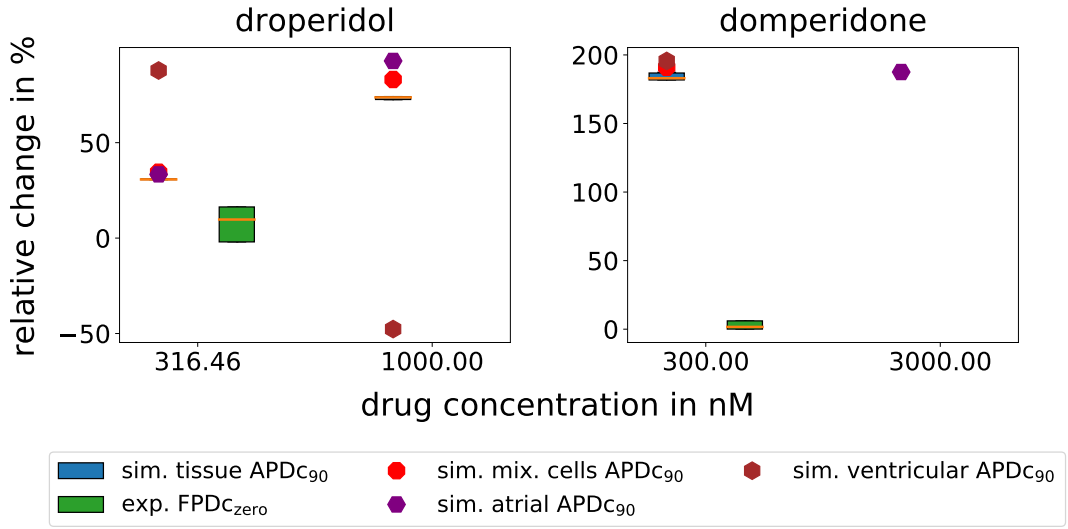


Figure B.3: Change in simulated $APDc_{90}$ and experimental $FPDc_{\mathrm{zero}}$ caused by the addition of droperidol or domperidone.

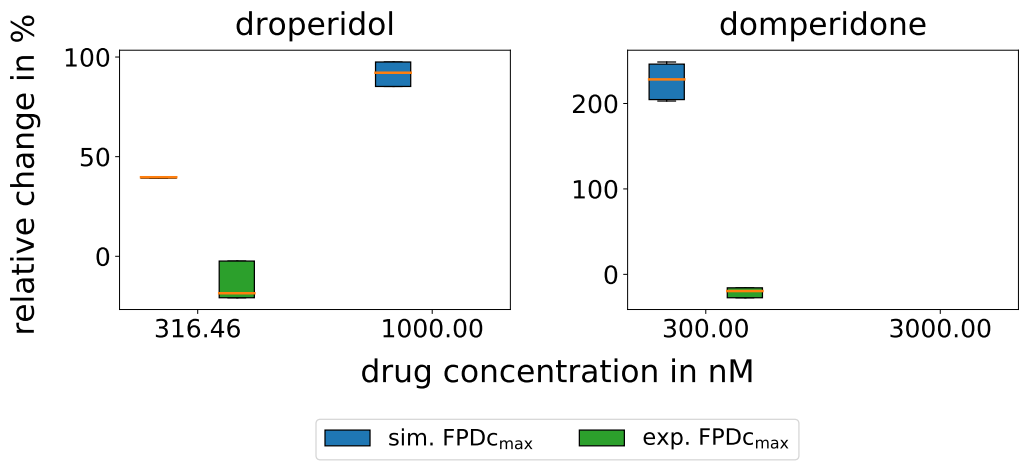


Figure B.4: Change in $FPDc_{\max}$ caused by the addition of droperidol or domperidone. Details are as for Figure 5.14.

B.1.3 I_{CaL} and I_{Kr} balanced blockers

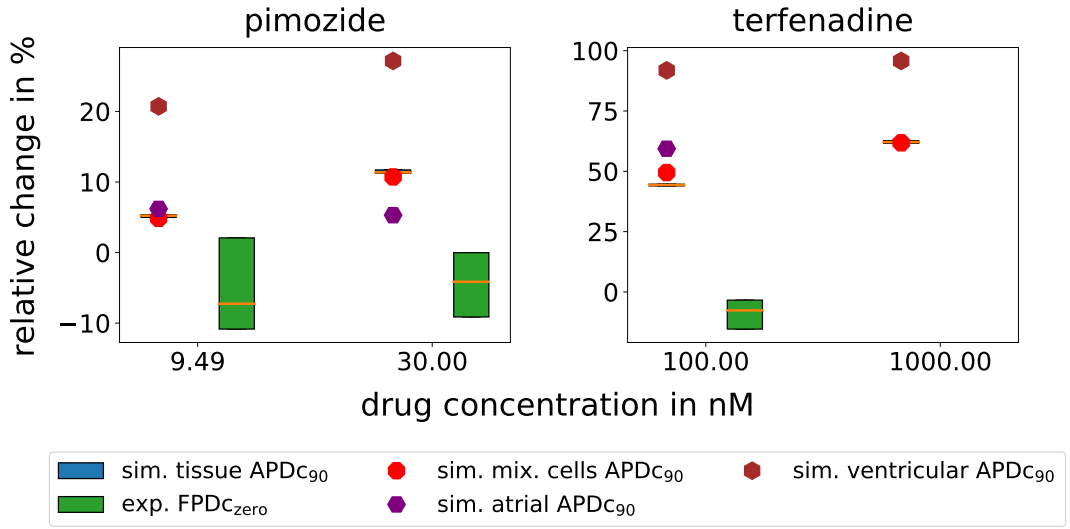


Figure B.5: Change in simulated $APDc_{90}$ and experimental $FPDc_{\mathrm{zero}}$ caused by the addition of pimozide or terfenadine. Details are as for Figure 5.16.

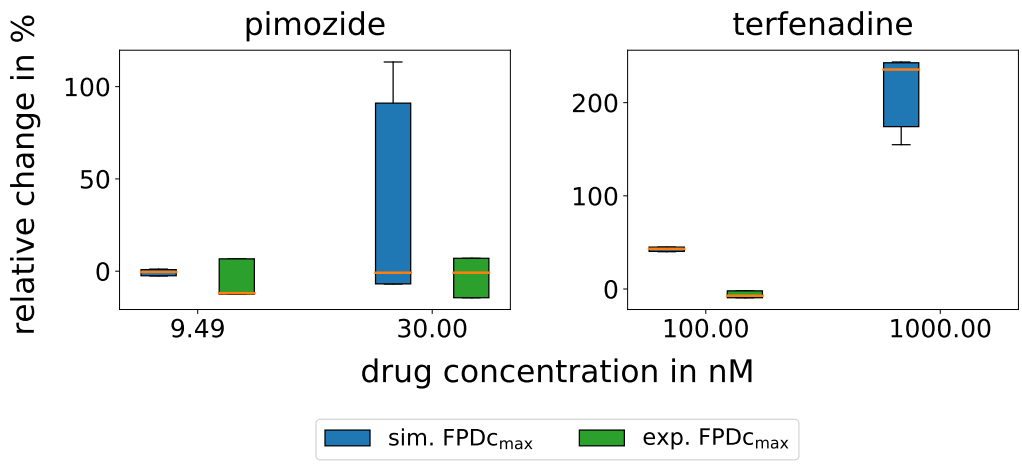


Figure B.6: Change in $FPDc_{\max}$ caused by the addition of pimozide or terfenadine. Details are as for Figure 5.14.

B.1.4 I_{Na} and I_{Kr} multiblockers

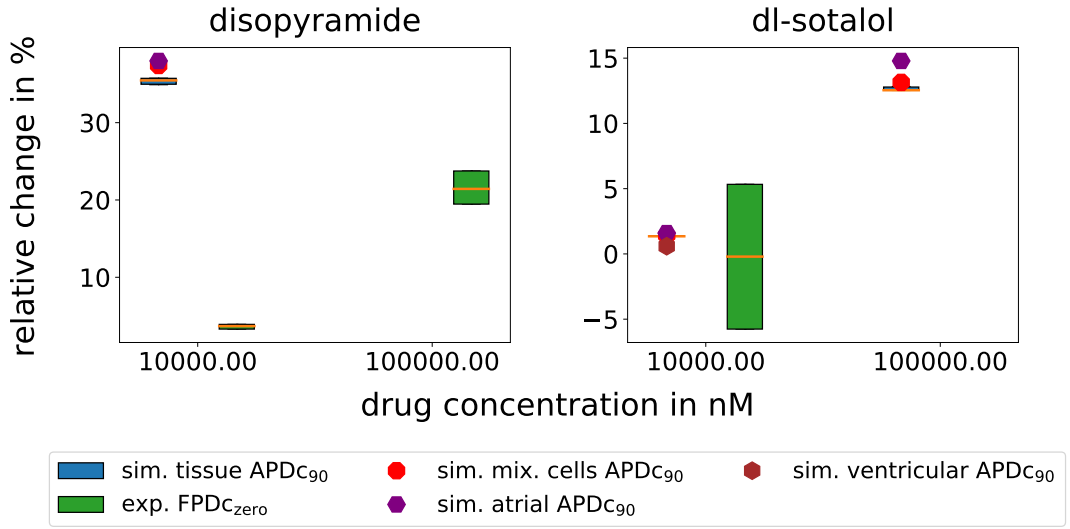


Figure B.7: Change in simulated $APDc_{90}$ and experimental $FPDc_{\mathrm{zero}}$ caused by the addition of disopyramide or dl-soltaol. Details are as for Figure 5.16.

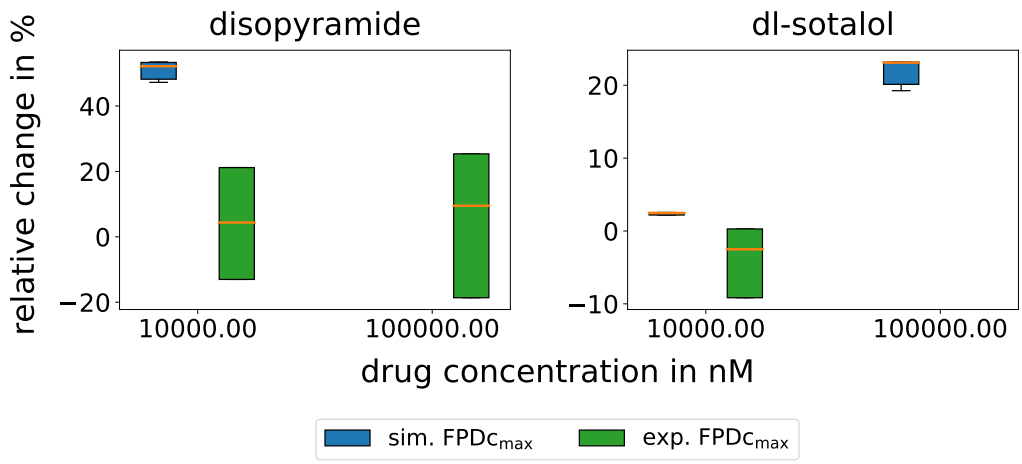


Figure B.8: Change in $FPDc_{\max}$ caused by the addition of disopyramide or dl-sotalol. Details are as for Figure 5.14.

B.1.5 I_{Na}, I_{CaL} and I_{Kr} multiblockers

Quinidine and ranolazine: supplementary figures

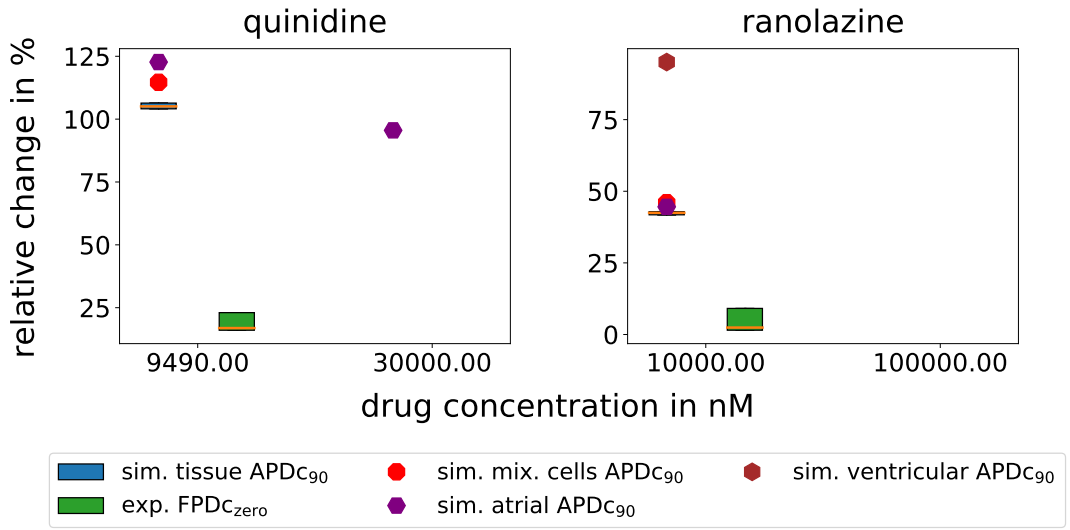


Figure B.9: Change in simulated $APDc_{90}$ and experimental $FPDc_{\mathrm{zero}}$ caused by the addition of quinidine or ranolazine. Details are as for Figure 5.16.

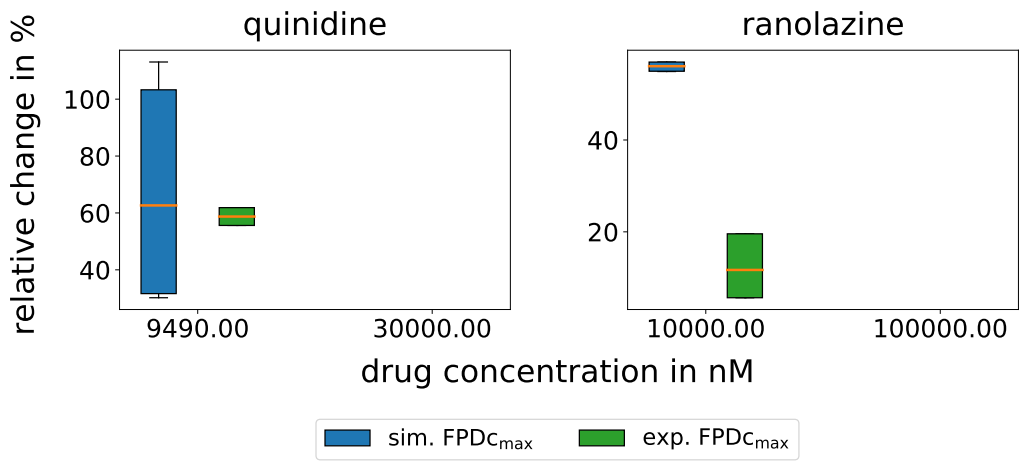


Figure B.10: Change in $FPDc_{\max}$ caused by the addition of quinidine or ranolazine. Details are as for Figure 5.14.

Vandetanib and tamoxifen

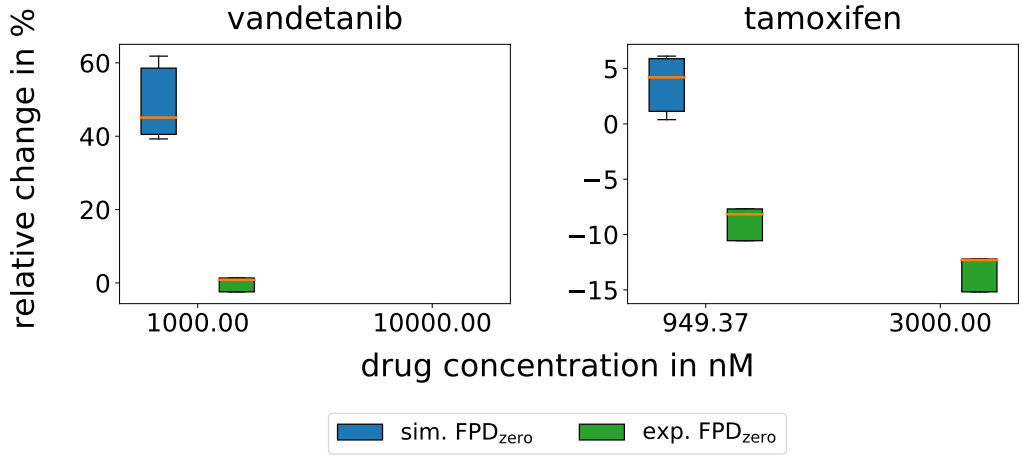


Figure B.11: Change in FPD_{zero} caused by the addition of vandetanib or tamoxifen. Details are as for Figure 5.14.

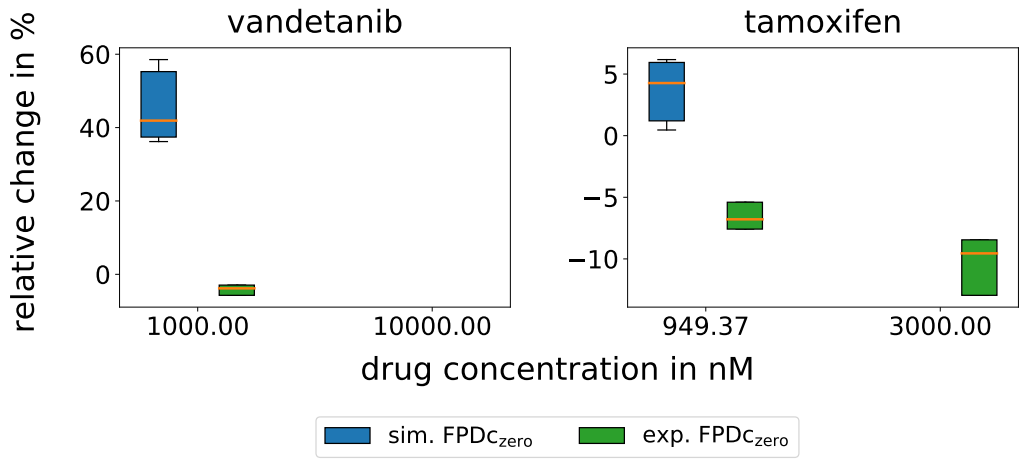


Figure B.12: Change in $FPDc_{\text{zero}}$ caused by the addition of vandetanib or tamoxifen. Details are as for Figure 5.14.

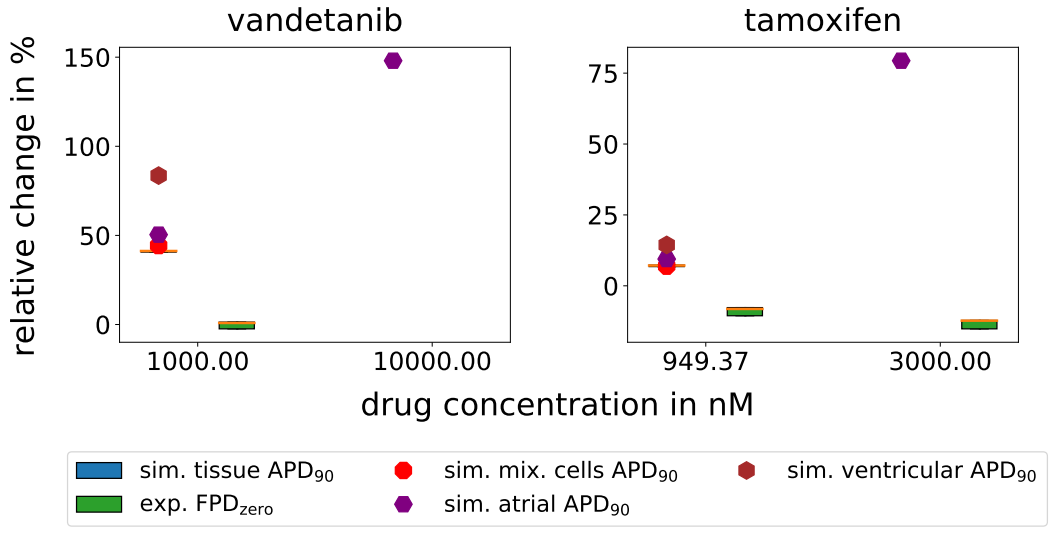


Figure B.13: Change in simulated APD_{90} and experimental FPD_{zero} caused by the addition of vandetanib or tamoxifen. Details are as for Figure 5.16.

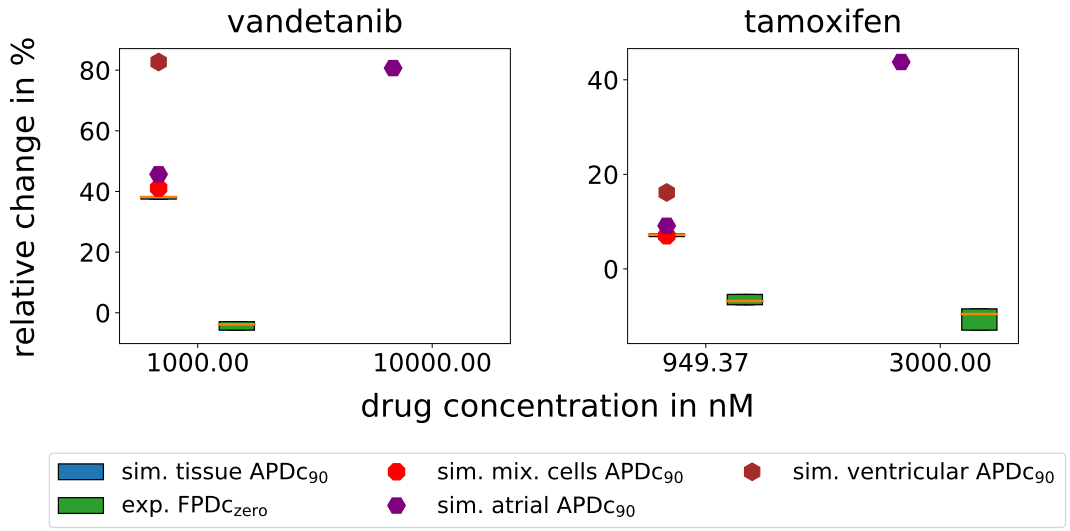


Figure B.14: Change in simulated $APDc_{90}$ and experimental $FPDc_{\text{zero}}$ caused by the addition of vandetanib or tamoxifen. Details are as for Figure 5.14. Details are as for Figure 5.16.

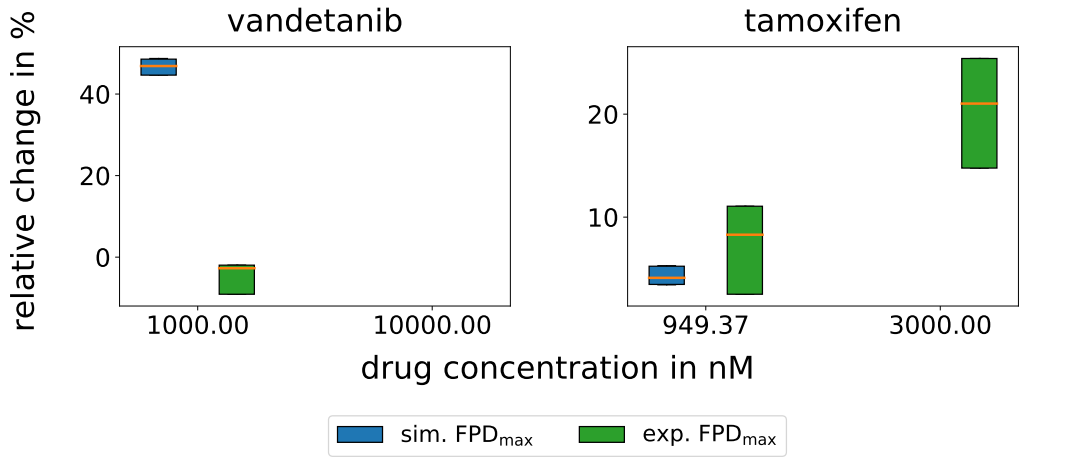


Figure B.15: Change in FPD_{max} caused by the addition of vandetanib or tamoxifen. Details are as for Figure 5.14.

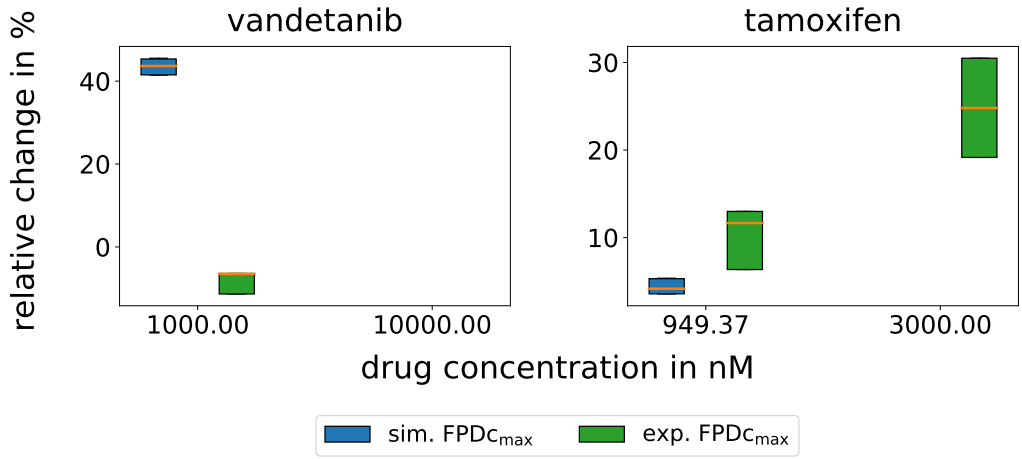


Figure B.16: Change in $FPDc_{\max}$ caused by the addition of vandetanib or tamoxifen. Details are as for Figure 5.14.

References

[1] H. M. Himmel, "Drug-induced functional cardiotoxicity screening in stem cell-derived human and mouse cardiomyocytes: effects of reference compounds," *Journal of Pharmacological and Toxicological Methods*, vol. 68, no. 1, pp. 97–111, 2013. DOI: 10.1016/j.vascn.2013.05.005.

[2] D. M. Roden, "Drug-induced prolongation of the QT interval," *New England Journal of Medicine*, vol. 350, no. 10, A. J. Wood, Ed., pp. 1013–1022, 2004. DOI: 10.1056/NEJMra032426.

[3] J. Vicente, R. Zusterzeel, L. Johannesen, J. Mason, P. Sager, V. Patel, M. K. Matta, Z. Li, J. Liu, C. Garnett, N. Stockbridge, I. Zineh, and D. G. Strauss, "Mechanistic model-informed proarrhythmic risk assessment of drugs: review of the "CiPA" initiative and design of a prospective clinical validation study," *Clinical Pharmacology and Therapeutics*, vol. 103, no. 1, pp. 54–66, 2018. DOI: 10.1002/cpt.896.

[4] F. De Ponti, "Pharmacological and regulatory aspects of QT prolongation," in *Antitargets: Prediction and Prevention of Drug Side Effects*, R. J. Vaz and T. Klabunde, Eds., Weinheim, Germany: John Wiley & Sons, Ltd, 2008, pp. 53–88. DOI: 10.1002/9783527621460.ch3.

[5] P. T. Sager, G. Gintant, J. R. Turner, S. Pettit, and N. Stockbridge, "Rechanneling the cardiac proarrhythmia safety paradigm: a meeting report from the

Cardiac Safety Research Consortium," *American Heart Journal*, vol. 167, no. 3, pp. 292–300, 2014. DOI: 10.1016/j.ahj.2013.11.004.

[6] I. Cavero and W. J. Crumb, "Native and cloned ion channels from human heart: laboratory models for evaluating the cardiac safety of new drugs," *European Heart Journal Supplements*, vol. 3, K53–K63, 2001. DOI: 10.1016/s1520-765x(01)90007-0.

[7] W. J. Crumb, J. Vicente, L. Johannesen, and D. G. Strauss, "An evaluation of 30 clinical drugs against the comprehensive in vitro proarrhythmia assay (CiPA) proposed ion channel panel," *Journal of Pharmacological and Toxicological Methods*, vol. 81, pp. 251–262, 2016. DOI: 10.1016/j.vascn.2016.03.009.

[8] W. Lee, M. J. Windley, J. I. Vandenberg, and A. P. Hill, "In vitro and in silico risk assessment in acquired long QT syndrome: the devil is in the details," *Frontiers in Physiology*, vol. 8, p. 934, 2017. DOI: 10.3389/fphys.2017.00934.

[9] K. Takahashi, K. Tanabe, M. Ohnuki, M. Narita, T. Ichisaka, K. Tomoda, and S. Yamanaka, "Induction of pluripotent stem cells from adult human fibroblasts by defined factors," *Cell*, vol. 131, no. 5, pp. 861–872, 2007. DOI: 10.1016/j.cell.2007.11.019.

[10] A. Eder, I. Vollert, A. Hansen, and T. Eschenhagen, "Human engineered heart tissue as a model system for drug testing," *Advanced Drug Delivery Reviews*, vol. 96, pp. 214–224, 2016. DOI: 10.1016/j.addr.2015.05.010.

[11] G. A. Truskey, "Advancing cardiovascular tissue engineering," *F1000Research*, vol. 5, 2016. DOI: 10.12688/f1000research.8237.1.

[12] B. Zhang and M. Radisic, "Organ-on-a-chip devices advance to market," *Lab on a Chip*, vol. 17, no. 14, pp. 2395–2420, 2017. DOI: 10.1039/c6lc01554a.

[13] Y. Shiba, S. Fernandes, W. Z. Zhu, D. Filice, V. Muskheli, J. Kim, N. J. Palpant, J. Gantz, K. W. Moyes, H. Reinecke, B. Van Biber, T. Dardas, J. L. Mignone, A. Izawa, R. Hanna, M. Viswanathan, J. D. Gold, M. I. Kotlikoff, N. Sarvazyan, M. W. Kay, C. E. Murry, and M. A. Laflamme, "Human ES-cell-derived cardiomyocytes electrically couple and suppress arrhythmias in injured hearts," *Nature*, vol. 489, no. 7415, pp. 322–325, 2012. DOI: 10.1038/nature11317.

[14] P. Menasché, V. Vanneaux, A. Hagège, A. Bel, B. Cholley, A. Parouchev, I. Cacciapuoti, R. Al-Daccak, N. Benhamouda, H. Blons, O. Agbulut, L. Tosca, J. H. Trouvin, J. R. Fabreguettes, V. Bellamy, D. Charron, E. Tartour, G. Tachdjian, M. Desnos, and J. Larghero, "Transplantation of human embryonic stem cell-derived cardiovascular progenitors for severe ischemic left ventricular dysfunction," *Journal of the American College of Cardiology*, vol. 71, no. 4, pp. 429–438, 2018. DOI: 10.1016/j.jacc.2017.11.047.

[15] D. Noble, "A modification of the Hodgkin–Huxley equations applicable to Purkinje fibre action and pace-maker potentials.," *The Journal of Physiology*, vol. 160, no. 2, pp. 317–52, 1962. DOI: 10.1113/jphysiol.1962.sp006849.

[16] M. Paci, J. Hyttinen, K. Aalto-Setälä, and S. Severi, "Computational models of ventricular- and atrial-like human induced pluripotent stem cell derived cardiomyocytes," *Annals of Biomedical Engineering*, vol. 41, no. 11, pp. 2334–2348, 2013. DOI: 10.1007/s10439-013-0833-3.

[17] M. Paci, J. Hyttinen, B. Rodriguez, and S. Severi, "Human induced pluripotent stem cell-derived versus adult cardiomyocytes: an in silico electrophysiological study on effects of ionic current block," *British Journal of Pharmacology*, vol. 172, no. 21, pp. 5147–5160, 2015. DOI: 10.1111/bph.13282.

[18] M. Paci, E. Passini, S. Severi, J. Hyttinen, and B. Rodriguez, "Phenotypic variability in LQT3 human induced pluripotent stem cell-derived cardiomyocytes and their response to antiarrhythmic pharmacologic therapy: an in silico approach," *Heart Rhythm*, vol. 14, no. 11, pp. 1704–1712, 2017. DOI: 10.1016/j.hrthm.2017.07.026.

[19] M. Paci, R. P. Pölönen, D. Cori, K. Penttinen, K. Aalto-Setälä, S. Severi, and J. Hyttinen, "Automatic optimization of an in silico model of human iPSC derived cardiomyocytes recapitulating calcium handling abnormalities," *Frontiers in Physiology*, vol. 9, pp. 1–14, 2018. DOI: 10.3389/fphys.2018.00709.

[20] J. Ma, L. Guo, S. J. Fiene, B. D. Anson, J. A. Thomson, T. J. Kamp, K. L. Kolaja, B. J. Swanson, and C. T. January, "High purity human-induced pluripotent stem cell-derived cardiomyocytes: electrophysiological properties of action potentials and ionic currents," *American Journal of Physiology-Heart and Circulatory Physiology*, vol. 301, no. 5, H2006–H2017, 2011. DOI: 10.1152/ajpheart.00694.2011.

[21] L. A. Bowler, D. J. Gavaghan, G. R. Mirams, and J. P. Whiteley, "Representation of multiple cellular phenotypes within tissue-level simulations of cardiac electrophysiology," *Bulletin of Mathematical Biology*, 2018. DOI: 10.1007/s11538-018-0516-1.

[22] E. Abbate, M. Boulakia, Y. Coudière, J. F. Gerbeau, P. Zitoun, and N. Zemzemi, "In silico assessment of the effects of various compounds in MEA/hiPSC-CM assays: modeling and numerical simulations," *Journal of Pharmacological and Toxicological Methods*, vol. 89, pp. 59–72, 2018. DOI: 10.1016/j.vascn.2017.10.005.

[23] M. L. Vestergaard, S. J. Grubb, K. K. Rasmussen, Z. Anderson-Jenkins, K. Grunnet-Lauridsen, K. Calloe, C. Clausen, S. T. Christensen, K. Møllgård, and C. Y. Andersen, "Human embryonic stem cell derived cardiomyocytes self-arrange with areas of different subtypes during differentiation," *Stem Cells and Development*, vol. 26, no. 21, pp. 1566–1577, 2017. DOI: 10.1089/scd.2017.0054.

[24] R. Zhu, M. A. Millrod, E. T. Zambidis, and L. Tung, "Variability of action potentials within and among cardiac cell clusters derived from human embryonic stem cells," *Scientific Reports*, vol. 6, p. 18 544, 2016. DOI: 10.1038/srep18544.

[25] L. Bowler, "Modelling and simulation of phenotypic variability in cardiac tissue and application to stem cell-derived cardiomyocytes," PhD thesis, University of Oxford, 2018.

[26] C. L. Lei, K. Wang, M. Clerx, R. H. Johnstone, M. P. Hortigon-Vinagre, V. Zamora, A. Allan, G. L. Smith, D. J. Gavaghan, G. R. Mirams, and L. Polonchuk, "Tailoring mathematical models to stem-cell derived cardiomyocyte lines can improve predictions of drug-induced changes to their electrophysiology," *Frontiers in Physiology*, vol. 8, p. 986, 2017. DOI: 10.3389/fphys.2017.00986.

[27] G. R. Mirams, C. J. Arthurs, M. O. Bernabeu, R. Bordas, J. Cooper, A. Corrias, Y. Davit, S. J. Dunn, A. G. Fletcher, D. G. Harvey, M. E. Marsh, J. M. Osborne, P. Pathmanathan, J. Pitt-Francis, J. Southern, N. Zemzemi, and D. J. Gavaghan, "Chaste: an open source C++ library for computational physiology and biology," *PLoS Computational Biology*, vol. 9, no. 3, 2013. DOI: 10.1371/journal.pcbi.1002970.

[28] S. Cohen and A. Hindmarsh, "Cvode, a stiff/nonstiff ode solver in C," *Computers in Physics*, vol. 10, no. 2, pp. 138–143, 1996. DOI: 10.1063/1.4822377.

[29] J. Cooper, R. J. Spiteri, and G. R. Mirams, "Cellular cardiac electrophysiology modeling with Chaste and CellML," *Frontiers in Physiology*, vol. 6, pp. 1–16, 2015. DOI: 10.3389/fphys.2014.00511.

[30] J. R. Levick, *Introduction to cardiovascular physiology*. Oxford, United Kingdom: Elsevier Science & Technology, 1991.

[31] B. F. Fremgen and S. S. Frucht, *Medical terminology: a living language*, Seventh ed. Hoboken, New Jersey: Pearson Education, 2017.

[32] R. E. Klabunde, *Cardiovascular physiology concepts*, Second edi. Philadelphia, PA: Lippincott Williams and Wilkins/Wolters Kluwer, 2012.

[33] P. I. Aaronson, J. P. T. Ward, and M. J. Connelly, *The cardiovascular system at a glance*, 4th, ser. At a Glance Ser. Somerset: John Wiley & Sons, Incorporated, 2012.

[34] W. Nernst, "Zur Kinetik der in Lösung befindlichen Körper [The kinetics of bodies in solution]," *Zeitschrift für Physikalische Chemie*, vol. 2U, no. 1, pp. 613–637, 1888. DOI: 10.1515/zpch-1888-0274.

[35] A. C. Daly, J. Cooper, D. J. Gavaghan, and C. Holmes, "Comparing two sequential Monte Carlo samplers for exact and approximate Bayesian inference on biological models," *Journal of the Royal Society Interface*, vol. 14, no. 134, 2017. DOI: 10.1098/rsif.2017.0340.

[36] M. J. Windley, W. Lee, J. I. Vandenberg, and A. P. Hill, "The temperature dependence of kinetics associated with drug block of herg channels is compound-specific and an important factor for proarrhythmic risk prediction," *Molecular Pharmacology*, vol. 94, no. 1, pp. 760–769, 2018. DOI: 10.1124/mol.117.111534.

[37] A. J. Pullan, L. K. Cheng, and M. L. Buist, *Mathematically modelling the electrical activity of the heart: from cell to body surface and back again*. New Jersey: World Scientific, 2005.

[38] B. Fermini and A. A. Fossa, "The impact of drug-induced QT interval prolongation on drug discovery and development," *Nature Reviews Drug Discovery*, vol. 2, no. 6, pp. 439–447, 2003. DOI: 10.1038/nrd1108.

[39] D. F. Dickinson, "The normal ECG in childhood and adolescence," *Heart*, vol. 91, no. 12, pp. 1626–1630, 2005. DOI: 10.1136/hrt.2004.057307.

[40] P. Sahu, "QT dispersion in medicine: electrophysiological Holy Grail or fool's gold?" *QJM*, vol. 93, no. 7, pp. 425–431, 2000. DOI: 10.1093/qjmed/93.7.425.

[41] P. G. Postema and A. A. M. Wilde, "The measurement of the QT interval," *Current Cardiology Reviews*, vol. 10, no. 3, pp. 287–294, 2014. DOI: 10.2174/1573403X10666140514103612.

[42] S. Zhang, Z. Zhou, Q. Gong, J. C. Makielski, and C. T. January, "Mechanism of block and identification of the verapamil binding domain to HERG potassium channels," *Circulation Research*, vol. 84, no. 9, pp. 989–998, 1999. DOI: 10.1161/01.RES.84.9.989.

[43] G. T. Dempsey, K. W. Chaudhary, N. Atwater, C. Nguyen, B. S. Brown, J. D. McNeish, A. E. Cohen, and J. M. Kralj, "Cardiotoxicity screening with simultaneous optogenetic pacing, voltage imaging and calcium imaging," *Journal of Pharmacological and Toxicological Methods*, vol. 81, pp. 240–250, 2016. DOI: 10.1016/j.vascn.2016.05.003.

[44] F. Administration and Drug, *E14 clinical evaluation of QT/QTc interval prolongation and proarrhythmic potential for non antiarrhythmic drugs questions and answers (R3)*, 2017. [Online]. Available: https://www.fda.gov/media/71379/download.

[45] B. Vandenberk, E. Vandael, T. Robyns, J. Vandenberghe, C. Garweg, V. Foulon, J. Ector, and R. Willems, "Which QT correction formulae to use for QT monitoring?" *Journal of the American Heart Association*, vol. 5, no. 6, 2016. DOI: 10.1161/JAHA.116.003264.

[46] Y. G. Yap and A. J. Camm, "Drug induced QT prolongation and torsades de pointes," *Heart*, vol. 89, no. 11, pp. 1363–1372, 2003. DOI: 10.1136/heart.89.11.1363.

[47] W. S. Redfern, L. Carlsson, A. S. Davis, W. G. Lynch, I. MacKenzie, S. Palethorpe, P. K. Siegl, I. Strang, A. T. Sullivan, R. Wallis, A. J. Camm, and T. G. Hammond, "Relationships between preclinical cardiac electrophysiology, clinical QT interval prolongation and torsade de pointes for a broad range of drugs: Evidence for a provisional safety margin in drug development," *Cardiovascular Research*, vol. 58, no. 1, pp. 32–45, 2003. DOI: 10.1016/S0008-6363(02)00846-5.

[48] C. L. Lawrence, C. E. Pollard, T. G. Hammond, and J. P. Valentin, "Nonclinical proarrhythmia models: predicting torsades de pointes," *Journal of Pharmacological and Toxicological Methods*, vol. 52, no. 1, pp. 46–59, 2005. DOI: 10.1016/j.vascn.2005.04.011.

[49] K. Blinova, Q. Dang, D. Millard, G. Smith, J. Pierson, L. Guo, M. Brock, H. R. Lu, U. Kraushaar, H. Zeng, H. Shi, X. Zhang, K. Sawada, T. Osada, Y. Kanda, Y. Sekino, L. Pang, T. K. Feaster, R. Kettenhofen, N. Stockbridge, D. G. Strauss, and G. Gintant, "International multisite study of human-induced pluripotent stem cell-derived cardiomyocytes for drug proarrhythmic potential assessment," *Cell Reports*, vol. 24, no. 13, pp. 3582–3592, 2018. DOI: 10.1016/j.celrep.2018.08.079.

[50] J. Zhang, G. F. Wilson, A. G. Soerens, C. H. Koonce, J. Yu, S. P. Palecek, J. A. Thomson, and T. J. Kamp, "Functional cardiomyocytes derived from human induced pluripotent stem cells," *Circulation Research*, vol. 104, no. 4, pp. 30–41, 2009. DOI: 10.1161/CIRCRESAHA.108.192237.

[51] O. Caspi, A. Lesman, Y. Basevitch, A. Gepstein, G. Arbel, I. Huber, M. Habib, L. Gepstein, and S. Levenberg, "Tissue engineering of vascularized cardiac muscle from human embryonic stem cells," *Circulation Research*, vol. 100, no. 2, pp. 263–272, 2007. DOI: 10.1161/01.RES.0000257776.05673.ff.

[52] N. L. Tulloch, V. Muskheli, M. V. Razumova, F. S. Korte, M. Regnier, K. D. Hauch, L. Pabon, H. Reinecke, and C. E. Murry, "Growth of engineered human myocardium with mechanical loading and vascular coculture," *Circulation Research*, vol. 109, no. 1, pp. 47–59, 2011. DOI: 10.1161/CIRCRESAHA.110.237206.

[53] R. J. Mills and J. E. Hudson, "Bioengineering adult human heart tissue: how close are we?" *APL Bioengineering*, vol. 3, no. 1, p. 010 901, 2019. DOI: 10.1063/1.5070106.

[54] K. Ronaldson-Bouchard, S. P. Ma, K. Yeager, T. Chen, L. J. Song, D. Sirabella, K. Morikawa, D. Teles, M. Yazawa, and G. Vunjak-Novakovic, "Advanced maturation of human cardiac tissue grown from pluripotent stem cells," *Nature*, vol. 556, no. 7700, pp. 239–243, 2018. DOI: 10.1038/s41586-018-0016-3.

[55] I. Goldfracht, Y. Efraim, R. Shinnawi, E. Kovalev, I. Huber, A. Gepstein, G. Arbel, N. Shaheen, M. Tiburcy, W. H. Zimmermann, M. Machluf, and L. Gepstein, "Engineered heart tissue models from hiPSC-derived cardiomyocytes and cardiac ECM for disease modeling and drug testing applications," *Acta Biomaterialia*, vol. 92, pp. 145–159, 2019. DOI: 10.1016/j.actbio.2019.05.016.

[56] D. T. M. Du, N. Hellen, C. Kane, and C. M. N. Terracciano, "Action potential morphology of human induced pluripotent stem cell-derived cardiomyocytes does not predict cardiac chamber specificity and is dependent on cell density," *Biophysical Journal*, vol. 108, no. 1, pp. 1–4, 2015. DOI: 10.1016/j.bpj.2014.11.008.

[57] Z. Chen, W. Xian, M. Bellin, T. Dorn, Q. Tian, A. Goedel, L. Dreizehnter, C. M. Schneider, D. Ward-Van Oostwaard, J. K. M. Ng, R. Hinkel, L. S. Pane, C. L. Mummery, P. Lipp, A. Moretti, K. L. Laugwitz, and D. Sinnecker, "Subtype-specific promoter-driven action potential imaging for precise disease modelling and drug testing in hiPSC-derived cardiomyocytes," *European Heart Journal*, vol. 38, no. 4, pp. 292–301, 2017. DOI: 10.1093/eurheartj/ehw189.

[58] L. Cyganek, M. Tiburcy, K. Sekeres, K. Gerstenberg, H. Bohnenberger, C. Lenz, S. Henze, M. Stauske, G. Salinas, W.-H. Zimmermann, G. Hasenfuss, and K. Guan, "Deep phenotyping of human induced pluripotent stem cell–derived atrial and ventricular cardiomyocytes," *JCI Insight*, vol. 3, no. 12, e99941, 2018. DOI: 10.1172/jci.insight.99941.

[59] A. L. Hodgkin and A. F. Huxley, "A quantitative description of membrane current and its application to conduction and excitation in nerve," *The Journal of Physiology*, vol. 117, no. 4, pp. 500–544, 1952. DOI: 10.1113/jphysiol.1952.sp004764.

[60] J. P. Keener and J. Sneyd, *Mathematical physiology*. New York: Springer, 1998, vol. 1.

[61] A. L. Hodgkin, A. F. Huxley, and B. Katz, "Measurement of current-voltage relations in the membrane of the giant axon of Loligo," *The Journal of Physiology*, vol. 116, no. 4, pp. 424–448, 1952. DOI: 10.1113/jphysiol.1952.sp004716.

[62] A. L. Hodgkin and A. F. Huxley, "Currents carried by sodium and potassium ions through the membrane of the giant axon of Loligo," *The Journal of Physiology*, vol. 116, no. 4, pp. 449–472, 1952. DOI: 10.1113/jphysiol.1952.sp004717.

[63] A. L. Hodgkin and A. F. Huxley, "The components of membrane conductance in the giant axon of Loligo," *The Journal of Physiology*, vol. 116, no. 4, pp. 473–496, 1952. DOI: 10.1113/jphysiol.1952.sp004718.

[64] A. L. Hodgkin and A. F. Huxley, "The dual effect of membrane potential on sodium conductance in the giant axon of Loligo," *The Journal of Physiology*, vol. 116, no. 4, pp. 497–506, 1952. DOI: 10.1113/jphysiol.1952.sp004719.

[65] D. Beeman, "Hodgkin-Huxley model," in *Encyclopedia of Computational Neuroscience*, New York: Springer New York, 2014, pp. 1–13. DOI: 10.1007/978-1-4614-7320-6_127-3.

[66] D. Noble, "From the Hodgkin-Huxley axon to the virtual heart," *Journal of Physiology*, vol. 580, no. 1, pp. 15–22, 2007. DOI: 10.1113/jphysiol.2006.119370.

[67] D. Noble, A. Garny, and P. J. Noble, "How the Hodgkin-Huxley equations inspired the Cardiac Physiome Project," *The Journal of Physiology*, vol. 590, no. 11, pp. 2613–2628, 2012. DOI: 10.1113/jphysiol.2011.224238.

[68] H. Reuter, "The dependence of slow inward current in Purkinje fibres on the extracellular calcium-concentration," *The Journal of Physiology*, vol. 192, no. 2, pp. 479–492, 1967. DOI: 10.1113/jphysiol.1967.sp008310.

[69] M. R. Davies, K. Wang, G. R. Mirams, A. Caruso, D. Noble, A. Walz, T. Lavé, F. Schuler, T. Singer, and L. Polonchuk, "Recent developments in using mechanistic cardiac modelling for drug safety evaluation," *Drug Discovery Today*, vol. 21, no. 6, pp. 924–938, 2016. DOI: 10.1016/j.drudis.2016.02.003.

[70] J. T. Koivumäki, N. Naumenko, T. Tuomainen, J. Takalo, M. Oksanen, K. A. Puttonen, Š. Lehtonen, J. Kuusisto, M. Laakso, J. Koistinaho, and P. Tavi, "Structural immaturity of human iPSC-derived cardiomyocytes: in silico investigation of effects on function and disease modeling," *Frontiers in Physiology*, vol. 9, pp. 1–17, 2018. DOI: 10.3389/fphys.2018.00080.

[71] M. Paci, L. Sartiani, M. Del Lungo, M. Jaconi, A. Mugelli, E. Cerbai, and S. Severi, "Mathematical modelling of the action potential of human embryonic stem cell derived cardiomyocytes," *Biomedical Engineering Online*, vol. 11, no. 1, p. 61, 2012. DOI: 10.1186/1475-925X-11-61.

[72] A. V. Hill, "The combinations of haemoglobin with oxygen and with carbon monoxide. I.," *The Biochemical Journal*, vol. 7, no. 5, pp. 471–80, 1913. DOI: 10.1042/bj0070471.

[73] G. R. Mirams, Y. Cui, A. Sher, M. Fink, J. Cooper, B. M. Heath, N. C. McMahon, D. J. Gavaghan, and D. Noble, "Simulation of multiple ion channel block provides improved prediction of compounds' clinical torsadogenic risk," *Cardiovascular Research*, vol. 91, no. 1, pp. 53–61, 2011. DOI: 10.1093/cvr/cvr044.

[74] S. M. Kandel, "The electrical bidomain model: a review," *Scholars Academic Journal of Biosciences*, vol. 3, no. 7, pp. 633–639, 2015.

[75] O. H. Schmitt, "Biological information processing using the concept of interpenetrating domains," in *Information Processing in The Nervous System*, Berlin, Heidelberg: Springer Berlin Heidelberg, 1969, pp. 325–331. DOI: 10.1007/978-3-662-25549-0_18.

[76] A. L. Muler and V. S. Markin, "Electrical properties of anisotropic neuromuscular syncytia. I. Distribution of the electrotonic potential (translated from Russian)," *Biofizika*, vol. 22, no. 2, pp. 307–12, 1977.

[77] L. Tung, "A bi-domain model for describing ischemic myocardial d-c potentials," PhD thesis, Massachusetts Institute of Technology, 1978. DOI: 1721.1/16177.

[78] W. T. Miller and D. B. Geselowitz, "Simulation studies of the electrocardiogram. I. The normal heart.," *Circulation Research*, vol. 43, no. 2, pp. 301–315, 1978. DOI: 10.1161/01.RES.43.2.301.

[79] R. Plonsey and R. C. Barr, "Current flow patterns in two-dimensional anisotropic bisyncytia with normal and extreme conductivities," *Biophysical Journal*, vol. 45, no. 3, pp. 557–71, 1984. DOI: 10.1016/S0006-3495(84)84193-4.

[80] R. C. Barr and R. Plonsey, "Propagation of excitation in idealized anisotropic two-dimensional tissue," *Biophysical Journal*, vol. 45, no. 6, pp. 1191–1202, 1984. DOI: 10.1016/S0006-3495(84)84268-X.

[81] B. J. Roth and J. P. J. Wikswo, "A bidomain model for the extracellular potential and magnetic field of cardiac tissue," *IEEE Transactions on Biomedical Engineering*, vol. 33, no. 4, pp. 467–469, 1986. DOI: 10.1109/TBME.1986.325804.

[82] N. G. Sepulveda and J. P. J. Wikswo, "Electric and magnetic fields from two-dimensional anisotropic bisyncytia," *Biophysical Journal*, vol. 51, no. 4, pp. 557–68, 1987. DOI: 10.1016/S0006-3495(87)83381-7.

[83] R. Plonsey and R. C. Barr, "Interstitial potentials and their change with depth into cardiac tissue," *Biophysical Journal*, vol. 51, no. 4, pp. 547–55, 1987. DOI: 10.1016/S0006-3495(87)83380-5.

[84] P. Pathmanathan, M. O. Bernabeu, R. Bordas, J. Cooper, A. Garny, J. M. Pitt-Francis, J. P. Whiteley, and D. J. Gavaghan, "A numerical guide to the solution of the bidomain equations of cardiac electrophysiology," *Progress in*

Biophysics and Molecular Biology, vol. 102, no. 2-3, pp. 136–155, 2010. DOI: 10.1016/j.pbiomolbio.2010.05.006.

[85] L. Doerr, U. Thomas, D. R. Guinot, C. T. Bot, S. Stoelzle-Feix, M. Beckler, M. George, and N. Fertig, "New easy-to-use hybrid system for extracellular potential and impedance recordings," *Journal of Laboratory Automation*, vol. 20, no. 2, pp. 175–188, 2015. DOI: 10.1177/2211068214562832.

[86] A. Obergrussberger, K. Juhasz, U. Thomas, S. Stölzle-Feix, N. Becker, L. Dörr, M. Beckler, C. Bot, M. George, and N. Fertig, "Safety pharmacology studies using EFP and impedance," *Journal of Pharmacological and Toxicological Methods*, vol. 81, pp. 223–232, 2016. DOI: 10.1016/j.vascn.2016.04.006.

[87] A. Obergrussberger, U. Thomas, S. Stölzle-Feix, N. Becker, K. Juhasz, L. Doerr, M. Beckler, M. George, and N. Fertig, "Combined impedance and extracellular field potential recordings from human stem cell-derived cardiomyocytes," in, Humana Press, New York, NY, 2017, pp. 191–209. DOI: 10.1007/978-1-4939-6661-5_10.

[88] C. Geuzaine and J.-F. Remacle, "Gmsh: a 3-D finite element mesh generator with built-in pre- and post-processing facilities," *International Journal for Numerical Methods in Engineering*, vol. 79, no. 11, pp. 1309–1331, 2009. DOI: 10.1002/nme.2579.

[89] B. Stroustrup and Bjarne, *The C++ programming language*. Addison-Wesley, 2000.

[90] *CellProperties class in Chaste*, 2011.

[91] R. M. Shaw and Y. Rudy, "Electrophysiologic effects of acute myocardial ischemia: a mechanistic investigation of action potential conduction and conduction failure," *Circulation Research*, vol. 80, no. 1, pp. 124–138, 1997. DOI: 10.1161/01.RES.80.1.124.

[92] CiPA, *Recommended voltage protocols to study drug-cardiac ion channel interactions using recombinant cell lines*, 2018. [Online]. Available: https://www.fda.gov/media/129686/download.

[93] J. Bezanson, A. Edelman, S. Karpinski, and V. B. Shah, "Julia: a fresh approach to numerical computing," vol. 59, no. 1, pp. 65–98, 2014. DOI: 10.1137/141000671.

[94] J. Pitt-Francis, P. Pathmanathan, M. O. Bernabeu, R. Bordas, J. Cooper, A. G. Fletcher, G. R. Mirams, P. Murray, J. M. Osborne, A. Walter, S. J. Chapman, A. Garny, I. M. M. van Leeuwen, P. K. Maini, B. Rodríguez, S. L. Waters, J. P. Whiteley, H. M. Byrne, and D. J. Gavaghan, "Chaste: a test-driven approach to software development for biological modelling," *Computer Physics Communications*, vol. 180, no. 12, pp. 2452–2471, 2009. DOI: 10.1016/j.cpc.2009.07.019.

[95] C. T. Bot, K. Juhasz, F. Haeusermann, L. Polonchuk, M. Traebert, and S. Stoelzle-Feix, "Cross-site comparison of excitation-contraction coupling using impedance and field potential recordings in hiPSC cardiomyocytes," *Journal of Pharmacological and Toxicological Methods*, vol. 93, pp. 46–58, 2018. DOI: 10.1016/j.vascn.2018.06.006.

[96] S. R. Braam, L. Tertoolen, A. van de Stolpe, T. Meyer, R. Passier, and C. L. Mummery, "Prediction of drug-induced cardiotoxicity using human embryonic stem cell-derived cardiomyocytes," *Stem Cell Research*, vol. 4, no. 2, pp. 107–116, 2010. DOI: 10.1016/j.scr.2009.11.004.

[97] R. A. Chowdhury, K. N. Tzortzis, E. Dupont, S. Selvadurai, F. Perbellini, C. D. Cantwell, F. S. Ng, A. R. Simon, C. M. Terracciano, and N. S. Peters, "Concurrent micro- to macro-cardiac electrophysiology in myocyte cultures

and human heart slices," *Scientific Reports*, vol. 8, no. 1, pp. 1–13, 2018. DOI: 10.1038/s41598-018-25170-9.

[98] C. Sprössler, M. Denyer, S. Britland, W. Knoll, and A. Offenhäusser, "Electrical recordings from rat cardiac muscle cells using field-effect transistors," *Physical Review E - Statistical Physics, Plasmas, Fluids, and Related Interdisciplinary Topics*, vol. 60, no. 2, pp. 2171–2176, 1999. DOI: 10.1103/PhysRevE.60.2171.

[99] L. Doerr, "Real-time cardiac cell analysis by high-resolution extracellular potential recording in a true parallel 96-well format," Technische Universität München, Munich, Tech. Rep., 2014.

[100] B. Trenor, J. Gomis-Tena, K. Cardona, L. Romero, S. Rajamani, L. Belardinelli, W. R. Giles, and J. Saiz, "In silico assessment of drug safety in human heart applied to late sodium current blockers," *Channels*, vol. 7, no. 4, pp. 249–262, 2013. DOI: 10.4161/chan.24905.

[101] L. S. Fridericia, "The duration of systole in an electrocardiogram in normal humans and in patients with heart disease," *Annals of Noninvasive Electrocardiology*, vol. 8, no. 4, pp. 343–351, 2003. DOI: 10.1046/j.1542-474x.2003.08413.x.

[102] M. Clements and L. Roquemore, *Stem cell-derived models in toxicology*, ser. Methods in Pharmacology and Toxicology. New York, NY: Springer New York, 2017, p. 205. DOI: 10.1007/978-1-4939-6661-5.

[103] H. S. Hwang, D. O. Kryshtal, T. K. Feaster, V. Sánchez-Freire, J. Zhang, T. J. Kamp, C. C. Hong, J. C. Wu, and B. C. Knollmann, "Comparable calcium handling of human iPSC-derived cardiomyocytes generated by multiple laboratories," *Journal of Molecular and Cellular Cardiology*, vol. 85, pp. 79–88, 2015. DOI: 10.1016/j.yjmcc.2015.05.003.

[104] S. A. Niederer, E. Kerfoot, A. P. Benson, M. O. Bernabeu, O. Bernus, C. Bradley, E. M. Cherry, R. Clayton, F. H. Fenton, A. Garny, E. Heidenreich, S. Land, M. Maleckar, P. Pathmanathan, G. Plank, J. F. Rodríguez, I. Roy, F. B. Sachse, G. Seemann, O. Skavhaug, and N. P. Smith, "Verification of cardiac tissue electrophysiology simulators using an N-version benchmark," *Philosophical Transactions of the Royal Society A: Mathematical, Physical and Engineering Sciences*, vol. 369, no. 1954, pp. 4331–4351, 2011. DOI: 10.1098/rsta.2011.0139.

[105] K. Matsuno, F. Sahli Costabal, E. Kuhl, P. Perdikaris, and J. Yao, "Machine learning in drug development: characterizing the effect of 30 drugs on the QT interval using Gaussian process regression, sensitivity analysis, and uncertainty quantification," *Computer Methods in Applied Mechanics and Engineering*, vol. 348, pp. 313–333, 2019. DOI: 10.1016/j.cma.2019.01.033.

[106] J.-S. Park, J.-Y. Jeon, J.-H. Yang, and M.-G. Kim, " Introduction to in silico model for proarrhythmic risk assessment under the CiPA initiative," *Translational and Clinical Pharmacology*, vol. 27, no. 1, p. 12, 2019. DOI: 10.12793/tcp.2019.27.1.12.

[107] X. Yang and T. Papoian, "Moving beyond the comprehensive in vitro proarrhythmia assay: use of human-induced pluripotent stem cell-derived cardiomyocytes to assess contractile effects associated with drug-induced structural cardiotoxicity," *Journal of Applied Toxicology*, vol. 38, no. 9, pp. 1166–1176, 2018. DOI: 10.1002/jat.3611.

[108] G. Gintant, P. T. Sager, and N. Stockbridge, "Evolution of strategies to improve preclinical cardiac safety testing," *Nature Reviews Drug Discovery*, vol. 15, no. 7, pp. 457–471, 2016. DOI: 10.1038/nrd.2015.34.

[109] H. Cheng and T. Force, "Why do kinase inhibitors cause cardiotoxicity and what can be done about it?" *Progress in Cardiovascular Diseases*, vol. 53, no. 2, pp. 114–120, 2010. DOI: 10.1016/j.pcad.2010.06.006.

[110] K. R. Doherty, R. L. Wappel, D. R. Talbert, P. B. Trusk, D. M. Moran, J. W. Kramer, A. M. Brown, S. A. Shell, and S. Bacus, "Multi-parameter in vitro toxicity testing of crizotinib, sunitinib, erlotinib, and nilotinib in human cardiomyocytes," *Toxicology and Applied Pharmacology*, vol. 272, no. 1, pp. 245–255, 2013. DOI: 10.1016/J.TAAP.2013.04.027.